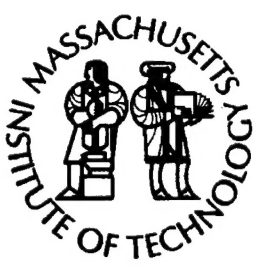


**Massachusetts Institute of Technology  
Woods Hole Oceanographic Institution**



**Joint Program  
in Oceanography/  
Applied Ocean Science  
and Engineering**

---

**DOCTORAL DISSERTATION**

*Observations and Modeling of Sand Transport in a Wave  
Dominated Environment*

by

Peter Traykovski

June 1998

**DISTRIBUTION STATEMENT A**  
Approved for Public Release  
Distribution Unlimited

19990526 078

**MIT/WHOI**

**98-25**

**Observations and Modeling of Sand Transport in a Wave Dominated Environment**

by

Peter Traykovski

Massachusetts Institute of Technology  
Cambridge, Massachusetts 02139

and

Woods Hole Oceanographic Institution  
Woods Hole, Massachusetts 02543

June 1998

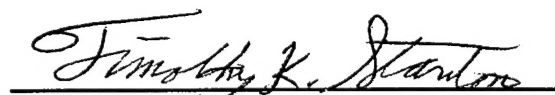
**DOCTORAL DISSERTATION**

Funding was provided by National Oceanic and Atmospheric Administration New York Bight Research Center Grant NA46GU0149 and Office of Naval Research Grant N00014-97-1-0556.

Reproduction in whole or in part is permitted for any purpose of the United States Government. This thesis should be cited as: Peter Traykovski, 1998. Observations and Modeling of Sand Transport in a Wave Dominated Environment. Ph.D. Thesis. MIT/WHOI, 98-25.

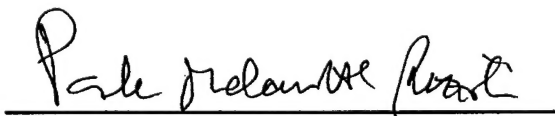
Approved for publication; distribution unlimited.

**Approved for Distribution:**



**Timothy K. Stanton**

Department of Applied Ocean Physics and Engineering



**Paola Malanotte-Rizzoli**  
MIT Director of Joint Program



**John W. Farrington**  
WHOI Dean of Graduate Studies

# **Observations and Modeling of Sand Transport in a Wave Dominated Environment**

by

**Peter Traykovski**

B.Se. Mechanical Engineering, Duke University, 1988

M.S. Applied Ocean Sciences and Eng., M.I.T./ Woods Hole Oceanographic Institution, 1994

O.E. Applied Ocean Sciences and Eng., M.I.T./ Woods Hole Oceanographic Institution, 1994

Submitted in Partial Fulfillment of the Requirements for the Degree of

**DOCTOR OF PHILOSOPHY**

at the

Massachusetts Institute of Technology  
and the  
Woods Hole Oceanographic Institution

May 1998

© 1998 Peter Traykovski  
All Rights Reserved

The author hereby grants to MIT and WHOI permission to reproduce and to distribute publicly  
paper and electronic copies of this thesis in whole or in part:

Signature of Author.....

Joint Program in Applied Ocean Sciences and Engineering  
Massachusetts Institute of Technology and  
Woods Hole Oceanographic Institution

Certified by.....

Dr. James D. Lynch  
Department of Applied Ocean Physics and Engineering  
Woods Hole Oceanographic Institution  
Thesis Advisor

Certified by.....

Dr. James F. Irish  
Department of Applied Ocean Physics and Engineering  
Woods Hole Oceanographic Institution  
Thesis Advisor

Accepted by.....

Professor Michael S. Triantafyllou  
Department of Ocean Engineering  
Chairman, Joint Committee in Applied Ocean Sciences and Engineering  
MIT/WHOI Joint Program in Oceanography and Oceanographic Engineering

# **Observations and Modeling of Sand Transport in a Wave Dominated Environment**

by

**Peter Traykovski**

Submitted to the Massachusetts Institute of Technology/  
Woods Hole Oceanographic Institution  
Joint Program in Oceanographic Engineering  
on May 12, 1998 in partial fulfillment of the  
Requirements for the Degree of Doctor of Philosophy in  
Oceanographic Engineering

## **Abstract**

Observations of bedforms, suspended sediment and water velocities were used to examine sediment transport processes at the sandy LEO-15 site located off the New Jersey coast. The bedforms were observed during storms using a rotary sidescan sonar and were found to be wave orbital scale ripples. The onshore migration of these ripples was forced by non-linear wave velocities, and could be related to a simple bedload model. Observations of suspended sand flux were calculated from acoustic backscattering profiles and water velocity profiles. Suspended sand transport forced by wave velocities was found to occur primarily during the weaker offshore phase of wave motion, as part of a vortex ejection mechanism. This net offshore suspended sediment flux was an order of magnitude less than the flux associated with onshore ripple migration. Thus it is hypothesized that ripple migration was forced by unobserved bedload or near bottom suspended flux. The net suspended sediment flux due to mean currents was a factor of five less than the wave-forced offshore suspended flux. These wave dominated events at LEO-15 represent a contradiction of the conceptual idea that waves are primarily responsible for suspending sediment and mean currents provide the transport mechanism.

## Contents

<b>Chapter 1: Introduction, Equipment Description and Calibration</b>	<b>14</b>
1.1 LEO-15 Site description	17
1.2 Instruments	18
1.2.1 Acoustic backscattering systems	21
1.2.2 LISST Instrument	22
1.2.3 Optical Backscattering Sensors (OBS)	22
1.2.4 Water velocity measurements	22
1.2.5 Bottom microtopography.	23
1.3 Data Sets	23
1.4 Instrument response, Calibration, and Preliminary Data processing	25
1.4.1 Acoustic and Optical Backscattering Instruments	25
1.4.2 Inverse Problem	35
1.4.3 LISST	37
1.4.4 Water velocity measurements	37
1.4.5 Sector Scanner Image Processing	38
1.5 Review of sediment transport modeling	40
1.5.1 1-d Models	40
1.5.2 Vortex ejection models	44
1.6 Outline of thesis	48
<b>Chapter 2: Geometry, migration, and evolution of wave orbital ripples at LEO-15</b>	<b>52</b>
2.1 Introduction	52
2.2 Instrumentation and current meter data processing	54
2.2.1 Sector scanning sonar	55
2.2.2 Acoustic Backscattering system	56
2.2.3 Current meters and current meter data processing	58
2.3 Ripple Geometry	62
2.3.1 Temporal evolution of ripple characteristics and type	62
2.3.2 Temporal evolution of ripple direction and wavelength	67
2.3.3 Empirical models for ripple wavelength	68
2.3.4 Temporal evolution in $\lambda/D$ , $d_0/D$ space.	70
2.3.5 Maximum ripple wavelength and transition to suborbital scaling	71
2.3.6 Ripple Height	74
2.4 Ripple Migration	77
2.4.1 Sediment transport due to ripple migration and suspended sediment transport	80
2.4.2 Bedload Modeling	84
2.5 Wave ripple climatology for LEO-15	88
2.6 Conclusions	90

<b>Chapter 3: Observations and Models of Sediment Transport at LEO-15: Wave or Current domination?</b>	<b>95</b>
3.1    Introduction	95
3.2    Site Description and Observational Techniques	98
3.2.1    Current meter data processing	99
3.2.2    ABS data processing and transport calculations	103
3.3    Description of Acoustic Backscattering Data	105
3.4    Wave time scale bottom boundary condition analysis	109
3.4.1    Determination of pickup function	109
3.4.2    Temporal dependence of the pickup function	113
3.5    Simple models for sediment transport by waves	116
3.5.1    Cumulative wave forced sediment transport	118
3.5.2    Grab, Lift and Trickle model	118
3.6    Sediment transport due to wave-current interaction	121
3.6.1    Transport Measurements	121
3.6.2    Modeling of concentration profiles and resulting transport	123
3.7    S4 long term current meter record analysis	128
3.8    Conclusions	131
<b>Chapter 4: Summary and Conclusions</b>	<b>135</b>
4.1    LEO-15 as a proto-typical site	135
4.2    Summary of thesis results	135
<b>Appendix A: A initial study on using full spectrum pulsed doppler to measure sand transport on and near the seafloor</b>	<b>138</b>

## List of Figures

- Figure 1-1 Conceptual diagram of the continental shelf. From a sediment transport perspective the inner shelf can be defined as the region where surface gravity wave non-linear steepening can produce substantial sediment transport due to waves alone. The middle shelf is defined as the region where significant wave velocities extend to the seafloor. In this region the waves are linear and thus may suspend sediment, but do not produce significant transport. On the outer shelf wave velocities do not reach the seafloor, and thus the transport and suspension is dominated by mean currents. Horizontal and vertical scales are grossly distorted. 14
- Figure 1-2 LEO-15 Bathymetry. The X marks the site location in 11 m deep water on the southern end of Beach Haven ridge. 17
- Figure 1-3 LEO-15 size distribution. The sieve mesh diameter is shown on the x-axis and the percentage by mass is shown on the y-axis. 18
- Figure 1-4 LEO 15 1995 tripod schematic diagram including instruments. Height to top is approximately 6 m. 19
- Figure 1-5 Acoustical and optical suspended sediment measuring instruments. Note the different beam width of the 1.0, 2.5 and 5.0 MHz acoustic systems. 21
- Figure 1-6 Sector Scanning Sonar 23
- Figure 1-7 Overview of the LEO-15-95 Deployment. The top plot shows burst-averaged data from the 2.5MHz ABS instrument. The dark gray line near 110cm range is the return from the bottom and shows elevation changes as ripples migrated past the acoustic beam. The lighter gray areas above the bottom are acoustic returns from suspended sediment. The correlation of suspended sediment to wave velocity is clearly visible. The wave velocity plot shows the maximum velocity from each 4 minute EMCW burst data. The current velocities are determined by averaging 4 minutes of EMCW burst data. The lines in the current plot represent alongshore (thick line) and cross-shore (thin line) currents. The cross-shore currents are marked by a pronounced semi-diurnal tidal variability. Corruption of the data quality due to biofouling is noticeable toward the end of the deployment, especially on the EMCW data. 24
- Figure 1-8 Scattering strength in terms of sediment size. The maximum scattering strength occurs near  $ka=1$  for each frequency used. For the OBS this corresponds to approximately 2 mm diameter, 5.0 MHz ~ 230 mm diameter, 2.5 MHz ~ 450 mm, 1.0 MHz ~ 1130 mm. For sediments smaller than  $ka=1$   $F(ka)$  falls off  $\mu a^3$ . For sediments larger than  $ka=1$   $F(ka)$  falls off  $\mu a^{-1}$ . 27
- Figure 1-9 ABS 2.5 MHz data as a function of range. a) Five profiles from the settling test data before applying range correction (thick line) b) Settling test after applying the range dependent correction factor 29
- Figure 1-10 2.5 MHz ABS Intensity is plotted vs. concentration (g/l) from bottle samples. The line represents the best fit to the data points. 31
- Figure 1-11 Example of 2.5 MHZ ABS data from the pour-in settling calibration experiment. 32

- Figure 1-12 2.5 MHz ABS measured sediment mass calculated using the two procedures described in the text vs. the actual mass of sediment poured into the tank during the settling experiments. The thick solid line is the line of one-to-one agreement. 33
- Figure 1-13 Size dependent scattering models and ABS data for 1.0 MHz and 2.5 MHz. 34
- Figure 1-14 a) Size dependent backscattering intensities calculated by equation 1.3 and b) Ratio of backscattered intensities for the 2.5 MHz and 1.0 MHz transducers. 36
- Figure 1-15 LISST transmission time series data and ABS intensity at 50cm above bottom. 37
- Figure 1-16 In the top left a Sector Scanner Image is shown with some of the largest ripples (1.0m wavelength, 15 cm height) in the deployment. The black line represents the trajectory of a water particle due to surface wave motions during a 4.25 minute EMCM burst. The typical scaling of orbital excursion distance = 1 to 2 times the ripple wave length is visible. The black dot is a arbitrary reference point used in viewing a movie of these images (<http://www.oal.whoi.edu/~petetray/leo15.html>) The plot in the upper right displays a direction/period spectrum of the surface wave field. Here the waves have periods of 18s and the direction lines up with the ripples. This plot also displays the r.m.s wave velocity and current velocity using the vertical scale (cm/s). The lower plot of the ABS data shows a time series of bottom elevation as ripples migrate past the ABS beam. The vertical line indicates when the sector scan image was taken from the time series 39
- Figure 1-17 In the 1-d models vertical profiles of velocity and sediment concentration are formed then multiplied and integrated to model transport. When the roughness elements have heights larger than the wave boundary thickness ( $\delta_{wave} \sim 1 - 10\text{cm}$ ) and horizontal scales on the order of the wave orbital distance, 2-d models that resolve the lee vortex ejection from each ripple may be more appropriate. 41
- Figure 1-18 Sediment trapping by vortices. The upper half of the figure shows how the combined vector motion of sediment fall velocity and water vortex motion leads to sediment trapping. The lower half shows a system of vortices and corridors of sediment trapping and/or upward advection over a rippled bed. 48
- Figure 2-1 LEO-15 bathymetry. The tripod location on the southern end of Beach Haven ridge is marked by an X. Depth contours are labelled in meters, and the grid spacing is 2.87 km. 54
- Figure 2-2 Rotary sidescan (sector scanning) sonar and acoustic backscattering system. 55
- Figure 2-3 Sector scanning sonar image (above) and 12 day time series of ABS vertical profiler data (below). The sector scanner image shows some of the largest ripples observed, with wavelengths of 1m, and the ABS shows changes in seafloor elevation as the ripples migrate past the acoustic beam. Light areas in both image represent high acoustic returns. In this image the SSS was located directly over a ripple crest, while the ABS is located over a trough. 56

- Figure 2-4 Acoustical and optical scattering intensities per unit sediment volume as a function of sediment diameter ( $D$ ) on the bottom axis and  $ka$  on the top axis. Intensities are normalized to have a maximum of unity. The acoustic results are generated using the expressions given by Sheng and Hay [1988]. The range of sediment diameters for which acoustic scattering intensity is within 50% of its maximum value is lightly shaded. This is approximately equal to the median grain size  $\pm 1$  std. The darker shaded region indicates the range of median grain diameters typically found at LEO-15. 58
- Figure 2-5 Current meter time series: a) Wave velocities, b) Wave period c) Wave orbital diameters, and d) Mean currents calculated from the BASS sensor 44 cm above the seafloor. e) Wave and current (constant drag coefficient) skin friction Shields parameter based on  $Hrms$  (left y-axis) and based on  $H1/3$  (right y-axis). The critical Shields parameter for initiation of motion of is also shown as a dotted and dash-dotted line for each case. 61
- Figure 2-6 Along crest variation length scale schematic. The dashed solid lines are the steady-state ripple patterns generated by waves before a directional shift through an angle  $q$ . The thin solid lines are the steady state ripple pattern after the directional change. The thick lines are the transitional state (as seen in image 5) with along crest oscillations of wavelength  $p$ . 63
- Figure 2-7 Representative sector scanning sonar images. The thick white line near the center of each image represents the wave orbital diameter scaled by  $3/4$ , and is aligned in the wave direction. The small plot below the upper left of each image displays the relative wave r.m.s. velocity (thick line) and current velocity (thin line). 66
- Figure 2-8 Temporal Evolution of Ripple features. a) Ripple wavelength ( $l$ ) and scaled significant wave orbital diameter ( $0.75do, 1/3$ ). Wave ripple type (2-d wave, 3-d wave), and periods of hysteresis (Hyst.) or relic ripples are indicated by the shaded regions b) Ripple direction and dominant wave direction. 68
- Figure 2-9 a) Ripple wavelength ( $l$ ) as a function of wave orbital diameter ( $do, 1/3$ ), with both quantities scaled by measured median grain size  $D50=400mm$ . Points represented by open circles are during times of hysteresis as determined from the time series b) Same as a, but hysteresis points not displayed and linear axis scaling. Points represented by crosses are 3-d wave ripples with a scaling of  $l=0.38do, 1/3$  shown as a dotted line. Points plotted as dots are 2-d wave ripples with a best fit line of  $l=0.76do, 1/3$  shown as dashed line. The thick solid line is the Wiberg and Harris [1994] empirical model with the orbital scaling of  $l=.62do$  and an orbital scaling of  $l=535D$  continued beyond the transitional (gray shaded) region as thin lines. 70
- Figure 2-10 Temporal evolution of ripple wavelength as a function of wave orbital diameter with both quantities normalized by median grain size ( $D50=400mm$ ). The dots, crosses, and open circles represent actual data points connected by lines in the order of occurrence. The different symbols indicate ripple type as in figure 2-9. The time of selected points is shown. The thick arrows are a conceptual model for the temporal evolution. The diagonal upward thick black lines are the trajectories along the orbital ripple scaling relations of

$l=0.38do, 1/3$  and  $l=0.76do, 1/3$ . The horizontal line with an arrow pointed to the left is the hysteresis path. 71

Figure 2-11

a) Ripple wave length as a function of significant wave orbital diameter with both quantities normalized by measured median grain size,  $D50=400\text{mm}$ . The Nielsen [1981] model is shown as the solid lines with wave periods varying from 10-16 seconds. The Grant and Madsen [1982] model, also with periods from 10-16 seconds, is shown as the dashed lines. b) The Wiberg and Harris [1994] model normalized by  $D85=800\text{ mm}$  is shown as the thick solid line. The best fits to the 3-d and 2-d wave ripple data are shown as the dotted and dashed line respectively. 74

Figure 2-12

An estimate of ripple height can be calculated from each sector scan image by examining changes in the distance AB from the transducer head (A) to the point of intersection of the lower edge of the beam pattern with the ripple surface (B). The distance AB changes as the transducer rotates to aim the beam at different locations on the ripple surface. 75

Figure 2-13

Evolution of ripple heights. a) Ripple heights (dots are the ABS altimeter estimates, dash-dot line is the SSS sidelobe estimate, and thick line is the average of the two estimates) and ripple wavelength scaled by 0.15 (thin solid line) as a function of time. b) Ripple steepness ( $h/l$ ) as a function of time. The open circle points are not reliable as described in the text, and are not included in the calculation of the mean (thin line, at  $h/l=0.15$ ). 76

Figure 2-14

Ripple migration as related to wave and current parameters. a) Ripple crest displacement,  $Xm$  (thick line),  $U3w$  (thin dashed line) and  $U3w,excess$  (thin solid line) b) Ripple crest velocity  $vm$  (thick line, left y-axis), and (thin line, right y-axis.) c) rms wave velocity ( $Uw,rms$ ) d) Alongshore ( $vc$ , thin line) and Cross-shore ( $uc$ , thick line) current velocities from BASS burst averages 44 cm above the seafloor. The cross shore current is dominated by the semi-diurnal tide, is relatively weak, and thus transports little sediment compared to waves. 78

Figure 2-15

Suspended sand transport and Ripple sand transport. a) Temporal evolution of cumulative net depth integrated suspended transport ( $M_{suspended,w}$ ). The scale for  $M_{suspended,w}$ , is on the right y-axis. Sand transport associated with ripples based on the assumption that ripples transport their entire volume of sand ( $M_{ripple}$ ). The scale for  $M_{ripple}$  is on the left y-axis. Bedload model forced with wave stresses as ( $M_{bedload,w}$ , left y-axis) calculated by the instantaneous wave velocities ( $uw(t)$ ) and forced with combined wave-current stresses ( $M_{bedload,wc}$ , left y-axis) b) Depth dependent transport  $mc, wave$  for periods yearday 235 to 245 (dashed line), 245 to 255 (dotted line), 255 to 260 (dash-dotted line), and 238 to 260 (thick line). Negative transports are onshore. 82

Figure 2-16

A simple conceptual model for relating bedload transport to ripple migration. The migration of the ripple profile over half a wave cycle is related to the temporally integrated flux convergence over the half wave cycle. The diagram is shown for the onshore half cycle of wave motion. 83

Figure 2-17

Vortex ejection and bedload forcing of ripple migration mechanism.

The greatest velocities are in the onshore direction. This onshore portion of the wave cycle moves fine and coarse sand over the crest (1) where most of the coarse sand is deposited to force the ripple migration as seen by the dashed line. This is the dominant cross shore transport mechanism. However some of this sand (particularly the finer fractions) that passes over the crest is entrained into a vortex in the lee of the ripple (2). This vortex is ejected upward into the water column during the wave reversal and is transported offshore in the next half of the wave cycle as it decays and sand settles out (3). The grain size dependence of this process is described in Bagnold [1946], and could account for the offshore suspended transport during periods of high wave velocity. While this process reverse every half wave cycle the stronger onshore velocities associated with non-linear waves allows the onshore phase to dominate. 87

Figure 2-18 Annual significant wave height vs. dominant period frequency of occurrence distribution from 8 years of NDBC [1995] buoy 40009 hourly observations located at the mouth of the Delaware Bay in 28m of water. The total area under the contours integrates to 100%, and contours are labelled in percent. The hatched area is the transitional region from wave orbital scale ripples to anorbital scale ripples defined with D=800mm. The dash-dotted and dotted lines are the Shields critical limits for initiation of motion for grain sizes of 400 and 800mm respectively. 89

Figure 3-1 LEO-15 bathymetry. The tripod location on the southern end of Beach Haven ridge is marked by an X. Depth contours are labelled in meters, and the grid spacing is 2.87 km. 98

Figure 3-2 Current meter time series: a) Wave velocities, b) Wave period c) Third moment, and d) Mean currents calculated from the BASS sensor 44 cm above the seafloor. e) Wave and current skin friction Shield's parameter based on H1/3 (right y-axis). The critical Shield's parameter for initiation of motion of is also shown as a dashed line. 100

Figure 3-3 a) Spectra of the wave velocity ( $uw$ ) for each data burst. The spectral level is represented by the grey scale. b) Time average of the spectra from yearday 248 and 254. 101

Figure 3-4 Schematic of the ABS sampling volume and ripple morphology 103

Figure 3-5 Several ABS profiles from a data burst on yearday 248.69. Profiles are separated by 10 seconds. a) The location of the seafloor ( $zt,max$ ) as defined by the maximum return is located at  $zt=96$ cm. The data for concentrations over  $10^{-4}$  mg/cm<sup>3</sup> is corrupted below 90cm by the return from adjacent ripple crests. b) The 6 cm above ( $zt,max$ ) have been extrapolated as described in the text. 104

Figure 3-6 a) Acoustic Backscattering System concentration depth profile time series from yearday 251.33. The strong return at 100 cm is from the seafloor. b) Wave velocity ( $uw$ , left y-axis) and depth integrated sediment concentration ( $Cz$ , right y-axis) time series. c) Depth integrated suspended sediment transport rate due to waves ( $Qz=uwCz$ ). The pulses of offshore transport at 105 and 120 seconds due to a group of non-linear waves are examples of the vortex ejection

- transport mechanism. 105
- Figure 3-7 Same plots as figure 3-6 with data from yearday 252.23. Examples of the vortex ejection mechanism are visible at 100 and 150 seconds. 106
- Figure 3-8 Same plots as figure 3-6 with data from yearday 248.69. In this case the group of waves at 20 to 60 seconds has approximately equal onshore and offshore velocities, thus producing little net transport. 107
- Figure 3-9 Same plots as figure 3-6, with data from yearday 252.9. This burst is not well described the vortex ejection mechanism, since the highest sediment concentrations occur 20 seconds after the large waves have past. 108
- Figure 3-10 Plot of VABS vs. the half wave cycle averaged Shields parameter . Dots with error bars represent the mean and standard deviation of the amount sediment suspended by each wave (VABS) as calculated by bin-averaging over 65,000 waves. The thicker line is a cubic relation and the thin line is a linear relation to the excess Shields parameter as given in equation 3.10. 111
- Figure 3-11 The amount of sand suspended in each half wave cycle measured by the ABS (VABS) vs. the amount predicted by equations 3.14 and 3.15 using the EMCM velocity record (V). The 45° solid line indicates the best fit of V to VABS using a scaling constant of Cp 112
- Figure 3-12 a) Temporal lagged correlation values (gray scale) as a function of time lag (Td in wave cycles) for each data burst (yearday) in the deployment. b) The average of and across all data bursts as a function of time lag (Td). 114
- Figure 3-13 Histogram of the temporal lag for maximum correlation of . 115
- Figure 3-14 Temporal lagged correlation of wave group velocity ( $u_g$ ) and depth integrated sediment concentration ( $C_z$ ) averaged over the data bursts in the period yearday 235 to 260. 115
- Figure 3-15 Predicted transport rates averaged over each half wave cycle (dots) are compared to measured sediment transport rates averaged over each half wave cycle (open circles) for the first three data bursts (a, b, and c respectively) shown in section 3.3. The instantaneous wave velocity  $u_w(t)$  is also shown (solid line) with scaling indicated by the right y-axis. 117
- Figure 3-16 a) Burst averaged wave sediment transport rate vs. time for both grab and dump model predictions and measured data. b) Cumulative wave-forced sediment transport flux vs. time for both model predictions and measured data. 119
- Figure 3-17 Vertical length scale of the suspended sediment profile  $L_z$  vs. the wave orbital diameter ( $2A_i$ ). The data has been bin-averaged and the best linear fit of is shown (solid line). 120
- Figure 3-18 a) Burst-averaged wave forced sediment transport rate vs. time for both GLT model predictions (solid line) and measured data (dotted line). b) Cumulative wave sediment transport flux vs. time for both model predictions and measured data. 121
- Figure 3-19 Alongshore current profile from the BASS current meter array for a data burst on 123
- Figure 3-20 Cumulative observed net transport flux due to waves alone ( $M_w$ ) and due to mean currents ( $M_c$ ). 124

- Figure 3-21 a) The gray scale shading represents burst-averaged sediment concentration as a function of time and depth. The time averaged length scale is also shown as the dots approximately 10 cm above the seafloor. b) Same data as panel a, but in the reference frame of the transducer ( $z_t$ ) so that . c) Wave skin friction velocity as a function of time. d) The ripple height ( $h$ , dash dotted line) and the scaled wave orbital amplitude (0.225A, solid line) as a function of time. 125
- Figure 3-22 Cumulative sediment transport by currents for the data (solid lines), the diffusive model (dotted lines), and the advective model (dashed lines). Thicker lines indicate along-shelf transport and thinner lines represent across-shelf transport. 128
- Figure 3-23 Selected hydrodynamic parameters from the S4 current meter record. The period during which data from the bottom tripod was analyzed is highlighted in grey. a) rms wave velocities. b) Wave period as calculated by equation 3.4. c) Mean alongshore currents. d) The wave Shields parameter calculated by equation 3.7. 129
- Figure 3-24 Cumulative sediment transport predicted using the S4 current meter data for three transport mechanisms. Wave forced bedload predicted by a wave-forced bedload model (thick solid line) [Traykovski et al., submitted], Wave-forced suspended sediment transport as predicted by the grab and dump model (thin solid line), and suspended sediment transport by mean current as predicted by the advective model (dashed and dotted lines). The period during which data from the bottom tripod was analyzed is highlighted in grey. 130
- Figure A-1 Sketch of bedload, saltation, and suspended load layers and doppler system geometry. 139
- Figure A-2 Alternate Doppler geometry for measuring vertical profiles in the boundary layer, and near bed transport. 140
- Figure A-3 Doppler shift with no strong stationary target 140
- Figure A-4 Doppler shift with a strong stationary target 141
- Figure A-5 Typical transmitted signal 143
- Figure A-6 a) Raw time series. b) After complex demodulation and low-pass filtering. c) 64 samples after block averaging 144
- Figure A-7 Inclined plane tank setup 146
- Figure A-8 Spectra from included plane tank test. Left side: with no moving sand only the stationary bed return at the carrier frequency is visible; Right side: with moving sand a “shoulder” of down-shifted (away from the transducer) returns appears. 147
- Figure A-9 Left: Doppler Spectra of intensity for the six flow speeds: 22, 35, 45, 50, 55, and 62cm/ in order of increasing flow speed. The spectra are averaged over all pings and normalized to have a maximum of unity. Right: Doppler spectra of flux (velocity \* intensity) with all six flow speeds are normalized by a single constant. 148
- Figure A-10 Upper panel: Acoustic and bedload trap measurement of bedload vs. flume nominal flow speed. Lower panel Acoustically measured bedload vs. bedload trap 149

# CHAPTER 1

## Introduction, Equipment Description and Calibration

The dynamics of sediment transport on the inner continental shelf have become an increasingly important research topic in the last two decades. It has become evident that a full understanding of the evolution of continental shelf topography and composition is not possible without a consideration of the role of sediment transport in the deposition and movement of shelf material. The inner shelf serves as a transition between the surf zone, the middle and outer shelf regions (figure 1-1). Past erosive and depositional events are recorded in the sediment stratified layers. Understanding the suspension and depositional processes which govern the formation of these strata can provide insight into the historical climatology that have led to the present day morphology of the inner continental shelf. Beyond understanding the evolution of the shelf, the ability to accurately model sediment transport dynamics has practical engineering applications, particularly in terms of understanding the fate of coastally discharged pollutant materials, as well as solving problems of coastal waterway dredging, coastal beach erosion, and the secure burial of submarine cables and pipelines. From a physical oceanographic perspective, sediment transport plays an important role in the frictional component of the momentum balance that governs coastal flows. Finally, an increased understanding of the complex interactions between sediment transport processes and biological oceanographic processes is necessary. The dynamics of sediment erosion and deposition help shape the habitat of a diversity of marine benthic organisms. These organisms, through their biological activities, alter the boundary layer flow dynamics, the bottom roughness, and the grain size composition and distribution.

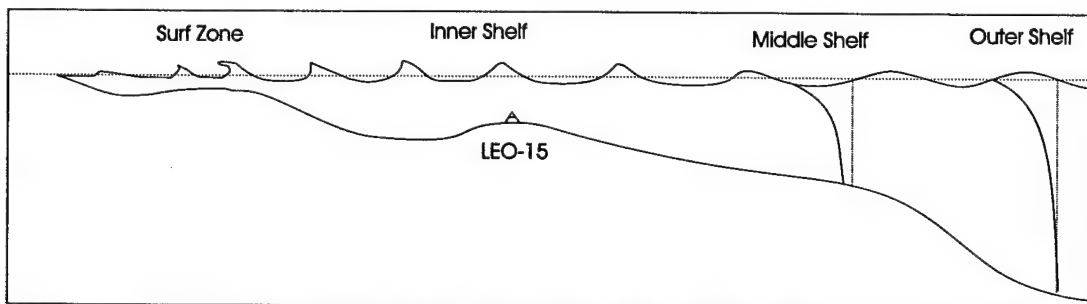
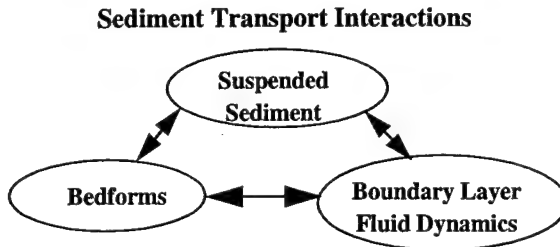


Figure 1-1 Conceptual diagram of the continental shelf. Form a sediment transport perspective the inner shelf can be defined as the region where surface gravity wave non-linear steepening can produce substantial sediment transport due to waves alone. The middle shelf is defined as the region where significant wave velocities extend to the seafloor. In this region the waves are linear and thus may suspend sediment, but do not produce significant transport. On the outer shelf wave velocities do not reach the seafloor, and thus the transport and suspension is dominated by mean currents. Horizontal and vertical scales are grossly distorted.

In order to understand sediment transport it is important to understand the interactions between the bottom roughness (bedforms), the hydrodynamic boundary layer and its frictional stress on the bottom, and the suspended sediment distribution. These three elements are mutually dependent:



The erosion and deposition of sediment creates the bedforms. The geometry of the bedforms, through its interactions with the hydrodynamics of the flow around the bedforms, serves to enhance or decrease the stress on the seafloor. This, in turn, controls the sediment suspension process. However, our ability to understand and model each of these elements and the interactions between them remains incomplete. For instance, although there are empirical models to predict bedform geometry based on flow conditions and sediment type (Wiberg 1994, Nielsen 1981), the prediction of migration rates has not been studied extensively. Regarding the fluid dynamics part of the framework, the boundary layer due to the steady current is fairly well understood, but the velocity structure and accompanying bottom stress due to wave motions over large steep bedforms is poorly understood, and has not generally been observed with sufficient spatial and temporal resolution.

The typical concept used for modeling sediment suspension is that of an equilibrium balance between upward turbulent diffusion of sediment and gravitational settling. This is often a good approximation for calculation of spatially and temporally averaged transport due to mean currents. However, preliminary examination of recently collected data at the inner continental shelf LEO-15 (Long-term Ecosystem Observatory in ~15m water) site shows that sediment suspension events are characterized by a series of temporally and spatially discrete ejections of sediment into the water, which are then available for transport by both waves and current. In particular, these ejections can lead to correlations between wave velocities and sediment concentration thus causing significant transport due to waves alone.

Field data to test existing ideas and models has been especially limited in quantity, as well as having low temporal and spatial resolution, although this has been improving in recent years. Few inner shelf studies have contained coherent observations of all three elements of the framework

described above. Classic suspended sediment sampling techniques (e.g. pump sampling) are accurate since the desired quantities are measured directly. Drawbacks of these techniques include low spatial and temporal resolution yielding only very averaged, or possibly aliased data which are unable to resolve the higher frequency physical processes. More recently, fast response sensors such as the Optical Backscattering Sensors (OBS) have been used to overcome some of these sampling problems. A universal problem with single frequency backscattering sensors is the confounding of sediment size effects and concentration effects. OBS sensors, which many recent studies have been based on, are most sensitive to the smallest sized sediments, and thus are unsuitable for measuring larger particle (e.g. sand) concentrations in the presence of any fine sediment. The most recent types of instrumentation being used to measure suspended sediment are multiple frequency acoustic and optic backscattering systems. These systems have high temporal and spatial resolution, and are also capable of collecting extended continuous time series.

The data set collected at the LEO-15 site includes temporally coherent and spatially co-located observations of bedform topography, bottom boundary layer fluid dynamics, and multiple frequency acoustic and optical suspended sediment measurements. A significant portion of this thesis is dedicated to describing the processing and analysis of this data, first to extract meaningful estimates of the relevant physical quantities, and then to understand the processes controlling the quantities. One of the main foci of this thesis is to better understand and quantify the sediment ejection process based on the observed bedforms. This includes investigating at the temporally and spatially dependent sediment bottom boundary conditions, the temporal and spatial distribution of suspended sediment, and the resulting transport. For the purposes of this thesis I will use the measurements of the fluid velocities and bedform structures as observed input quantities to try to understand and quantify the sediment transport process. This will be done by comparing components of existing transport/suspension models to measured data and developing new models where they are needed.

This chapter is presented in six sections as follows. The first two sections describe the LEO-15 site and the instruments used in a recent deployment. The third section describes the data taken during summer 1995 at LEO-15. The fourth section describes the preliminary processing of the instrumental data required before scientific analysis of the physical processes can proceed. Because it is necessary to carefully calibrate the acoustic backscattering data to derive sediment concentration, the fourth section contains a detailed description of the calibration methods. The fifth section contains a review of some of the basic types of models, concepts and observations

used to derive them. Models that attempt to describe some aspects of the time dependent sediment ejection process are discussed in some detail.

### 1.1 LEO-15 Site description

The LEO-15 site is located off the coast of southern New Jersey (figure 1-2). The data we will discuss was collected in 11 m depth water on the southern corner of the Beach Haven ridge. This 4km long by 1 km wide by 4 m high ridge is one of a series of ridges extending away from the coast at a characteristic 20 degree angle (Trowbridge 1995). These ridges are largely composed of sand over a bed of Holocene Lagoonal mud (Duane). Thus the finest sediment sizes are found in the troughs between the ridges, whereas coarser sediments are found on the ridges. Bottom samples taken on the southern crest of the ridge typically reveal medium sand with mean grain sizes of 1.1 to 1.6 $\phi$  (~450 to 330  $\mu\text{m}$ ) with standard deviations of 0.6 $\phi$  (2.2 $\phi$ ~220  $\mu\text{m}$ , 0.5 $\phi$ ~700  $\mu\text{m}$ ) (Craghan). There are also larger broken shell fragments which are not included the grain size analysis.

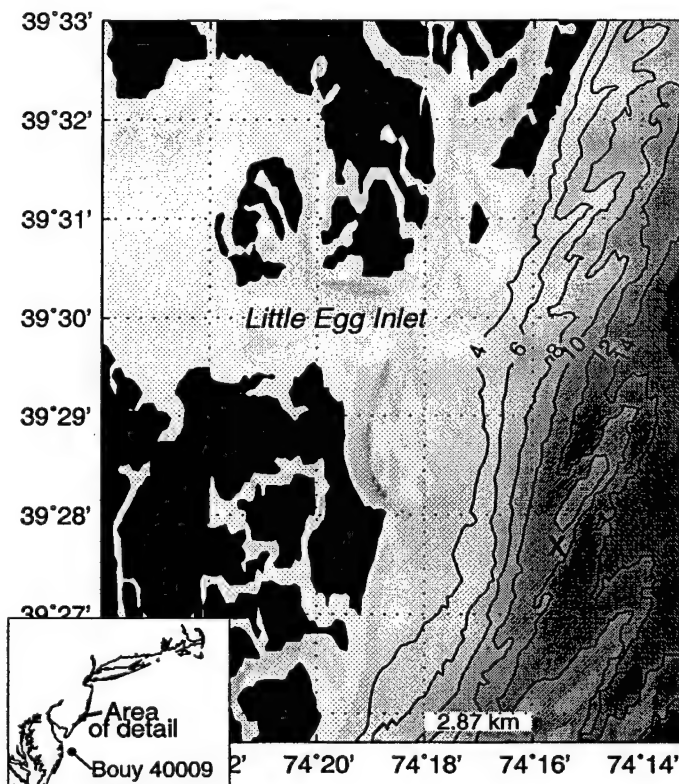


Figure 1-2 LEO-15 Bathymetry. The X marks the site location in 11 m deep water on the southern end of Beach Haven ridge.

A dry sieve analysis of sediment size from a sample taken from the LEO-15 site at the end of the observational period is shown in figure 1-3.

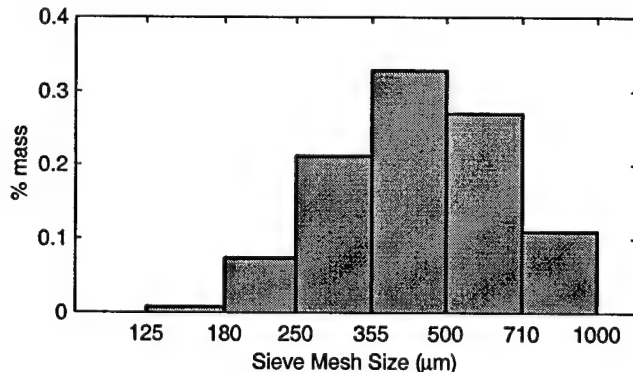


Figure 1-3 LEO-15 size distribution. The sieve mesh diameter is shown on the x-axis and the percentage by mass is shown on the y-axis.

The physical oceanographic environment at LEO-15 contains tidal currents with velocities of 10-15 cm/s with the semi-diurnal ellipse major axis aligned perpendicular to the shore, and the diurnal ellipse aligned parallel to the shore. Wind/pressure gradient forced currents measured 4 m above the seafloor often reach 25-35 cm/s during storms. Maximum wave velocities can reach 80 cm/s measured 4m from the bottom with associated r.m.s velocities of 35 cm/s during storms. Periods for storm generated waves are typically 6-12 seconds, but periods of up to 18 seconds are observed during the passage of offshore hurricanes. In LEO-15's sandy environment and shallow water depth longer period waves are not attenuated substantially. Linear wave theory predicts waves with periods of 6 seconds are attenuated by 60% in 11 m deep water, but waves of periods greater than 9 seconds are attenuated less than 30% due to the depth. The typical observed bedforms during storms are wave generated ripples with wavelengths roughly 3/4 of the wave orbital excursion distance. Thus these ripples have wavelengths of up to 1.0 m and heights of up to 15 cm.

## 1.2 Instruments

The overall goal of our measurement program at LEO-15 was to measure the size-dependent suspended sediment concentration and transport together with the relevant physical forcing parameters, including bottom roughness and water velocities. With this objective in mind several different instrument systems were deployed on bottom-moored tripods (figure 1-4) at the LEO-15 site.

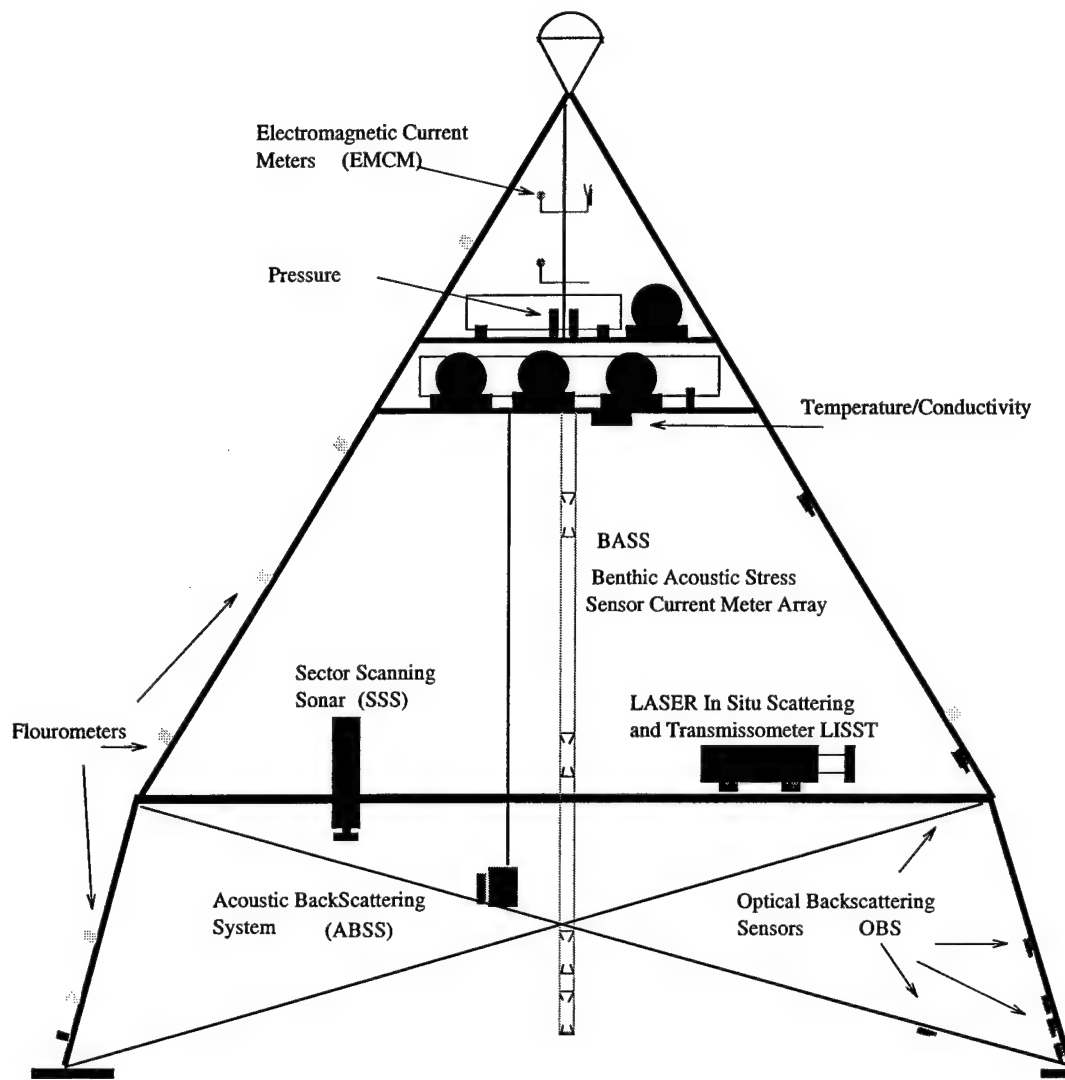


Figure 1-4 LEO 15 1995 tripod schematic diagram including instruments. Height to top is approximately 6 m.

To measure suspended sediment concentration, two acoustic backscattering systems and optical backscattering sensors were used. While a direct measurement of the size dependence of the suspended sediment concentration was attempted using the Laser *In-Situ* Sizing and Transmissometry (LISST) instrument developed by Y. Agrawal at Sequoia Scientific, this instrument is not well suited to the medium grain sized sand found at LEO-15 (Traykovski et al, submitted). Transport of sediment was also not measured directly, but was calculated using the acoustic backscattering data and water velocity data as measured by ElectroMagnetic Current Meters (EMCM's) and the Benthic Acoustic Stress Sensor (BASS). These water velocity

measurements are also needed as forcing parameters for the suspension modeling. Another important measurement in sediment transport is the bottom roughness. To measure roughness, both the acoustic backscattering systems, which serve as altimeters, and a rotary Sector Scanning side scan Sonar system (SSS) were used.

Since both wave and current action are important in resuspending and transporting sediment, the time sampling of most of the instruments was designed to sample both the faster wave period time scale and the slower current time scales. To do this, the instruments were typically run at a fast (15 - 4 Hz) sampling rate for several (4-8) minutes to capture the waves and wave groups. These bursts were repeated every hour or half hour to monitor the slower scale processes. This conserves battery power and computer memory enough to allow for deployment lengths of several months. For specific details on the sampling schedules of each instrument see table 1-1.

Instrument Package	Sensor	Height (cmab)	Burst Interval (min)	Burst Duration (sec)	Freq. in Burst (Hz)
EMCM	T24	540	30	240	4
	One channel dead	479			
ABS <sup>x</sup>	1 MHz	110	30	248	2
	2.5 MHz <sup>x</sup>	110			
ABSS <sup>x</sup>	1 MHz Upward	46	6	80	0.5
	5 MHz Downward	110			
	Pressure	418			
SSS	4m Range	122	30	4.5 s/rot	1 rot
OBS	1	14	30	240	4
	2*	37			
	3*	37			
	4*	37			

Table 1-1 Omni Tripod (WHOI Equipment Only)-Aug 24-Oct 9,1995

\* OBS 2,3,4 are in a horizontal triangular array.

<sup>x</sup>ABSS 5MHz and ABS1,2.5MHz, are co-located (figure 1-5).

The Rutgers Marine Sciences Group (P.I. Dr. Scott Glenn) also deployed a BASS array with OBS sensors and Temperature/Conductivity sensors. Sequoia Scientific (P.I. Dr. Yogesh Agrawal) deployed two LISST instruments, a Laser Doppler Velocimeter (LDV), and a Bottom aimed Camera on a separate tripod.

The following is a brief description of each of the systems, more details on the physics of the scattering processes and how these measurements are converted to physical quantities is included in the calibration section (1.4) of this thesis.

### 1.2.1 Acoustic backscattering systems

The acoustic systems measure vertical profiles of acoustic backscattering by transmitting a short pulse (10-12  $\mu$ s) of acoustic energy and then time sampling the backscattered energy. The time sampling rate is 75 kHz, which gives range resolution cells of 1 cm. The instruments are capable of recording 128 range bin samples, but are usually placed 110 cm above the bottom of the tripod to allow for any seabed elevation changes.

The Acoustic Backscattering System (ABS) has 1.0 and 2.5 MHz downward looking transducers (figure 1-5). The beamwidth as defined by the -3dB point is 20° for the 1.0 MHz system and is 15° for the 2.5 MHz system. This gives a bottom “footprint” of 80 cm and 60 cm respectively when the instruments are mounted 110 cm above the bottom.

A second acoustic system, called the Acoustic BackScattering System (ABSS), has a 5.0 MHz downward looking and a 1.0 MHz upward looking transducer. The 5.0 MHz transducer also has 1 cm range resolution, but a narrower beamwidth of 0.8° giving a footprint of 1.5 cm. The 1.0 MHz upward transducer has 128 20cm range cells and thus spans the entire water column at LEO-15.

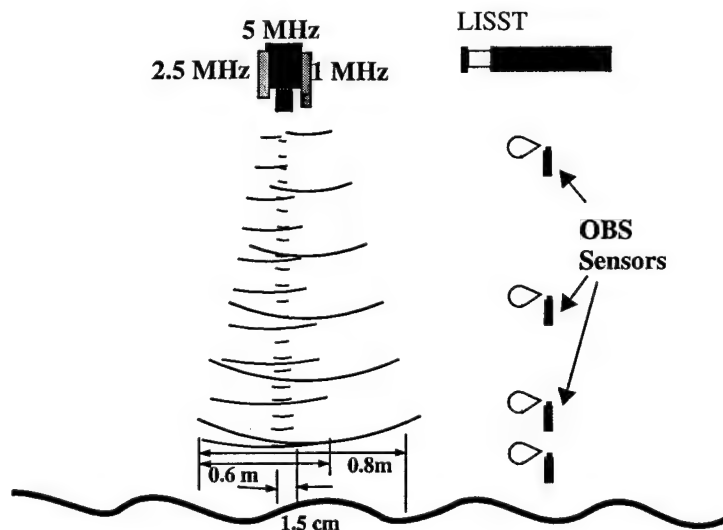


Figure 1-5 Acoustical and optical suspended sediment measuring instruments. Note the different beam width of the 1.0, 2.5 and 5.0 MHz acoustic systems.

### **1.2.2 LISST Instrument**

The LISST sensor transmits a 670nm laser beam across a 10 cm path to a receiver that measures the amount of energy transmitted as a function of small (0.05-4.5°) forward scattering angle. The total amount of energy transmitted is used to measure sediment concentration and the angular distribution of the transmitted energy is used to invert for particle size distribution (Agrawal, 1991). The LISST instrument does not sample within the wave period as it takes samples every 10 minutes. Each sample is a 16 “ping” average which takes 6 seconds to complete; this is not ideal since the wave periods of interest at LEO-15, which have periods ranging from 4 to 18 seconds. LISST’s possible aliasing of the wave period may not be a problem for the higher LISST sensor located at approximately 1 m above the seafloor, since sediment ejections on the wave time scale reach 1 m infrequently. Temporal variance at this height was expected to be dominated by slower scale processes. However, aliasing certainly could be a problem for the lower sensor located at approximately 30 cm above the seafloor.

### **1.2.3 Optical Backscattering Sensors (OBS)**

Optical backscattering sensors transmit infrared light at a wavelength of 850nm and measure backscattering from a volume of roughly 15 cm long by 10 cm<sup>2</sup> directly in front of the sensor. At higher concentrations, this sampling volume decreases due to attenuation. The OBS sensors integrate over the entire illuminated volume unlike the acoustic systems. Because this is essentially a point measurement, OBS sensors are usually placed in a vertical array, with the closest vertical spacing between sensors near the seafloor

### **1.2.4 Water velocity measurements**

To measure current and wave velocities, two different types of current meters were used on the tripod at the LEO-15 site. The EMCM measures two perpendicular horizontal components of current velocity by producing two perpendicular magnetic fields and measuring changes in the electric fields caused by the motion of the conducting sea water. These sensors are typically deployed in a vertical array at the same elevations as the OBS sensors.

In the late summer 1995 LEO-15 deployment a vertical array of BASS current meters were deployed by Dr. Scott Glenn from Rutgers University. These sensors measured two horizontal components of velocity by using differential acoustic pulse travel times over an approximately 10 cm long path.

### 1.2.5 Bottom microtopography.

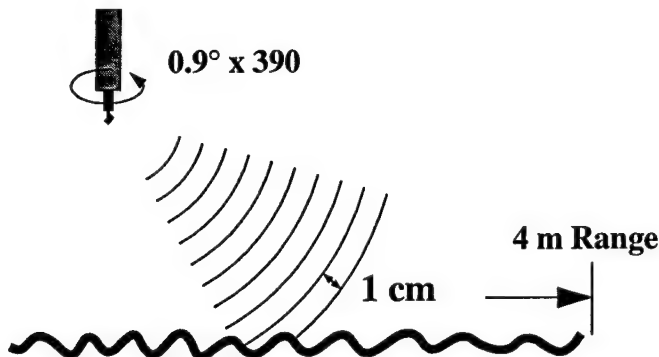


Figure 1-6 Sector Scanning Sonar

The (SSS) Sector Scanning Sonar is a rotary sidescan sonar operating at 2.25 MHz. It creates images of seafloor backscattering with a radial resolution of ~1 cm and angular resolution of 0.9° (~2.0 cm at  $r=1$  m, 5.1 cm at  $r=3.5$  m) by sweeping through 390 0.9° angular bins and range gating with 1cm bin size. The imaged area has a 4 m radius. This can be converted to an image of seafloor topography by using the fact that surfaces facing the sonar are strong reflectors and surfaces facing away from the sonar are weaker reflectors. The SSS makes an image of the bottom every half hour which seems to be adequate for our work at LEO-15, as preliminary analysis shows ripple migration speeds of one wavelength per 7 hours

### 1.3 Data Sets

Four deployments were conducted by the WHOI group (J.D. Irish, J.F. Lynch, P. Traykovski) at the LEO-15 site over the last three years. The first (LEO-15-1) was in the winter of 1993-94 from December 9th to January 11th. Unfortunately the acoustic system failed for the first winter deployment so the only sediment concentration measurements obtained were from the OBS. This data will not be utilized in the present thesis work. The second and third deployments (LEO-15-2,3) were made in the early summer of 1994 (May 11-May 29),(June 1-June 28). In each of these deployments two tripods were deployed. One tripod contained the ABS system with the 1.0 MHz and 2.5 MHz downward sonars and an array of OBS/EMCM sensors. The other tripod had the ABSS system with the 1.0 MHz upward and the 5.0 MHz downward sonar. This tripod also had a OBS array with a VACM current meter. The beginning of the May deployment was marked by a storm with northeast winds but was relatively calm thereafter. The June deployment had several periods of increased and decreased backscattering associated with upwelling and downwelling

favorable conditions. The largest sediment concentration in this deployment occurred at the end of the deployment with a southerly wind storm.

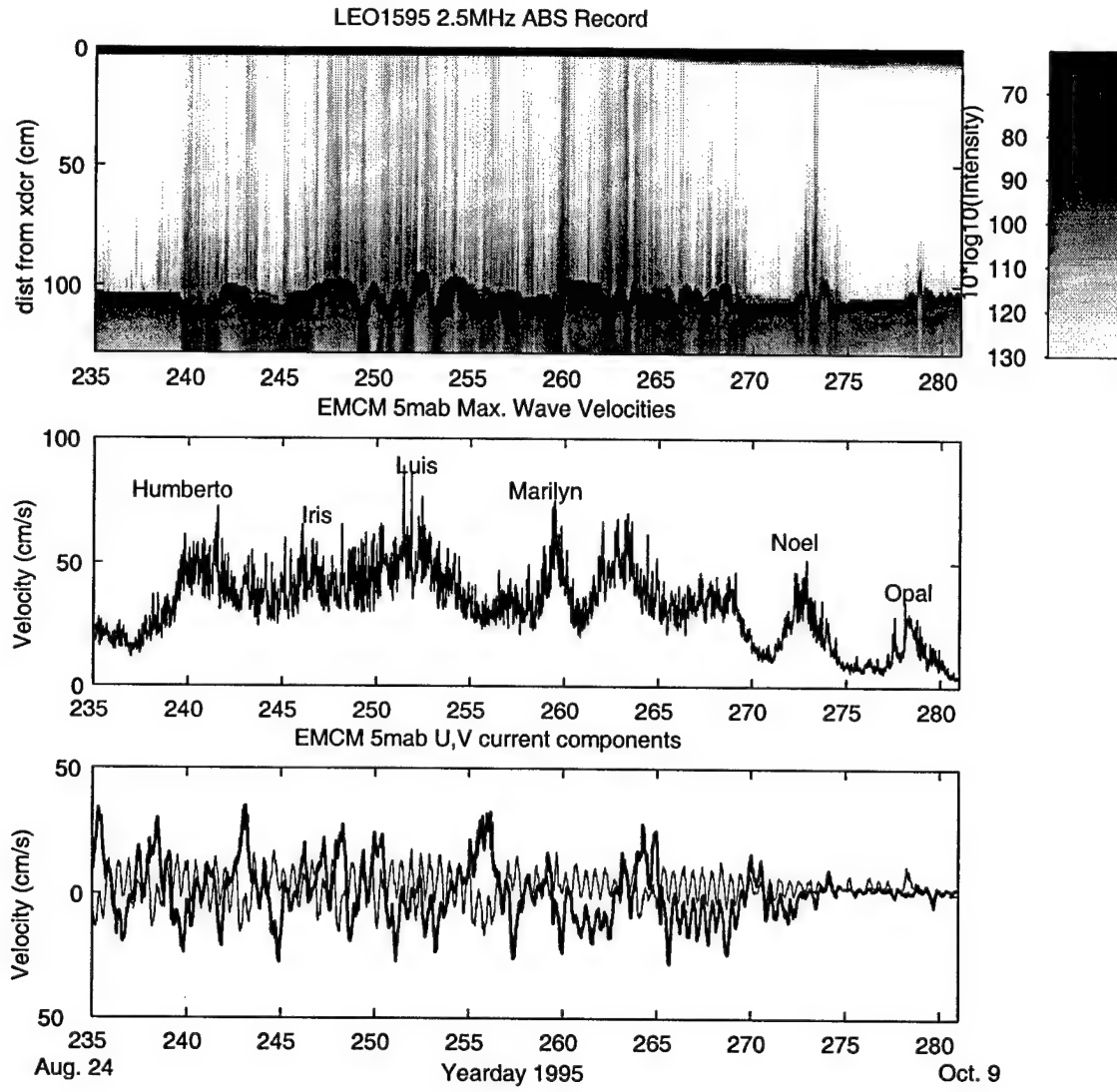


**Figure 1-7** Overview of the LEO-15-95 Deployment. The top plot shows burst-averaged data from the 2.5MHz ABS instrument. The dark gray line near 110cm range is the return from the bottom and shows elevation changes as ripples migrated past the acoustic beam. The lighter gray areas above the bottom are acoustic returns from suspended sediment. The correlation of suspended sediment to wave velocity is clearly visible. The wave velocity plot shows the maximum velocity from each 4 minute EMCM burst data. The current velocities are determined by averaging 4 minutes of EMCM burst data. The lines in the current plot represent alongshore (thick line) and cross-shore (thin line) currents. The cross-shore currents are marked by a pronounced semi-diurnal tidal variability. Corruption of the data quality due to biofouling is noticeable toward the end of the deployment, especially on the EMCM data.

The fourth deployment (LEO-15-95) took place in the late summer of 1995 from August 24th to September 9th. During this period seven tropical storms passed the east coast; several of which attained hurricane strength (figure 1-7). Two tripods were used. The larger tripod contained all the instrumentation described above except the LISST, which was deployed on a separate smaller tripod along with a LDV and a camera. This provides a unique data set with multiple instruments sampling the same (or nearly adjacent) volume at the same times. The thesis work will rely most heavily on this data set since it is the most complete.

## **1.4 Instrument response, Calibration, and Preliminary Data processing**

This section discusses how the output of the various instruments can be interpreted and converted to measures in standard units. Parts 1.4.1, 1.4.2 and 1.4.3 of this section deals with the instruments designed to measure sediment concentration and size distribution. In particular, part 1.4.2 describes the calibration procedures whereby acoustical backscattered intensities are converted to sediment concentration estimates. Part 1.4.4 discusses the current and wave velocity measurements from the EMCMs. Part 1.4.5 discusses the sector scanning sonar bottom roughness measurements.

### **1.4.1 Acoustic and Optical Backscattering Instruments**

Much theoretical and experimental work has been done on understanding how acoustic backscattering systems such as the ABS/ABSS work. (Hay 1983, Sheng and Hay 1988, Thorne 1993) The general problem can be cast in two forms. In the forward problem, one tries to predict the acoustic or optical intensity as a function of range and frequency given known sediment properties (size distribution, density, mass concentration). It is assumed that all the sediment has the density of quartz. In the inverse problem, which is the desired solution for the field data, one tries to estimate the sediment properties from the backscattered intensity of the different frequency systems (Hay 1992, Lynch 1994).

Generally the acoustical or optical intensity  $I$  from range  $r$  at a frequency defined by wavenumber  $k$  is given by:

$$I(k, r) = S \int_0^{a_{max}} F(ka)c(r)n(a, r)R^2(r)da \quad (\text{EQ 1.1})$$

where  $F(ka)$  is the scattering function as a function of wavenumber and sediment diameter ( $a$ ).  $c(r)$  is the total mass concentration as a function of sediment size and range.  $R(r)$  is the range dependence of the instrument response, and  $S$  is a constant of proportionality.  $n(a,r)$  is the size distribution of the sediment as a function of range. It is normalized so that  $\int_0^\infty n(a)da = 1$ .

Sheng and Hay (1988) found that the scattering function  $F(ka)$  for irregular sand grains can be described by a rigid moveable sphere model, and they provided a simple high-pass (in the wavenumber domain) approximation to the rigid moveable sphere model. The dominant physics of this model is determined by Rayleigh scattering when the particle is much smaller than an acoustic wavelength ( $ka \ll 1$ ). In this case inertia controls the scattering process and the pressure is proportional to the particle volume ( $p \propto a^3$  or  $I \propto p^2 \propto a^6$ ). When the particle is much larger than the wavelength ( $ka \gg 1$ ) geometric scattering occurs and the intensity is proportional to the surface area of the particle ( $I \propto a^2$ ). Since the scattering is proportional to the number of scatterers per unit volume of water, in order to use mass concentration in equation 1.1 the scattering dependence must be divided by a factor of  $a^3$  (sediment volume). Thus  $F(ka)$  is proportional to  $a^3$  for small particles and low frequencies ( $ka \ll 1$ ) and  $a^{-1}$  for large particles or high frequencies. The largest response occurs near  $ka = 1$ . This size-wavenumber dependence can be expressed as:

$$a^3 F(ka) = a^2 \left( \frac{K_f(ka)^2}{1 + K_f(ka)^2} \right)^2 \quad (\text{EQ 1.2})$$

A typical value for  $K_f = 1.1$  for water and quartz sediment. Thorne (1993) suggested additional structure to this function near  $ka = 1$ , to better fit measurements. Thus equation 1.3 becomes:

$$a^3 F(ka) = a^2 (1 - v_1 e^{-(ka-x_1)/\eta_1})^2 (1 - v_2 e^{-(ka-x_2)/\eta_2})^2 \left( \frac{K_f(ka)^2}{1 + K_f(ka)^2} \right)^2 \quad (\text{EQ 1.3})$$

where  $v_1 = 0.3$ ,  $\eta_1 = 0.5$ ,  $x_1 = 1.4$ ,  $v_2 = 0.25$ ,  $\eta_2 = 2.2$ , and  $x_2 = 2.8$ .

Figure 1-8 displays  $F(ka)/a$  normalized to a maximum of one for the three acoustic and one optical frequencies used in terms of sediment diameter ( $2a$ ). The figure clearly displays the fact that OBS instruments are sensitive to the finest sediments and are thus not suitable for measuring sand concentrations in the presence of small amounts of fine sediment. Likewise the three acoustic frequency instruments are most sensitive to different sand size fractions, and not the finer fractions. In figure 1-8 equation 1.3 was used for the three acoustic frequencies, while the more approximate asymptotic expression (equation 1.2) was for the optical frequency.

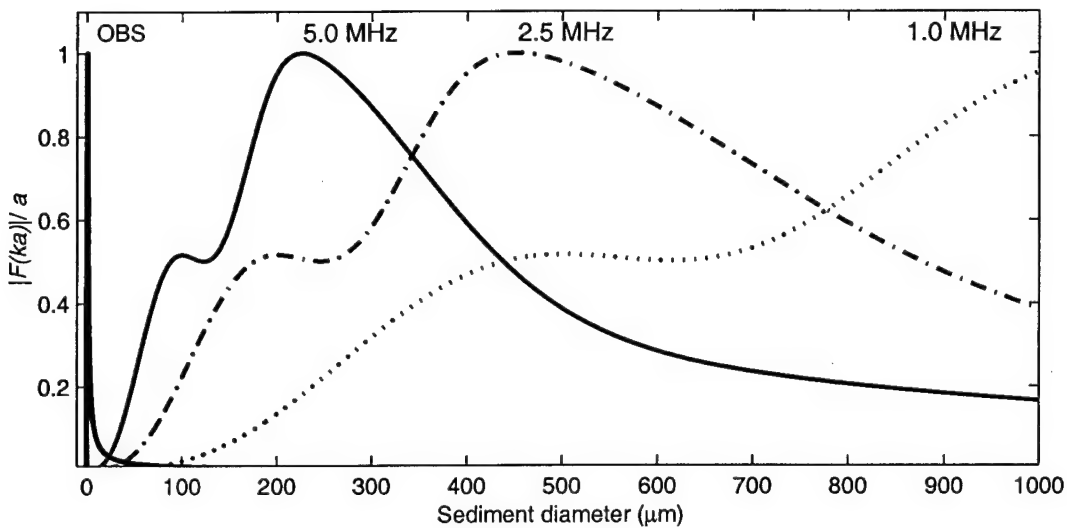


Figure 1-8 Scattering strength in terms of sediment size. The maximum scattering strength occurs near  $ka=1$  for each frequency used. For the OBS this corresponds to approximately 2  $\mu\text{m}$  diameter, 5.0 MHz  $\sim 230 \mu\text{m}$  diameter, 2.5 MHz  $\sim 450 \mu\text{m}$ , 1.0 MHz  $\sim 1130 \mu\text{m}$ . For sediments smaller than  $ka=1$   $F(ka)$  falls off  $\propto a^3$ . For sediments larger than  $ka=1$   $F(ka)$  falls off  $\propto a^{-1}$ .

To relate this theoretical description of scattering from suspended sediments to our experimental data from the calibration tests, as well as to calibrate the suspended sediment measuring instruments, two different sets of experiments were performed. The first set of calibration experiments was performed before the LEO-15 1995 deployment and consisted of a relatively simple settling experiment. The settling experiment was performed by adding sediment from a bottom sample taken at the LEO-15 site to the tank until the maximum expected field concentration is reached. Then the tank was stirred vigorously for several minutes to suspend all the sediment. Then stirring was halted to allow the sediment to settle while the acoustics system sampled. Bottle samples were taken over the next 24 hours on a roughly logarithmic time scale, with the most samples being taken in the first few minutes when the largest sediments are falling out of suspension. The bottle samples were analyzed using standard wet sieving and vacuum filtering techniques for total mass and size distribution. Once this experiment was completed the settling test was used to determine the instrument's response to a varying size distribution and concentration.

A second type of calibration experiment was also performed with finer sediment. In the concentration experiment sediment was added to the tank while stirring, and immediately after stirring was halted the acoustic system sampled. Additional quantities of sediment were then

added in several steps. While this test is designed to produce varying concentration levels with the same size distribution, it does not work well for the fast fall velocities (6 cm/s) of sediment found at LE0-15. It actually became a settling test since sediment begins to settle as soon as the stirring is ceased. However, with finer sediment that has slow settling velocities the concentration experiment can be used to determine the range dependence of the instrument's response ( $R(r)$ ) in equation 1.1).

To determine the unknown parameters in equation 1.1 the first step is to convert the acoustic instruments raw output into units proportional to intensity. The data  $d(r)$  coming out of the instrument,  $d=0-255$  for the ABS (8 bit),  $d=0-4095$  for the ABSS (12 bit) are amplified by a logarithmic amplifier. The OBS data is amplified using a linear amplifier. Thus acoustic intensity is related to the instrument output  $d$  by a logarithmic amplification factor  $A$ :

$$I = A^d \quad d = \frac{\log I}{\log A} . \quad (\text{EQ 1.4})$$

Since intensity is linearly proportional to concentration,  $A$  can be solved for if the size distribution remains constant, as it does in the concentration calibration experiment. The manufacturers of the instruments give values for  $A$  to convert the data into decibels. The values from the concentration calibration agree well with the specified values for the ABSS, but are off by a factor of 2 for the ABS system. This factor of two probably results from the ABS manufacturer referring to  $10\log_{10}(\text{volts})$  (with volts  $\sim$  pressure) as decibels while acousticians typically use  $10\log_{10}(\text{pressure}^2)$ .

Figure 1-9 displays the 2.5 MHz ABS raw data from the settling test as a function of range. The first 5 cm are corrupted by transducer ringing and the peak at 78 cm is the bottom of the tank. The multiple lines in this plot represent the different time steps in this type of calibration test.

Once the instrument's output has been converted to units proportional to intensity, the range dependence  $R(r)$  in equation 1.1 must be corrected for before the constant  $S$  relating intensity to concentration can be found. The range dependence of the instrument and the scattering process is generally defined by:

$$R^2(r) = \frac{e^{-4(\alpha_w + \alpha_s)r}}{r^2} \quad (\text{EQ 1.5})$$

where  $\alpha_w$  and  $\alpha_s$  are water and sediment attenuation coefficients, and  $r$  is range from the transducer. The sediment attenuation is a function of sediment concentration, range and sediment

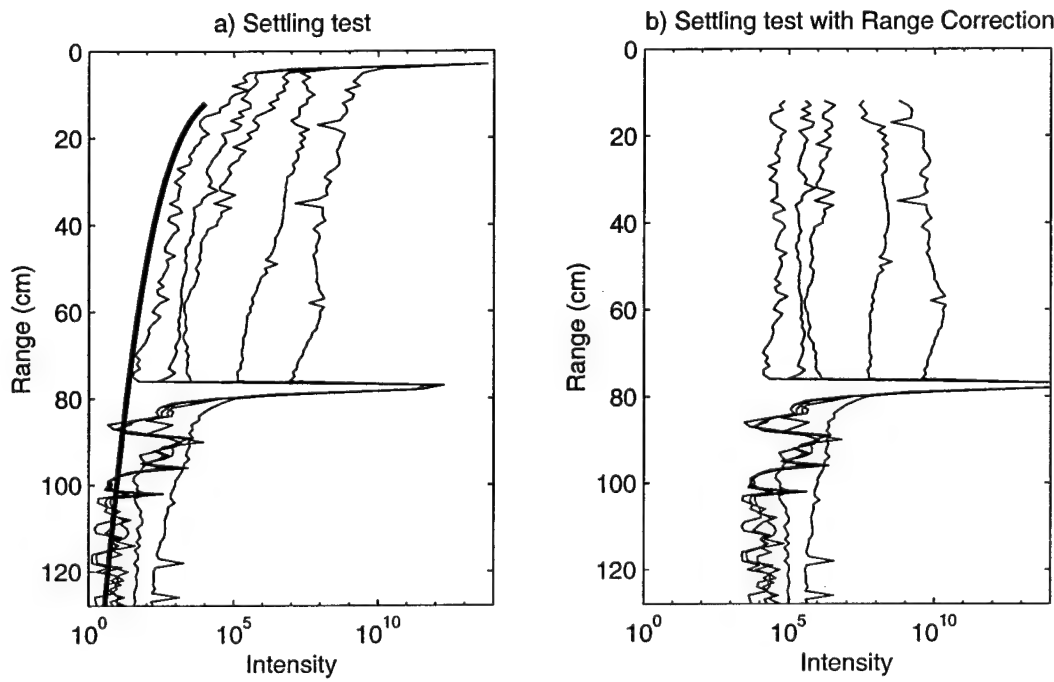


Figure 1-9 ABS 2.5 MHz data as a function of range. a) Five profiles from the settling test data before applying range correction (thick line) b) Settling test after applying the range dependent correction factor

size distribution. For the purposes of calibration we will assume concentration to be independent of range in the concentration tests. This should be a valid assumption since the tank is stirred thoroughly before the acoustic system samples.

The most obvious indicator of sediment attenuation becoming significant is when the bottom return begins to decrease due to acoustic "shadowing." To account for this, algorithms developed by Thorne (in press) can be used to equalize the bottom return by increasing the attenuation coefficient during periods of high suspension.

The factor of  $1/r^2$  in equation 1.4 is given by spherical spreading from the transducer and back ( $1/r^4$ ) times a factor of  $r^2$  for the increase of the insonified volume with range. Since these high frequency acoustic systems are often operated in the near field of the transducer ( $r < r_n = \pi a_t^2/\lambda$  where  $a_t$  is the transducer radius) a correction factor of  $[(2 + Er_n/r)/3]^2$  where  $E=2$  is suggested in the denominator of equation 1.5 for the near field by Thorne. For the 2.5 MHz transducer,  $r_n$  is at approximately 50 cm.

To examine the validity of equation 1.5, raw data ( $d$ ) is converted to intensity using  $A$  and then divided by  $R^2$ . The result of this process is range corrected intensity:

$$I_r = A^d / R^2(r) \quad (\text{EQ 1.6})$$

This operation is displayed in figure 1-9 for the 2.5 MHz system. A best fit of  $\alpha=0.015 \text{ cm}^{-1}$  ( $\alpha=\alpha_w+\alpha_s$ ) is used to remove the range dependence. The residual slope of the range dependence and the strength of bottom return is proportional to variability in concentration. In figure 1-9 there is no systematic relation between sediment concentration and range dependence, thus most of the attenuation must be from  $\alpha_w$ . The variability of the two profiles with high concentrations seen in figure 1-9 are most likely due to gradients in sediment concentration and size distribution as the sediment settles out. The variability is not due to varying attenuation because the bottom return in figure 1-9 is relatively constant.

In figure 1-10 the raw data from range cells  $r= 10$  to  $25 \text{ cm}$  is converted to intensity using equation 1.4 and  $A_{(2.5\text{MHz})}=10^{(16/255)}$  and averaged across these range cells. While there appears to be a linear trend to the data there are effectively only two data points since many points fall near zero intensity and concentration. To remedy this problem a more thorough set of calibration experiments was performed after the deployment. Errors in this type of calibration is most likely not caused by variability of the acoustic return since each line is an average of 120 profiles, but is due more to errors in bottle sampling and weighing. The weighing process is particularly suspect, since the paper filters often weigh more than the sediment for low concentrations. To get the sediment mass the dry filter is weighed and then the dry sediment and filter are weighed and the two are subtracted. At high concentrations, the bottles sample a non-uniform concentration field as clouds of sediment are stirred off the bottom with each stroke of the canoe paddle.

The data from figure 1-10 is used to determine the calibration constant ( $K$ ) using a least squares fit, so that the calibrated intensity ( $I_c$ ) will be the acoustic estimate of range dependent concentration ( $c(r)$ ) for this size distribution.

$$I_c = \frac{1}{K} I_r \quad (\text{EQ 1.7})$$

The calibration constant  $K$  is theoretically related to the parameters in equation 1.1 by:

$$K = S \int_0^{a_{max}} F(ka)n(a)da \quad (\text{EQ 1.8})$$

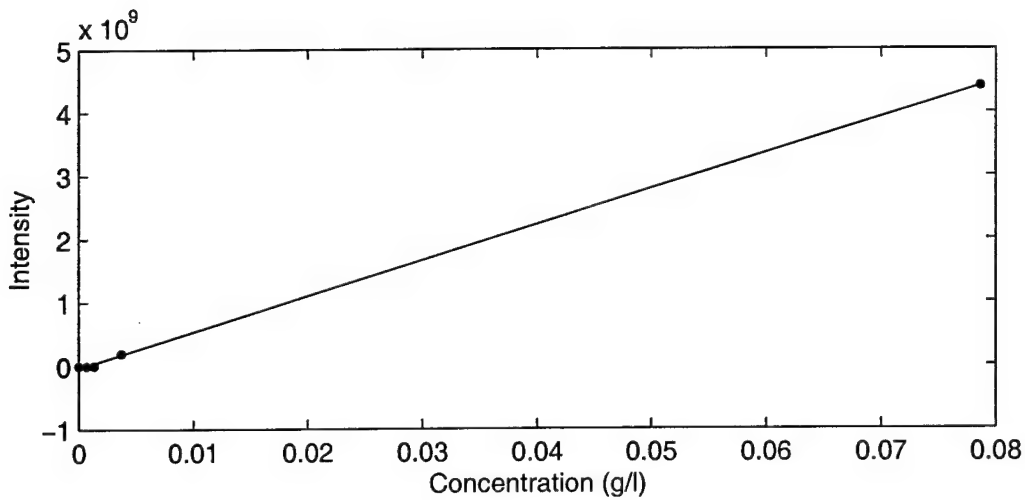


Figure 1-10 2.5 MHz ABS Intensity is plotted vs. concentration (g/l) from bottle samples. The line represents the best fit to the data points.

To generate a more complete calibration data set, a second set of experiments was performed after the field deployment. To avoid the errors associated with the bottle sampling procedure, as may have occurred in the previous calibration experiments, in these experiments a known quantity of sand was simply poured in front of the ABS transducer and then allowed to settle. An example of data from one run of such an experiment is displayed in figure 1-11. The range of settling velocities from 2.5 to 7 cm/s, corresponding to sediment sizes from 200 to 500  $\mu\text{m}$ , is clearly seen. The data shown in figure 1-11 are from an experiment performed with all the size fractions present in the LEO-15 bottom sample. Other experiments were performed by first sieving the sand with a 710  $\mu\text{m}$  diameter opening mesh to remove any small shell fragments. Very little sand was retained on this mesh, thus this could test if the small clam shell fragments would substantially impact the calibration results. Experiments were also performed on a per size class basis by using a set of  $1/2\phi$  spaced sieves to test the validity of the theoretical expressions for the size dependence of the scattering process.

Using this experimental technique with the full size distribution allows testing the calibration constant calculated from the pre-deployment experiments to see if this calibration factor will correctly predict the amount of sediment that is poured past the transducer. The previous calibration experiments derived a constant relating concentration to backscattered intensity. In this type of settling experiment, the mass of the sediment is known and not the concentration. However, if the concentration measured by the ABS is integrated over the appropriate volume then

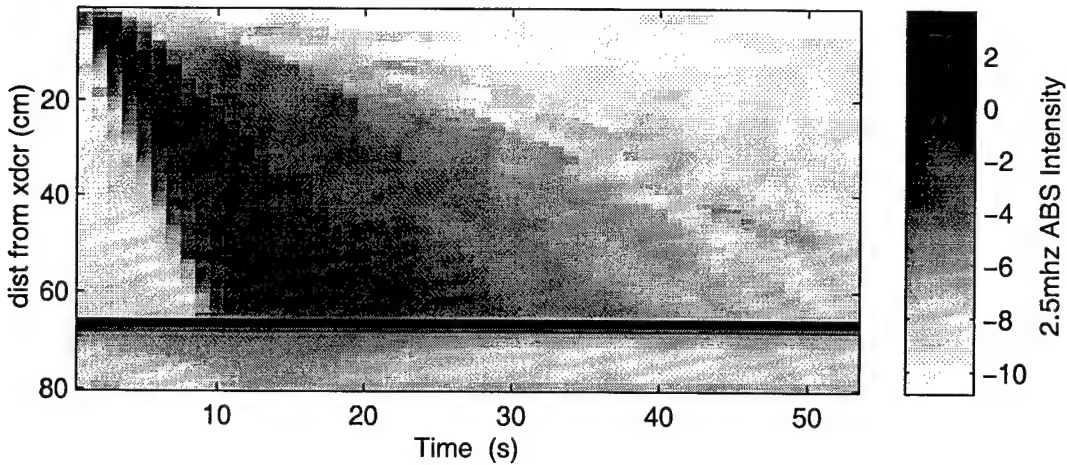


Figure 1-11 Example of 2.5 MHZ ABS data from the pour-in settling calibration experiment.

it should match the known sediment mass. As the sediment settles, it spreads out from the initial 2cm diameter opening that it is poured from. The width of the patch of sediment on the floor of the calibration tank was about 50 cm in diameter; thus all of the sediment is contained within the half power width of the ABS beampattern. Since the spreading rate of the sediment is roughly equal to the spreading of the ABS beam, the assumption of a uniform suspension is roughly valid. The cross sectional area of the sampling volume that is used to integrate the concentration estimate into a mass estimate is defined as a cone with radius  $r=5$  cm at  $z=10$  cm from the transducer expanding to  $r=26$  cm at  $z=80$  cm. The height of the sampling volume is defined by the 1 cm range resolution of the ABS instrument. Thus, the cross sectional area of sampling volume ( $A_s$ ) with units of  $\text{cm}^2$  is given by:

$$A_s(z) = 0.3 \left( z + \frac{20}{3} \right). \quad (\text{EQ 1.9})$$

A more sophisticated analysis would account for the true beampattern of the transducer, but this level of sophistication is probably unwarranted in this case because of the unknown variability of the sediment concentration across the beampattern sampling volume.

The amount of mass suspended during this type of settling test can calculated in two ways. The first method involves integrating across all the ABS depth bins at an instant in time when all the sediment has been poured in front of the transducer, but no sediment has reached the floor of the

tank. In the experiment shown in figure 1-11 this occurred 8 seconds into the record. The total mass in suspension can be found by

$$M_z = 1000 \int_z I_c(z) A_s(z_i) dz \quad (\text{EQ 1.10})$$

where  $I_c$  has units of g/l,  $A_s$  has units of cm<sup>2</sup>, and the factor of 1000 is used to convert liters to cm<sup>3</sup>. The quantity  $M_z$  was calculated for 5 runs of the settling experiment with the amount of sediment varied from 1 to 16 grams (figure 1-12). Both the full size distribution and the sand sieved through a 710μm mesh was used.

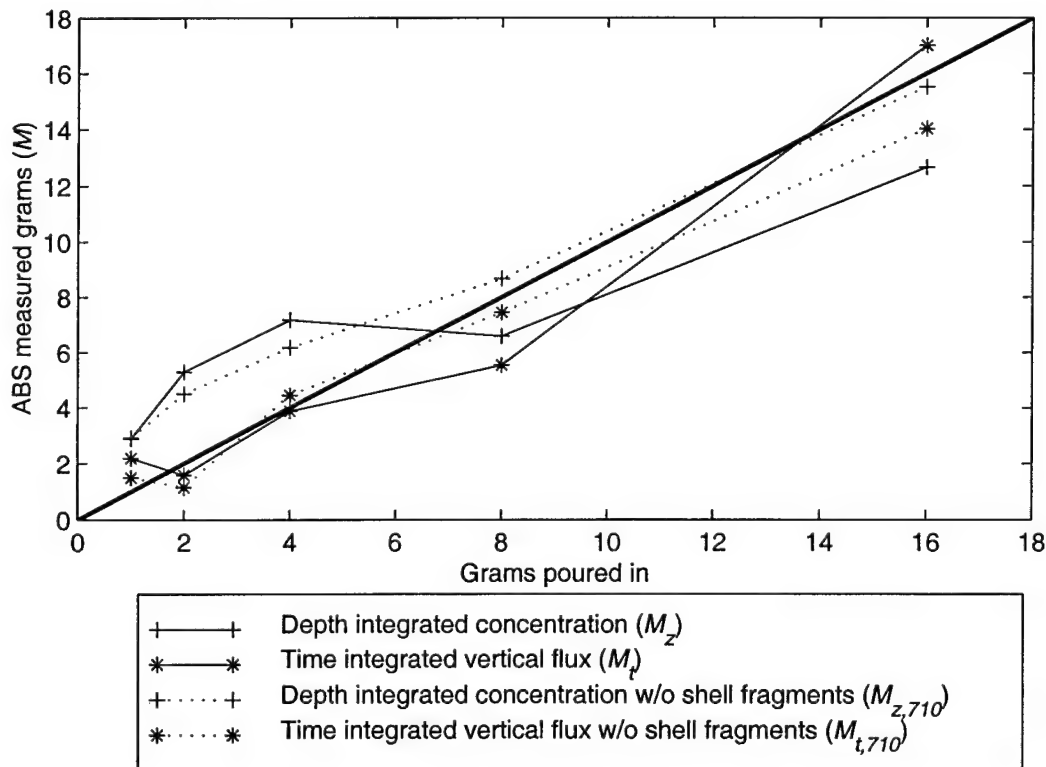


Figure 1-12 2.5 MHz ABS measured sediment mass calculated using the two procedures described in the text vs. the actual mass of sediment poured into the tank during the settling experiments. The thick solid line is the line of one-to-one agreement.

The second method of estimating the total mass of sediment is to pick a depth bin ( $z_i$ ) and temporally integrate the vertical flux through that depth bin.

$$M_t = 1000 \int_t I_c(z_i, t) A_s(z) w_f(z_i, t) dt \quad (\text{EQ 1.11})$$

In order to calculate flux the fall velocity ( $w_f$ ) is required. This can be calculated for a given depth bin simply from time difference between when the sediment was released ( $t_o$ ) and when it gets to the depth bin of interest.

$$w_f(z_i, t) = \frac{z_i}{t - t_o} \quad (\text{EQ 1.12})$$

This calculation for the total mass based on the temporal integral of vertical flux was performed for the same data sets as the previous calculation (equation 1.10) based on the depth integral of concentration. The results are shown in figure 1-12. It can be seen in this figure that both methods give a reasonable agreement between ABS measured sediment mass and actual mass poured into the tank, thus giving confidence in the validity of the calibration factor ( $K$ ) derived in the pre-deployment calibration experiments.

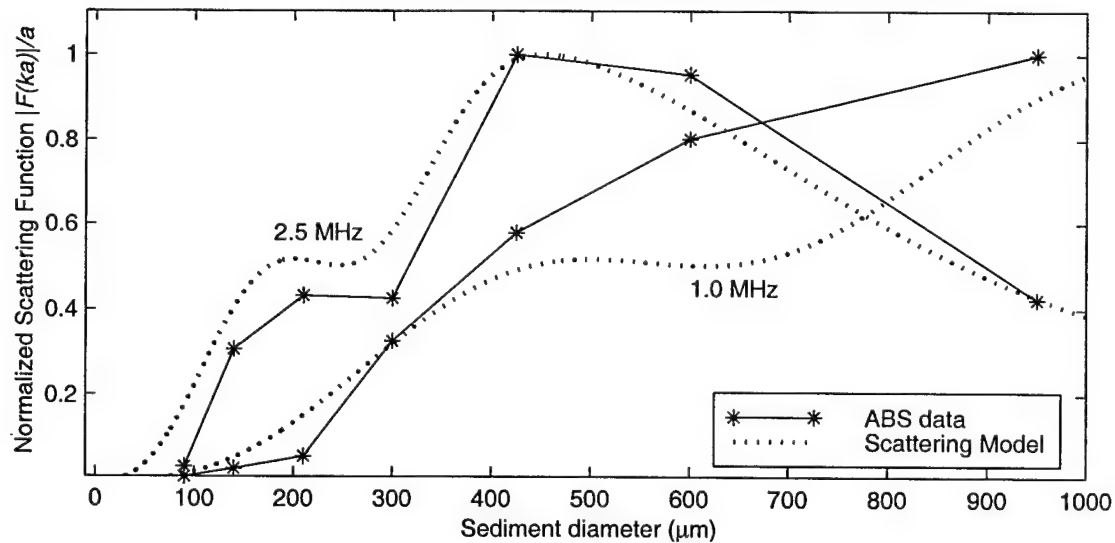


Figure 1-13 Size dependent scattering models and ABS data for 1.0 MHz and 2.5 MHz.

The final test of this calibration technique was designed to measure the size dependence of the scattering process and compare this with the theoretical/empirical expressions generated by Sheng and Hay (1988) and Thorne (1993). This was performed by sieving the bottom samples with a series of sieves separated by  $1/2\phi$ , where the  $\phi$  scale is related to metric size units by:  $d(\text{mm})=2^{-\phi}$ . The minimum sieve mesh size was 63 μm and the largest was 710 μm. For each size fraction the same mass of sediment was poured in front of the ABS transducer. The results from this set of experiments is shown in figure 1-13. For the 2.5 MHz transducer the results are

excellent, with both the general structure and the detailed structure near  $ka=1$  being well reproduced by the scattering model. For the 1.0 MHz transducer the general structure is well reproduced but the detailed structure near  $ka=1$  present in the model is not visible in the data. However this structure would only be captured by the one data point near 600 $\mu\text{m}$ . To do this type of experiment more accurately, sieves separated by  $1/4\phi$ , such as those used by Sheng and Hay (1988), would be required. However, this test of the theoretical scattering model allows us to use the model with confidence for determining the amount of error the may occur in the concentration estimate due to uncertainty in the sediment size distribution.

#### 1.4.2 Inverse Problem

The objective of the general inverse problem is to find both the concentration and the size distribution of suspended sediment from multiple frequency or multi-angle acoustical and optical data. In the previous section, the constant ( $K$ ) was found to relate acoustic intensity at a given frequency to concentration, given a known size distribution. The size distribution is not known *a priori* in the field, nor is it likely to remain constant; thus an approach that takes this into account is required to estimate the concentration. If one had many acoustic frequencies, one could in theory perform a least squares inversion as described by Greenlaw (1979) for zooplankton size distributions. However, with only three frequencies, the least squares inversion becomes poorly conditioned. Hay and Sheng (1992) developed a method for inverting data from a three frequency (1, 2.25, 5.0 MHz) acoustic system with a sandy ( $D_{50} \sim 150 \mu\text{m}$ ) bottom. In this method the size distribution is assumed to be log normal with a fixed variance, thus the inverse solves for the mean size and concentration. In Hay's method, theoretical backscattering strengths over the range of possible mean sizes are calculated and are then used to find the mean size by matching ratios of theoretical scattering strengths at different frequencies to the same ratio based on data. Different ratios ( $I_5/I_{2.25}$  or  $I_{2.25}/I_1$ ) are used based on an initial size estimate from  $I_5/I_1$ , as well as the constraint of a unique solution for mean size. Using ratios has the advantage of eliminating system constants, and more importantly concentration dependence from the size estimate. Once a mean size has been determined, the concentration is calculated by using a theoretical relation between intensity and concentration given the estimated size distribution.

Unfortunately in the LEO-15 1995 deployment the 5.0 MHz ABSS system failed several days into the deployment so data is only available from the 1.0 and 2.5 MHz ABS system. With only these two frequencies the ratio of  $F_{2.5}(ka)/F_{1.0}(ka)$  does not allow for a unique inverse solution in the 200 to 600  $\mu\text{m}$  sediment size range found at LEO-15 (figure 1-14).

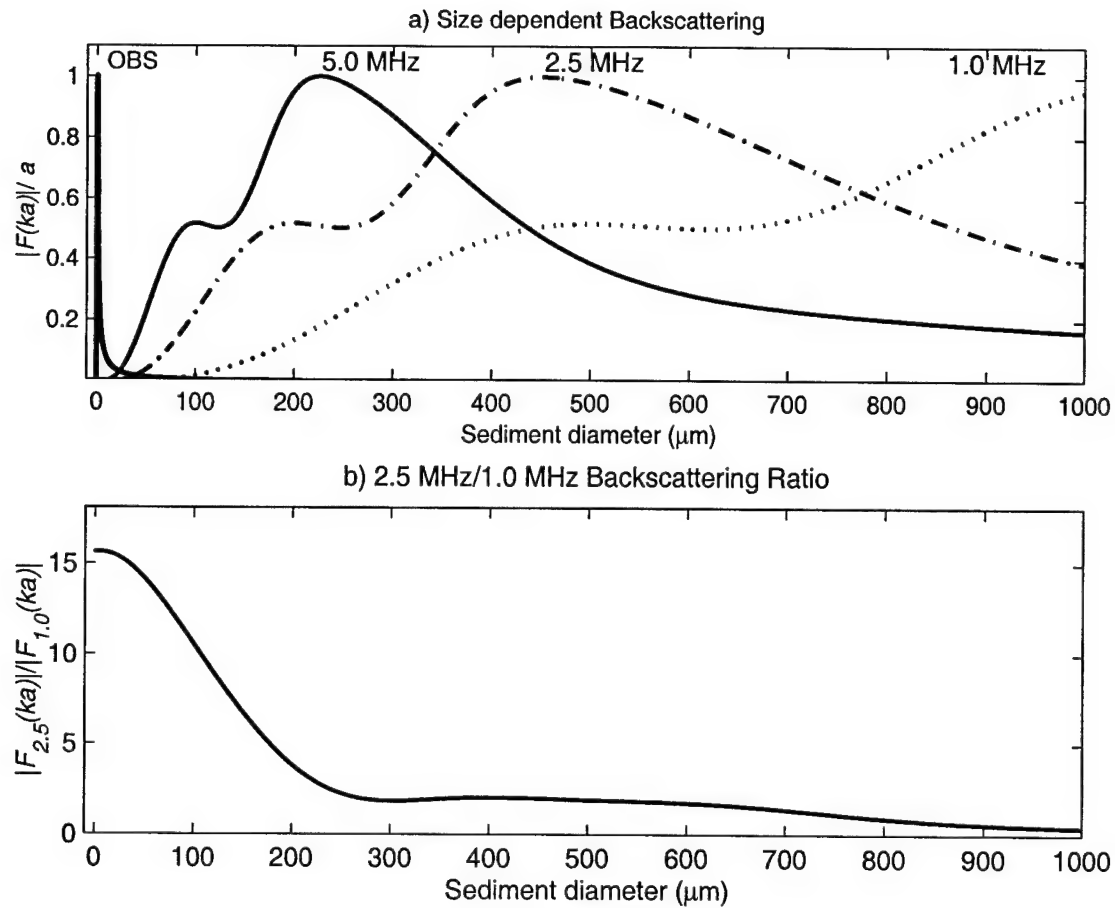


Figure 1-14 a) Size dependent backscattering intensities calculated by equation 1.3 and b) Ratio of backscattered intensities for the 2.5 MHz and 1.0 MHz transducers.

This technique of using ratios has also been successfully exploited by Lynch et al. using the 5.0 MHz ABSS system and an OBS instrument with fine sediment ( $<90 \mu\text{m}$ ). However, the OBS gives little useful information about scattering from 200 to 600  $\mu\text{m}$  in the presence of the small quantities of fine suspended sediment

Since an inverse for sediment size is not possible with the data collected at LEO-15, concentration estimates will be made using the 2.5 MHz ABS data alone. Fortunately the size distribution of the bottom sediment size distribution at LEO-15 is well matched to the size dependent scattering of the 2.5 MHz ABS instrument. In the next chapter an error analysis is discussed relating the potential error in the concentration estimate to the uncertainty in suspended grain size.

### 1.4.3 LISST

The LISST instrument also provides a method for determining the size distribution of suspended sediments. The general theory upon which the instrument is based is simple diffraction theory; small particles behave more like point scatterers, thus they have an angular distribution of forward scattered energy that is stronger at higher angles, while large particles generate a narrower angular distribution of forward scattered energy. The expected result from the settling test is that, as the larger particles settle out of suspension, the angular distribution of forward scattered energy shifts to higher angles. It is also expected that the transmission of optical energy increases as particles settle. In the pre-deployment calibration experiments, the transmission decreased and the angular distribution of energy remained relatively constant as sediment settled. The decreasing transmission may be due to the fact that the tank was not big enough to position the LISST with the lenses vertical so fine sediment may have been accumulating on the lenses. A thorough calibration and evaluation of the performance of the LISST instrument was performed after the LEO-15 deployment (Traykovski *et al.* 1998). These tests revealed that the LISST is presently unable to properly determine the sizes of sediment larger than 250  $\mu\text{m}$ , thus making it unsuitable for use with the sandy sediments at LEO-15. However, one of the LISST instruments was placed 1 m above the seafloor, so it may have been above most of the bursts of sand which were observed to rise to 40-60 cm in the ABS data. The transmission on this LISST sensor was well below 30% for most of the deployment, which is the maximum limit for correct interpretation of the LISST data (figure 1-15). Since the analysis in this thesis deals entirely with the sand sized sediments which dominate the bottom size distribution at LEO-15, LISST data will not be used in the context of this thesis.

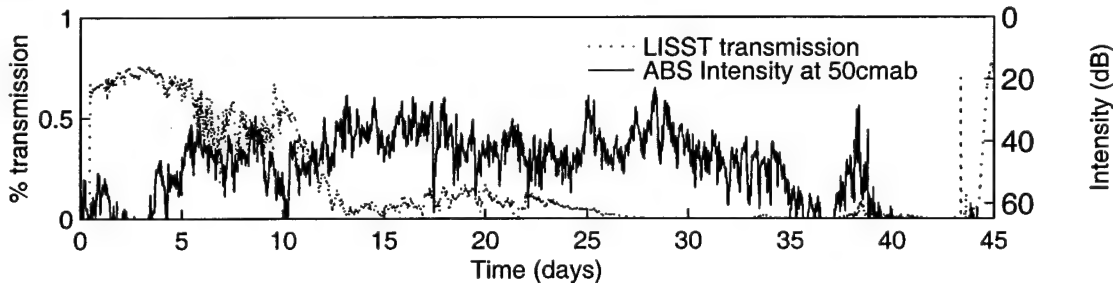


Figure 1-15 LISST transmission time series data and ABS intensity at 50cm above bottom.

### 1.4.4 Water velocity measurements

The EMCM current meters are calibrated in a standard fashion in a tow tank with tow speeds of 0,10,30,60 and 90 cm/s on either axis. In the most recent LEO deployment the EMCM sampled

every 1/2 hour for 4.25 minutes at 4 Hz. To interpret the EMCM record the 4.25 minute bursts are averaged to estimate x and y components of current velocity. This mean is then subtracted to examine the wave properties. The simplest wave description would be the r.m.s. velocities combined with a dominant period. Other important statistics include the skewness of the velocity distribution which can be used as a measure of wave steepness. These parametrizations will be discussed in detail in chapter 2.

With only two directional channels it is impossible to get a complete representation of the wave directional spectrum. However, it is possible to obtain a low resolution estimate of the directional spectrum. A method of looking at the temporal/directional spectrum is to decompose the x and y velocity records into frequency bands using an fft and then form rotary spectra to represent the water velocity in each frequency band. The advantage of this method is that it gives a direction for each frequency band, and can resolve multiple direction swells if they have different periods. A simpler method of calculating dominant wave direction is to calculate the total energy in each perpendicular axis of the current meter output and then rotate the coordinate system until the energy in one direction is minimized and energy is maximized in the other. This directional information is important when looking at the evolution of the bedforms as imaged by the Sector Scanning Sonar.

To interpret the acoustic and optical sediment concentration records in terms of sediment resuspension dynamics, knowledge of the bottom stress is required. In the 1995 LEO deployment only one EMCM functioned properly; thus no velocity shear measurements are available from this instrument. However, a BASS array measured current velocity at 44, 80, 166 and 250 cm above bottom. Richard Styles (pers. comm.) of Rutgers University has reported that the velocity data are well fit by logarithmic profiles thus the bottom stress due to the current can be measured. Unfortunately, there is not any data available to measure velocity shear in the wave boundary layer, so the instantaneous bottom stress due to the combination of waves and current must come from water velocity measurements and a boundary layer model. Appropriate models will be discussed in section 1.5 of this chapter.

#### **1.4.5 Sector Scanner Image Processing**

The unique property of the rotary side scan sonar system is that it does not need to be closely calibrated to give information on the spatial structure of the bottom roughness, if the roughness elements are substantially larger than the sonar's spatial resolution (approximately  $1 \text{ cm}^2$ ). This is

the case at LEO-15 since the roughness elements are typically large ripples with heights of 5 to 20 cm and wavelengths of 15 to 120 cm.

A central goal of this thesis will be to understand how the observed bedforms effect sediment resuspension dynamics. With this in mind, the parameters that need to be measured from the image are: the ripple wavelength, the ripple height, the spatial relation between the ABS beam and the ripple phase. Since it is possible to map where the ABS beam is located on the SSS image, the height of the ripples can be found from the ABSS/ ABS bottom return. The other parameters can be simply measured manually from the image. These issues will be discussed in depth in chapter 2.

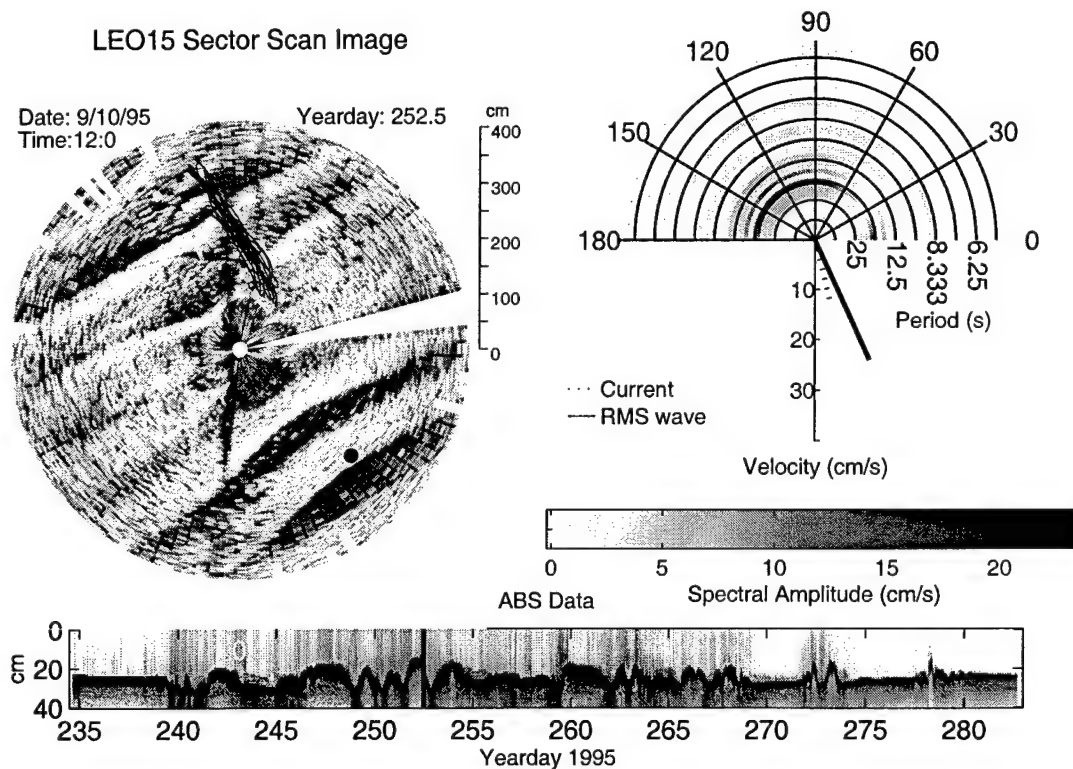


**Figure 1-16** In the top left a Sector Scanner Image is shown with some of the largest ripples (1.0m wavelength, 15 cm height) in the deployment. The black line represents the trajectory of a water particle due to surface wave motions during a 4.25 minute EMC burst. The typical scaling of orbital excursion distance = 1 to 2 times the ripple wave length is visible. The black dot is a arbitrary reference point used in viewing a movie of these images (<http://www.oal.whoi.edu/~petetray/leo15.html>) The plot in the upper right displays a direction/ period spectrum of the surface wave field. Here the waves have periods of 18s and the direction lines up with the ripples. This plot also displays the r.m.s wave velocity and current velocity using the vertical scale (cm/s). The lower plot of the ABS data shows a time series of bottom elevation as ripples migrate past the ABS beam. The vertical line indicates when the sector scan image was taken from the time series

## **1.5 Review of sediment transport modeling**

Typically what is desired from a sediment transport model is to input a minimum set of oceanographic and bottom parameters from which the model returns the amount of sediment in suspension and the net sediment transport. A typical oceanographic input data set includes wave parameters (amplitude, period, direction) and current speed and direction relative to the waves. The required sediment parameters are often the bottom size distribution, sediment density and fall velocity, and critical stress for the initiation of motion.

The physical context in which the models work is displayed in figure 1-17. The figure is divided horizontally into two halves to show the difference between 1-d models and 2-d models. The left half shows a scenario with ripples much smaller than the wave orbital diameter spatial scale and modeling elements associated with a 1-d model. The right half shows wave orbital diameter scale ripples and a 2-d view of the sediment suspension process. With wave orbital scale ripples with sharp crests and energetic flows, vortex formation has commonly been observed (Sleath 1982). These vortices are formed in the lee of each ripple twice during each wave cycle during periods of maximum velocity and are capable of entraining significant amounts of sediment. As the wave velocity reverses the vortex and its entrained sediment is ejected upwards into the main flow where it can be advected by the wave orbital velocities. The 2-d approximation is made since ripples are often long and parallel. However, the flow produced by these ripples probably has substantial 3-d variability and structures. The observation of the 3-d structure of the suspended sediment field remains as a topic for future research and instrument development.

### **1.5.1 1-d Models**

Some of the more commonly used models for sediment transport on the continental shelf are those developed in the late 70's and early 80's by Glenn, Grant and Madsen (GM Models)(1991). These models account for wave current interaction, ripple formation and degradation, and sediment induced stratification. The basic core of the model has two systems of equations, one describing the sediment part of the system, and the other describing the fluid flow. An eddy viscosity turbulence closure scheme is used in both systems to relate turbulent momentum and sediment flux to velocity shear and sediment gradients respectively. This eddy viscosity is typically chosen to be time invariant, although these models have been compared to models that include a time variable eddy viscosity (Trowbridge and Madsen, 1984) with the result that for linear waves the small differences in bottom stress predicted by a time dependent eddy viscosity model are probably overshadowed by errors in roughness estimates.

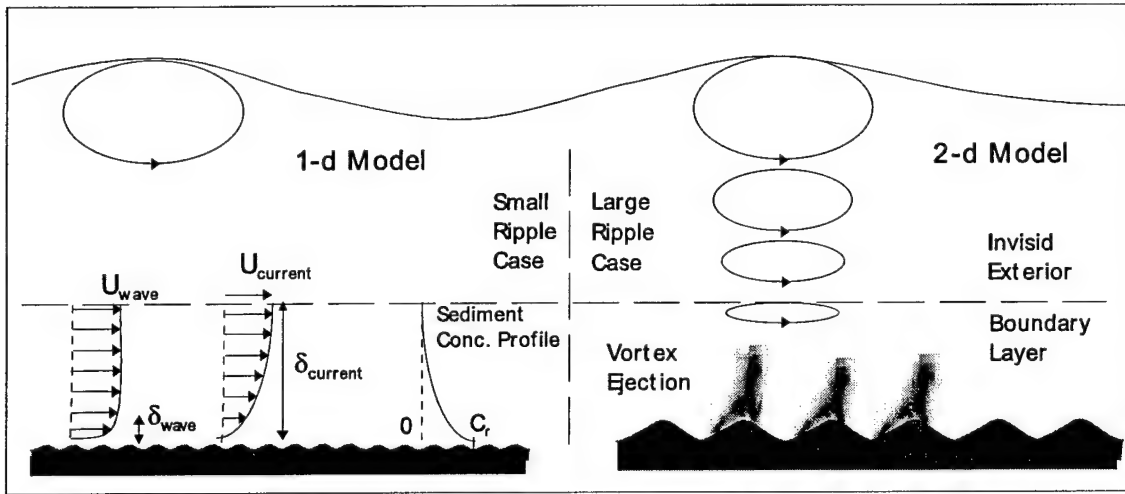


Figure 1-17 In the 1-d models vertical profiles of velocity and sediment concentration are formed then multiplied and integrated to model transport. When the roughness elements have heights larger than the wave boundary thickness ( $\delta_{wave} \sim 1 - 10\text{cm}$ ) and horizontal scales on the order of the wave orbital distance, 2-d models that resolve the lee vortex ejection from each ripple may be more appropriate.

The models are typically 1-d since the horizontal scale associated with the wavelength of the surface waves allows the horizontal convective terms to be ignored in a order of magnitude analysis of the horizontal momentum balances. This 1-d assumption also requires the bottom roughness to have a horizontal length scale that is much smaller (or much larger) than the wave excursion distance so the roughness can be parameterized by a r.m.s. roughness height as shown in the left half of figure 1-17. This is not the case at LEO-15 where the ripples have wavelengths of up to 1.0 m.

The physical model for the fluid part of the 1-d system is that of a thin oscillatory wave boundary layer within a thicker steady current boundary layer. The thickness of the wave boundary layer is determined by the bottom shear stress and the temporal frequency of the waves. It is typically a few centimeters in thickness; thus the definition of a wave boundary layer becomes problematic at a site such as LEO-15 where the bedforms have heights of 10 to 15 cm. In terms of sediment dynamics, the important results from the fluid analysis are the bottom stress which forces the sediment resuspension, and the amount of mixing as determined by the flow-dependent eddy viscosity. The bottom stress calculated by this type of model is time dependent, but does not vary in space along the ripple profile.

The sediment part of the problem starts with initiation of motion. Initiation of motion is typically determined by a critical bottom stress  $\tau_{cr}$  determined as a function of sediment properties from a modified Shields diagram which gives the function  $F$  in equation 1.13. (Madsen and Grant, 1976)

$$\Psi_{cr} = F(S^*)$$

$$\Psi_{cr} = \frac{\tau_{cr}}{(s-1)\rho gd} \quad S^* = \frac{d}{4v} \sqrt{(s-1)gd} \quad (\text{EQ 1.13})$$

The sediment and water properties are: the sediment to water density ratio  $s = \rho_s/\rho$ , sediment diameter  $d$ , and the water viscosity  $v$ . According to this model, sediment is set in motion when the bottom stress exceeds the critical stress. In the 1-d models, which treat the bedforms as a statistical roughness height, skin friction stress, based on grain roughness, is used for the bottom stress for initiation of motion calculations since part of the total bottom stress is due to form drag on the bedforms.

Once sediment is in motion, the amount available to go into suspension is determined by a reference concentration boundary condition for the sediment concentration profile. This reference concentration  $c_m(z_r)$  is given by

$$c_{rn}(z_r) = \gamma C_{bn} \left( \frac{|\tau'_b|}{\tau_{cr}} - 1 \right). \quad (\text{EQ 1.14})$$

Here  $C_{bn}$  is bed concentration in the  $n$ th size class,  $\tau'_b$  is the skin friction bottom shear stress, and  $\gamma$  is an empirical constant and  $z_r$  is the height where this boundary condition is applied. The total sediment concentration  $c$  is related to the concentration in the  $n$  classes ( $c_n$ ) and the continuous size distribution function  $n(a)$  by

$$c = \sum_n c_n \approx c \int_a^{\infty} n(a) da. \quad (\text{EQ 1.15})$$

Typically  $z_r$  is chosen as seven grain diameters, but this is inconsistent among different researchers, leading to difficulty in comparing reference concentrations. The 1-d vertical sediment concentration profile is determined by a balance of upward eddy diffusion mixing and downward gravitational settling  $w_{fn}$  for the  $n$ th size class.

$$\frac{\partial c_n}{\partial t} = w_{fn} \frac{\partial c_n}{\partial z} + \frac{\partial}{\partial z} \left( v_t \frac{\partial c_n}{\partial z} \right) \quad (\text{EQ 1.16})$$

This equation is typically solved by assuming a steady state solution ( $\partial c_n / \partial t = 0$ ) over a suitable averaging period and eddy viscosity  $v_t$ , based on the fluid analysis. With a simple linear eddy viscosity given by

$$v_t = \kappa u_* z \quad u_* = \sqrt{|\tau_b|/\rho} \quad \kappa = 0.4 \quad (\text{EQ 1.17})$$

the sediment concentration profile becomes the classic Rouse profile:

$$c_n(z) = c_{rn}(z_r) \left( \frac{z}{z_r} \right)^{-w_{fr}/\kappa u_*} \quad (\text{EQ 1.18})$$

More complicated eddy viscosity models to reflect the different scales of the wave, current and transitional boundary layers have been suggested by Madsen (1991) and others (for a review see Sleath, 1990). Once a sediment profile and a velocity profile have been found, transport can be calculated by multiplying the two quantities and integrating in depth. One of the assumptions of this type of model is that the surface gravity waves velocities are well represented by linear sinusoidal waves. This causes no sediment to be transported by the waves; the waves only help to suspend the sediment which is transported by the current. The vortex ejection models, if forced with non-linear waves, are very different in this respect.

With regards to the amount of sediment in the water, one of the important parts of this model, as discussed in the literature, is the reference concentration. Issues have included: what value of  $\gamma$  should be used, should  $\gamma$  be constant at all, or should  $\gamma$  depend on some other parameters such as bottom roughness or stress. In their original model Grant and Glenn (1983) suggest that a value of 0.002 for rippled beds. Several authors suggest that this proportionality constant decreases as a function of increasing stress. Vincent (1991) used measurements taken from a 2.8 MHz backscatter device deployed in a fine sand environment (median grain diameter,  $D_{50} \sim 180 \mu\text{m}$ ) to estimate a  $\gamma$  averaged over several wave periods. They found that  $\log_{10}(\gamma)$  decreased from -2 to -4 over an order of magnitude increase in excess shear stress. They hypothesized that this variation in resuspension was due to changing ripple steepness on the wave group time-scale, and that steeper ripples could more efficiently eject sediment carrying vortices. Unfortunately they had no direct observations of the bedforms. While the reference concentration boundary condition is well suited for the gradient diffusion models, other types of models, such as advective models use a flux bottom boundary condition.

### 1.5.2 Vortex ejection models

As mentioned previously, when the ripple wavelength scales become of the same order as the wave orbital diameter scale, the 1-d models may be able to describe the temporally and spatially averaged sediment concentration profile given the right eddy viscosity model, but they do not capture the 2-d time dependent physics of the vortex ejection process. Several types of models that account for these processes have been presented in the literature. They range from simple “grab and dump” models, which calculate the amount of sediment picked up in each vortex and simply place it some distance away, to complicated 2-d numerical discretization of the equations of motion for water and sediment over wave-orbital scale rippled beds. In Nielsen’s (1988) paper entitled “Three simple models of wave sediment transport” he examines three models which explicitly account for the vortex ejection process. Since these models attempt to describe the elements of the vortex ejection process, and thus will form part of the basis for this thesis work, they are reviewed in some detail.

#### 1-d time dependent boundary condition diffusion model

Nielsen’s diffusion model retains many of the same components as the 1-d steady state models discussed in the previous section. The most important difference is his treatment of the bottom boundary condition. Instead of using a time dependent reference concentration he uses a time dependent flux condition called a “pick up function.” The time dependence reflects the vortex ejection process by only allowing sediment to enter the water at the instant of wave velocity reversal. If one assumes equilibrium or averages over a long enough time period, the pick up function can be related to the reference concentration by:

$$\bar{p} = w_f \bar{c}_r \quad (\text{EQ 1.19})$$

where the overbar indicates a time average,  $w_f$  is the average settling velocity, and  $p$  has units g/m<sup>2</sup>s. On an instantaneous basis the pickup function in the diffusion equation can be expressed as diffusive flux from the bottom:

$$p(t) = v_t \frac{\partial c}{\partial z} \quad (\text{EQ 1.20})$$

Nielsen’s pick up function is cast as a function of the Shields parameter (scaled bottom stress):

$$p = F(\psi) \quad \psi = \frac{\tau_b}{(s-1)\rho gd} \quad (\text{EQ 1.21})$$

For flow over vortex ripples (as in LEO-15), based on a variety of data for  $\bar{C}_r$  and using equation 1.19, Nielsen suggests

$$\bar{p} = 0.005 w_f \psi_r^3 \quad \psi_r = \frac{\Psi}{(1 - \pi \eta / \lambda)^2} \quad (\text{EQ 1.22})$$

where  $\eta$  is ripple height,  $\lambda$  is ripple wavelength, and the factor  $1 - \pi \eta / \lambda$  accounts for potential flow enhancement over the ripple crests. Here the overbar indicates averaging over many wave periods. Unlike other models there is no critical stress for initiation of motion in this formulation although the third power dependence makes the curve much steeper for larger stresses. To account for the time dependence (within the wave cycle) of the vortex ejections the pick up function becomes:

$$p(t) = 0.005 w_f (0.5 \psi_{rf}^3 \delta(t - t_d) + 0.5 \psi_{rb}^3 \delta(t - t_u)) \quad (\text{EQ 1.23})$$

where  $\psi_{rf}$  and  $\psi_{rb}$  are the maximum forward and backward Shields parameter to account for wave asymmetry and  $t_d, t_u$  are the times of down and up zero-crossing velocities. Given this boundary condition, Nielsen solves the diffusion equation analytically for time dependent sediment concentration profiles by representing the delta functions as a sum of periodic functions. Since only the boundary condition from this model will be used in this thesis, the solution to the time dependent diffusion equation is not discussed in further detail.

### 1-d Heuristic entrainment model

This model uses the boundary condition as described in the 1-d time dependent diffusion model, but it describes the vertical distribution of suspended sediment in terms of a probability function for the height of entrainment ( $z_e$ ) exceeding a height  $z$ . The entrainment process is considered to be instantaneous as sediment is carried to its maximum height upon ejection. Thus at any level  $z$  the balance between time-averaged settling flux and entrainment flux is

$$w_f \bar{c}(z) = \bar{p} P(z_e > z). \quad (\text{EQ 1.24})$$

Breaking the sediment concentration profile  $\bar{c}(z)$  into a distribution function  $F(z)$  and a reference concentration  $\bar{c}_r(z_r)$  results in  $P(z_e > z)$  being equal to  $F(z)$ . Immediately after a vortex ejection the amount of freshly entrained sediment is:

$$m_i(t_i) = \int_p(t) dt = p(t)|_{t=t_i} \quad (\text{EQ 1.25})$$

and any later time the total amount in suspension is:

$$m(t) = \sum_i P(t_i) \int_{w_f(t-t_i)}^{\infty} F(z) dz . \quad (\text{EQ 1.26})$$

Nielsen assumes an exponential profile for  $F(z)$  based on data, which simplifies this expression and allows for flux calculations given a suitable transport velocity. The sum over  $i$  only needs to be evaluated from the most recent event back several events if the sediment has a sufficiently large fall velocity. This expression is very useful for analyzing our LEO-15 data, since it closely resembles what we actually measure on an instantaneous basis. More detailed models attempt to give  $F(z)$  a better physical basis in terms of the eddy ejection process.

### **2-d Grab and dump transport model**

The above models resolve the temporal structure of the ejection process, but do not address the 2-d spatial structure of the suspended sediment associated with the ripples. Nielsen suggested a third model which accounts for the 2-d structure of the transport process. In this model the amount of sediment “grabbed” is described by the same pick up function and then this sediment is simply “dumped” an average distance of one wave orbital excursion in the opposite direction of the entrainment velocity. Thus this model does not account for any of the vertical structure of the suspended sediment, yet when all three models results were compared to flume data for sediment transport under waves, the grab and dump model provided the best fit for larger sand sizes ( $w_f/U_{wave} > 0.25$ ). All models performed equally well for the smaller sediment sizes, which could possibly be explained by the fact that the smaller sediment sizes staying in suspension for more than one wave cycle. The fact that the grab and dump model works well for larger grain sizes in a laboratory environment with vortex ripples indicates that this may be an appropriate model to use for wave forced sediment transport at LEO-15.

### **Fully 2-d numerical models**

For a more detailed picture of the flow which does not parametrize the vortex formation and ejection process, but actually resolves the eddies that form at the ripple crest, one is forced to use 2-d dimensional numerical models such as those developed by Longuet-Higgins (1981), Blondeaux and Vittori(1991), and most recently Hansen, Fredsøe, and Deigaard (1994). In these models discrete vortices are generated in the thin wave boundary layer and are then released in the inviscid main flow. In the Longuet-Higgins model, the main flow is calculated from a 2-d analytical solution of potential flow over the rippled boundary plus the contributions from the discrete vortices. In the other two numerical models the vortices are not simply added to potential

flow away from the boundaries, but interact with the main flow through the Poisson equation. This makes them much more computationally intensive, but allows a more realistic treatment of viscous effects. Hansen's model includes a sediment component which uses a boundary layer model to calculate how much sediment is introduced into the main flow, and then allows the eddy structure of the main flow to determine the spatial structure of the suspended sediment field. Sediment grains in the main flow are tracked individually in a Lagrangian manner.

### **Sediment trapping by vortices**

An important part of any model that includes vortex ejection is to determine how effective these vortices are at trapping and advecting sediment. In Nielsen's (1984) paper entitled "On the motion of Suspended Sand Particles" he discusses this issue in some depth. The picture that emerges from this analysis is that sediment particles with settling velocities smaller than the maximum velocities in the vortex are trapped by the vortex and do not settle until released. The following picture (figure 1-18, upper panel) with water particle vortex motion as a solid body rotation shows how this works. The vector motion of the sediment particle is a vector addition of its fall velocity and the water motion. Thus if  $w_f$  is less than or equal to  $u$  (the upward water velocity) sediment can be trapped in the vortex. For more realistic vortex motions the sediment paths are not perfect circles as shown here, but the sediment paths are still closed, indicating trapping. Observational support for this type of trapping is evident from experiments where vertical profiles are compared for different size sediments. Diffusion based theories would predict different concentration depth profile slopes for different sized sediment. Nielsen's observed results show similar slopes for different sized particles, as long as the settling velocity is less than the vortex velocity, which is consistent with sediment trapping.

One important part of the thesis work is to attempt to determine how much complexity must be retained in the models to accurately predict sediment transport in the environment present at LEO-15. One reason for a simplified 2-d model is that such a model may capture the important physics without resorting to cumbersome numerical techniques. Perhaps, a more significant argument for a simplified 2-d model is that the vortex ejection process most likely has 3-d structures even with a "2-d" bottom of elongated ripples. It may be possible that the detailed 2-d numerical models which try to accurately describe the vorticity field are missing the 3-d structures, which are important for a detailed description of the vertical mixing process, yet the detailed 2-d numerical models may be more complicated than is required to predict transport due to the vortex ejection process. The application of a 2-d model is discussed in depth in chapter 3.

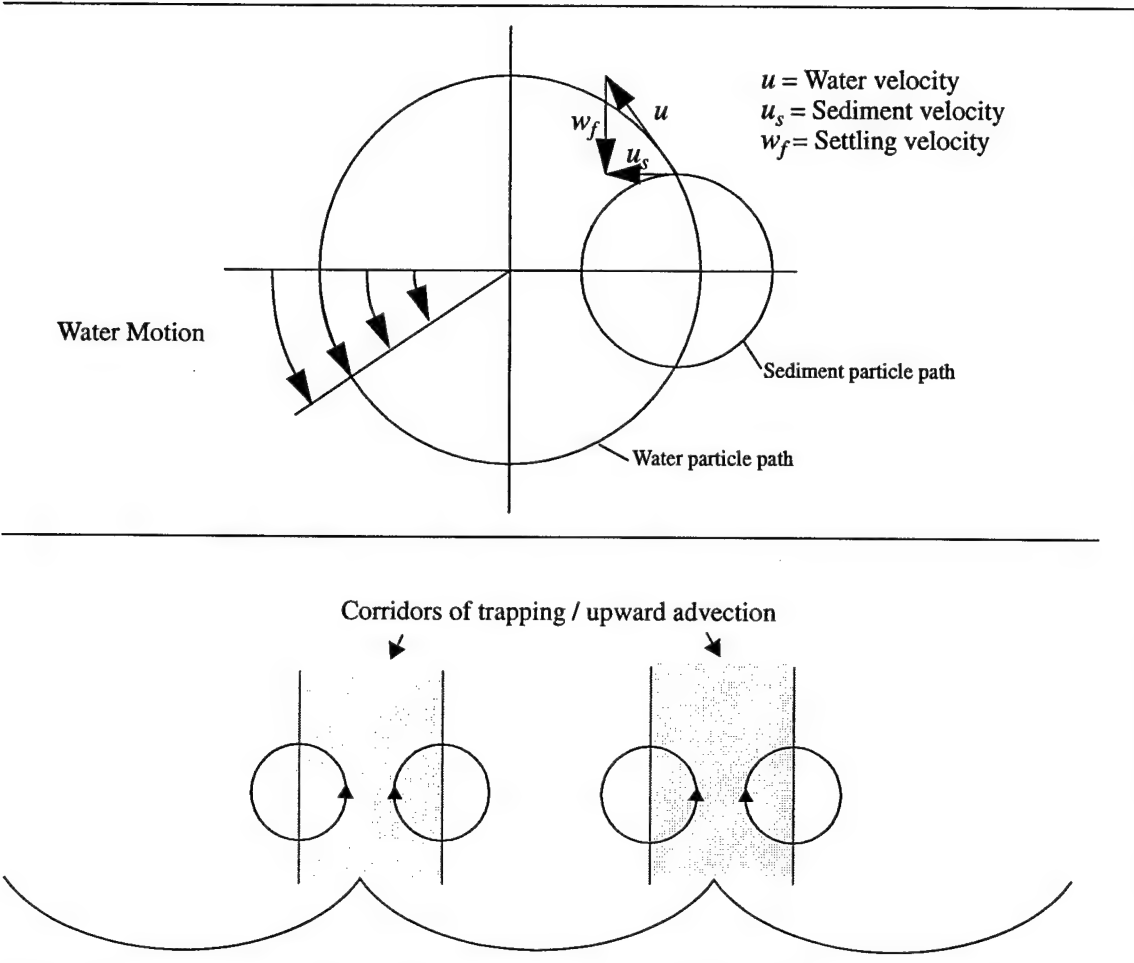


Figure 1-18 Sediment trapping by vortices. The upper half of the figure shows how the combined vector motion of sediment fall velocity and water vortex motion leads to sediment trapping. The lower half shows a system of vortices and corridors of sediment trapping and/or upward advection over a rippled bed.

## 1.6 Outline of thesis

The following three chapters are presented as papers that are to be published in the literature. The next chapter entitled “*Geometry, migration, and evolution of wave orbital ripples at LEO-15*” has been submitted to the *Journal of Geophysical Research*. This paper discusses observations of the bedforms at LEO-15 made with the Sector Scanning Sonar in terms of relevant physical forcing parameters. The geometry of the observed ripples is compared to existing empirical models for predicting ripple geometry. The temporal evolution of the ripple geometric properties during storm events is compared to previous observations reported in the literature. The interactions of the flow dynamics and the geometry of the ripples may have important ramifications to the sediment transport mechanisms. Two of the mechanisms that are examined in this paper are the observed

ripple migration record, and the wave forced suspended sediment transport. A combination of modeling of the unobserved bedload transport and observations of wave forced suspended sediment transport are used to relate the ripple migration to water velocity forcing parameters.

The third chapter entitled "*Wave forced sediment transport mechanisms over vortex ripples*" begins with examining models for wave forced suspended sediment transport due to the vortex ejection mechanism. The observational basis for these models is presented in detail, and transport predicted by the models is compared to measured transport. Models for sediment transport due to mean currents are also examined and compared to observations. At this stage, models for bedload transport and suspended transport due to wave velocities and suspended transport due to mean currents have been developed and tuned with observations. These models are forced with a 1.5 year current meter record to determine what the dominant sediment transport mechanisms are on the crest of a sand ridge such as the LEO-15 site on Beach Haven ridge.

Finally, since bedload or saltation load forced by wave orbital velocities may play a major role in forcing ripple migration, but was not directly observed in this study due to lack of a suitable measuring technique, a study was conducted to develop instrumentation to measure this mode of transport. An appendix, entitled "*A initial study on using full spectrum pulsed doppler to measure sand transport on and near the seafloor,*" describes the development of an instrument designed to measure the upper layer of bedload, and saltation load transport.

## References

- Agrawal, Y.C., I.N. McCave, and J.B. Riley, "Laser diffraction size analysis," in *Principles, methods and applications of particle size analysis*, J.P.M. Syvitski, editor, Cambridge University Press, 1991, p. 119-128.
- Blondeaux, P., G Vittori, "Vorticity dynamics in an oscillatory flow over a rippled bed," *J. Fluid Mech.* **226** p.257-28 (1991)
- Craghan, M., "Topographic changes and sediment characteristics at a shore face sand ridge- Beach Haven ridge, New Jersey," Masters Thesis, Rutgers Univ., New Brunswick, New Jersey (1995)
- Drake, D.E. and Cacchione, D.A. "Estimates of the suspended sediment reference concentration ( $C_a$ ) and resuspension coefficient ( $\gamma$ ) from near-bed observations on the California shelf," *Cont. Shelf Res.*, **9** p. 51-64 (1989)
- Duane, D.B., M.E. Field, E.P. Meisburger, D.J.P. Swift, S.J. Williams, "Linear shoals on the Atlantic inner continental shelf, Florida to Long Island," in *Shelf Sediment Transport: Process and Pattern* edited by D.J.P. Swift, D.B. Duane, O.H. Pilkey, p447-498, Van Nostrand Reinhold, New York, (1972)
- Glenn, S.M., Grant W.D., "A continental shelf boundary layer model" vol. III, Users manual, technical report, 186 pp., Am. Gas. Assoc., Arlington, VA (1983)
- Greenlaw, C.F., "Acoustical estimation of zooplankton populations". *Limnol. Oceanogr.*, **24** p226-242 (1979)
- Hansen, E.A., J. Fredsoe, R. Deigaard, "Distribution of suspended sediment over wave generated ripples," Int. Symposium on the transport of suspended sediment and its mathematical modeling, Florence, Italy p. 111-128 (1991)
- Hay, A.E., "On the remote acoustic detection of suspended sediments at long wavelengths," *J. Geophys. Res.* **88**(c12), p7525-7542 (1983)
- Hay, A.E., "Vertical Profiles of suspended sand concentration and size from multifrequency acoustic backscatter," *J. Geophys. Res.* **97**(c10), p 15,661-15,677 (1992)
- Hay, A.E., A.J. Bowen "On the coherence scales of wave-induced suspended sand concentration fluctuations," *J. of Geophys. Res.* **99**(c6)p 12,749-12,765 (1994)
- Longuet-Higgins M.S., "Oscillating flow over steep sand ripples," *J. Fluid Mech.* **107** p.1-35(1981)
- Lynch, J.F., J.D. Irish, C.R. Sherwood, Y.C. Agrawal, "Determining suspended sediment particle size information from acoustical and optical backscatter measurements," *Continental Shelf Research*, **14**(10/11) p1139-1165 (1994)
- Madsen, O.S. and W.D. Grant, *Sediment Transport in the Coastal Environment, MIT Rep. 209*, 105 pp. Ralph M. Parsons Lab., Mass. Inst. of Technol., Cambridge, 1976

- Madsen, O.S., P.N. Wikramanayake, "Simple models for turbulent wave current bottom boundary layer flow," US Army Corps of Engineers Coastal Engineering Research Center Dredging Research Program contract report DRP-91-1(1991)
- Nielsen, P., "Dynamics and geometry of wave-generated ripples," J. of Geophys. Res., **86**(c7) p 6467-6472 (1984)
- Nielsen, P., "On the motion of suspended sand particles," J. of Geophys. Res., **89**(c1) p 616-626 (1984)
- Nielsen, P., "Three simple models of wave sediment transport," Coastal Eng. (12) p. 43-62 (1988)
- Osborne, P.D., and B. Greenwood, Frequency dependent cross-shore suspended sediment transport. 1. A non-barred shoreface, *Marine Geology*, 106, p 1-24, 1992
- Sheng, J. and A. E. Hay, "An examination of the spherical scatterer approximation in aqueous suspension of sand," J. Acoust, Soc. Am. **83** (2), p598-610 (1988)
- Sleath, J.F.A., "The suspension of sand by waves," J. of Hydraul. Res. 20(5), p. 439-451 (1982)
- Sleath, J.F.A., "Seabed Boundary Layers" The Sea, Ocean Engineering Science, Le-Mehaute-Bernard (editor); Hanes-Daniel-M (editor). John Wiley & Sons. New York, p693-727, 1990
- Thorne, P.D., "Analysis of acoustic measurements of suspended sediments," J. Geophys. Res. **98**(c1), p899-910 (1993)
- Thorne, P.D., "Constraining acoustic backscatter estimates of suspended sediment concentration profiles using the bed echo," J. Acoust, Soc. Am. (in press)
- Traykovski, P., R.J. Latter, and J.D. Irish, "A laboratory evaluation of the LISST instrument using natural sediments," Submitted to Marine Geology (1998)
- Trowbridge, J., and O.S. Madsen, "Turbulent wave boundary layers, 1. Model formulation and first order solution," J. Geophys. Res. **89**(c5), p. 7989-7997(1984)
- Trowbridge, J., "A mechanism for the formation and maintenance of shore-oblique sand ridges on storm-dominated shelves," J. Geophys. Res. **95**(c8), p. 16,071-16086 (1995)
- Vincent, C.E., D.M. Hanes, A.J. Bowen, "Acoustic measurements of suspended sand on the shoreface and control of concentration by bed roughness," Mar. Geol., **96** p1-18 (1991)
- Vincent, C.E., M.O. Green "Field measurements of the suspended sand concentration profiles and fluxes and of the resuspension coefficient  $\gamma_0$  over a rippled bed," J. of Geophys. Res. **95** (c7) p. 11,591-11,601(1990)
- Wiberg, P.L., D. E. Drake, D. A. Cacchione, "Sediment resuspension and bed armouring during high bottom stress events of the northern California inner continental shelf: measurements and predictions," Cont. Shelf Res. 10(14) p 1191-1219, (1994)
- Wiberg, P.L., C.K. Harris, "Ripple geometry in wave dominated environments," J. of Geophys. Res. **99** (c1) p. 775-789(1994)

## CHAPTER 2

### Geometry, migration, and evolution of wave orbital ripples at LEO-15

Peter Traykovski, Alex E. Hay\*, James D. Irish and James F. Lynch

*Dept. of Applied Ocean Physics and Engineering, Woods Hole Oceanographic Institution, Woods Hole, MA.*

*\*Dept. of Oceanography, Dalhousie University, Halifax, NS*

#### Abstract

Observations of the temporal evolution of the geometric properties and migration of wave formed ripples are analyzed in terms of measured suspended sand profiles and water velocity measurements. Six weeks of bedform observations were taken at the sandy (medium to coarse sized sand) LEO-15 site located on Beach Haven ridge during the late summer of 1995 with an autonomous rotary sidescan sonar. During this period six tropical storms, several of hurricane strength, passed to the east of the study site. Ripples with wavelengths of up to 100 cm and with 15 cm amplitudes were observed. The predominant ripples were found to be wave orbital scale ripples with ripple wavelengths equal to 3/4 of the wave orbital diameter. Although orbital diameters become larger than 130 cm during the maximum wave event, it is unclear if a transition to non-orbital scaling is occurring. Ripple migration is found to be directed primarily onshore at rates of up to 80 cm/day. Suspended transport due to wave motions, calculated by multiplying acoustic backscatter measurements of suspended sand concentrations by flow velocity measurements, are unable to account for a sufficient amount of sand transport to force ripple migration, and are in the opposite direction to ripple migration. Thus it is hypothesized that the onshore ripple migration is due to unobserved bedload transport or near bottom suspended transport. Bedload model calculations forced with measured wave velocities are able to predict the magnitude and direction of transport consistent with observed ripple migration rates. Sequences of ripple pattern temporal evolution are examined showing mechanisms for ripple directional change in response to changing wave direction, as well as ripple wavelength adjustment and erosion due to changing wave orbital diameter and relative wave to current velocities.

#### 2.1 Introduction

Bottom bedforms are an important part of the interactions between bottom boundary layer hydrodynamics and sediment transport. In particular wave formed ripples are the predominant bedform found in many coastal locations where the water is shallow enough to allow wave stresses to dominate over those caused by mean currents.

Previous laboratory studies such as those by *Bagnold* [1946], *Carstens et al.* [1969], *Mogridge and Kamphuis* [1972], and *Miller and Komar* [1980a] and field studies such as those by *Inman* [1957], *Dingler* [1974] and *Miller and Komar* [1980a] have led to a wealth of data on ripple geometry that has been recently reexamined by *Wiberg and Harris* [1994]. In *Clifton and Dingler* [1984] three

different classes of ripples are identified. Orbital scale ripples have wavelengths ( $\lambda$ ) that scale directly with the wave orbital diameter ( $d$ ). Anorbital ripples have wavelengths that depend on grain size ( $D$ ) alone. Suborbital ripples are a transitional stage between these two states and depend on both  $d$  and  $D$ .

Most of the previous observations have been conducted by divers which limits the temporal sampling. Alternatively, photographic systems have been used and have been able to produce time series of ripple evolution and occasionally ripple migration rates [Boyd *et al.*, 1988]. The photographic time series measurements by Wheatcroft [1994], Boyd *et al.* [1988], and Amos *et al.* [1988] of the seafloor have been used to investigate the relative roles of waves and mean currents in forming different types of bedforms in varying oceanographic conditions. However, photographic systems are often unable to produce adequate images during periods of high suspended sediment concentration [Wheatcroft, 1994]. Recently rotary sidescan sonar systems such as that described by Hay and Wilson [1994] have been used to measure bedform evolution in locations where a cable to shore is possible. We have adapted this type of sidescan sonar system for autonomous use on the continental shelf.

This rotary sidescan sonar system allows high resolution, rapid sampling of bedform morphology and migration over extended periods. The tripod on which this sidescan sonar system was mounted also contained current meters and acoustical and optical sensors to measure sediment concentrations. This system was deployed from August 24th to September 9th, 1995 at the Long Term Ecosystem Observatory (LEO-15) site off the coast of southern New Jersey (figure 2-1). During this time period six tropical storms, some of which attained hurricane strength, passed to the east of the study site. The geophysical environment at LEO-15 consists of a system of sand ridges extending north and east from the coast. The LEO-15 site is located in 11 m deep water on the southern end of Beach Haven ridge (shown as the closed contour in figure 2-1). These ridges consist largely of medium sand on top of a bed of holocene lagoonal mud between the ridges [Duane *et al.*, 1972].

The purpose of this paper is to analyze these observations of bedforms in the context of previous observations of wave formed bedforms, and to relate the bedforms to the sediment transport process. The paper is organized in five sections. The first section describes the equipment deployed during this period at LEO-15 along with relevant calibration and processing information. The second section covers the evolution of ripple geometry in which observations of ripple wavelength and height are compared to previous empirical models. While most previous work has

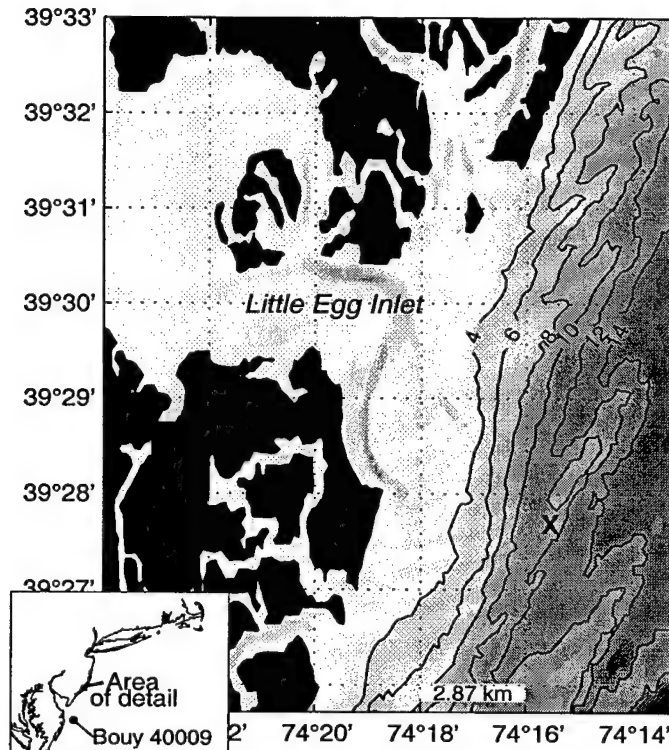


Figure 2-1 LEO-15 bathymetry. The tripod location on the southern end of Beach Haven ridge is marked by an X. Depth contours are labelled in meters, and the grid spacing is 2.87 km.

focused on ripple geometry, the sidescan sonar system is also able to resolve ripple migration rates; the third section examines ripple migration and associated sediment transport rates. The fourth section displays several individual images to illustrate mechanisms for ripple directional change, wavelength evolution and erosion. The final section places the observations in a climatological context by examining wave climatology data from NDBC [1995] buoy 44009.

## 2.2 Instrumentation and current meter data processing

Since sediment transport involves the interactions of bottom boundary layer hydrodynamics, suspended sediment dynamics and bedform morphology, it is necessary to observe all of these components. At LEO-15 a multi-instrument tripod was deployed that contained a vertical array of Benthic Acoustic Stress Sensor (BASS) [Williams *et al.* 1987] current meters and ElectroMagnetic Current Meters (EMCM) to measure water velocities, an Acoustic Backscattering System (ABS) to measure vertical profiles of suspended sediment concentration and local seafloor elevation, and a rotary sidescan (Sector Scanning) Sonar (SSS) to image bedform geometry and migration. It is

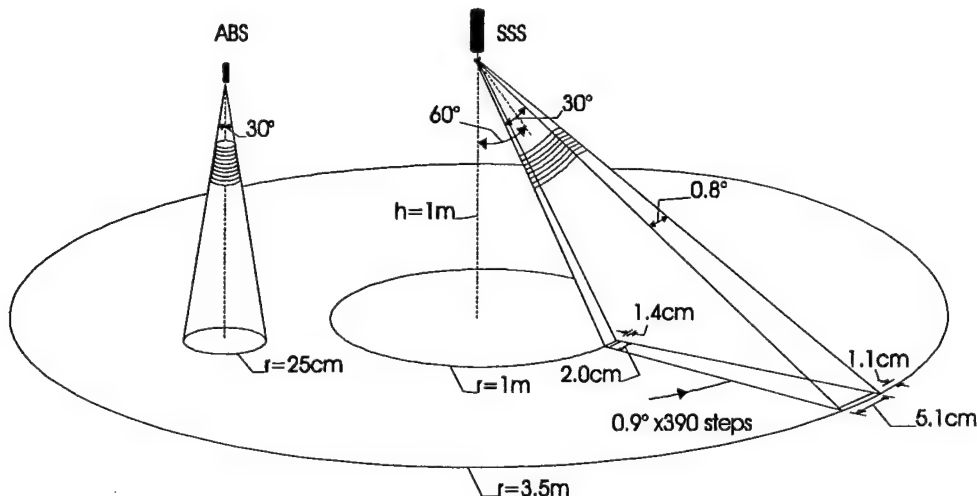


Figure 2-2 Rotary sidescan (sector scanning) sonar and acoustic backscattering system.

worth noting that SCUBA divers reported 1 to 2 foot visibility through much of the deployment, thus it is unlikely that photographic systems would have produced adequate bedform images. Biofouling of these systems became a serious problem by the end of the deployment. Thus after yearday 260 analysis is stopped. The acoustic SSS bedform measurements were generally more robust to biofouling than the EMCM and BASS current meter measurements.

### 2.2.1 Sector scanning sonar

The sector scanning sonar images a seafloor area of approximately  $35 \text{ m}^2$  by projecting a beam of sound with  $0.8^\circ$  beamwidth in azimuth by  $30^\circ$  high in elevation on a center axis aimed  $60^\circ$  above vertical as shown in figure 2-2. Since the inner edge of the main beam is at an angle of  $45^\circ$  to the vertical, there is a region of 100 cm radius in the center that is not imaged.

The beam is rotated around through  $351^\circ$  in  $390 \times 0.9^\circ$  steps. The range resolution of the instrument is 1 cm by sampling the envelope of the returned signal at 75 kHz. Combined with the  $0.8^\circ$  azimuth beamwidth, this gives resolution cells ranging from  $1.4 \times 2.0 \text{ cm}$  at 100 cm from the center of the image to  $1.1 \times 5.1 \text{ cm}$  at the maximum range of 350 cm. Photographic systems are generally able to achieve a higher resolution, at the expense of sampling a smaller area. The system operates at a frequency of 2.25 MHz. Roughness features that are much larger than the acoustic wavelength of 0.66 mm scatter in the geometric regime. Since the bedform features of interest at LEO-15 have typical wavelengths of 10 to 100 cm the images can be interpreted simply by considering areas of high acoustic backscattered intensity (light areas in the image) as surfaces facing towards the sonar transducer head, and areas of low acoustic intensity as surfaces facing

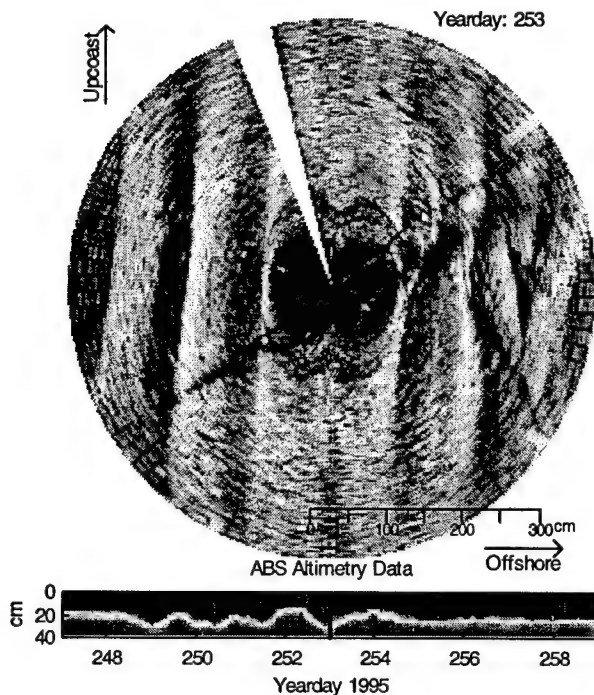


Figure 2-3 Sector scanning sonar image (above) and 12 day time series of ABS vertical profiler data (below). The sector scanner image shows some of the largest ripples observed, with wavelengths of 1m, and the ABS shows changes in seafloor elevation as the ripples migrate past the acoustic beam. Light areas in both image represent high acoustic returns. In this image the SSS was located directly over a ripple crest, while the ABS is located over a trough.

away from the sonar head. This is clearly visible in the image (figure 2-3) of 100 cm wavelength ripples taken on yearday 253, 1995. The acoustic shadows from the tripod legs are also noticeable in this image.

This system was originally designed by Simrad/Mesotech for use in imaging the insides of pipes and was adapted for coastal seafloor imaging applications with a cable to shore by *Hay and Wilson [1994]*. It was modified for autonomous use on the continental shelf by adding a PC 104 controller and a 2 Gbyte hard disk data storage system which allows sampling a new image every 30 minutes for a 6 week deployment such as this one conducted at LEO-15. [*Irish et al. 1997*]

### **2.2.2 Acoustic Backscattering system**

The tripod contained both Acoustic Backscattering (ABS) and Optical Backscattering Systems (OBS) to measure suspended sediment concentrations. The OBS system, with its maximum scattering response to sediments of radius  $a \sim 1 \mu\text{m}$  and  $a^{-1}$  geometric scattering fall off in intensity per unit sediment volume for larger sediment sizes, is unsuitable for detecting sand in the presence

of small quantities of finer sediments (figure 2-4). Bottom samples reveal finer sediment in the trough adjacent to Beach Haven ridge which can be advected over the ridge by mean currents. While this suspended mud has great impact on visibility and optical backscattered (OBS) intensity it does not influence sand ripple dynamics. Therefore, OBS measurements are not used in this paper. The median grain diameters ( $D_{50}$ ) measured at LEO-15 are typically 1.1 to 1.6  $\phi$  ( $D_{50} \sim 465$  to 330  $\mu\text{m}$ ) with standard deviations of  $\pm 0.5$  to  $\pm 1.0 \phi$  (2  $\phi = 250 \mu\text{m}$  to 0.1  $\phi = 933 \mu\text{m}$ ). Larger broken shell fragments or entire shells that generally do not comprise a significant percentage of the total mass, but can occasionally skew the size statistics, were not included in the grain size analysis [Craghan 1995].

The 2.5 MHz ABS system is located 110 cm above the seafloor within the imaged area of the sector scanning sonar. It has a vertical resolution of 1 cm and a beamwidth of 30° as defined by the half power points (-3dB). The instrument sampled for 4 minutes every half hour at a rate of 2 Hz. The acoustic intensity ( $I$ ) measured by this system is calibrated to give a measure of suspended sand concentration ( $C$ ). This can then be multiplied by the velocity measurements to estimate suspended sediment transport rates. The return from the seafloor also gives an estimate of the local elevation. A series of ripples of 10 to 15 cm height migrating past the ABS beam are shown in figure 2-2.

The ABS is calibrated in a tank with known concentrations of sediment from LEO-15 with a procedure similar to that described in *Lynch et al. [1994]*. Generally a single frequency acoustic system cannot measure concentration independently of sediment size since the Raleigh scattering dependence on grain size ( $I/C \propto a^3$  for  $ka \ll 1$ ) is stronger than the linear dependence on concentration. However the median grain size ( $\sim 400 \mu\text{m}$ ) from bottom samples at LEO-15 is near the scattering maximum at  $ka=1$  where  $k$  is the acoustic wavenumber (figure 2-4). In this region the scattering is roughly independent of grain size, which allows the use of a single frequency concentration estimate. An estimate of the error in concentration due to uncertainty in grain size can be obtained by noting that for sediment sizes within one standard deviation of the median (light shaded region in figure 2-4) there is a maximum fall off in intensity of 50%. Thus if the median grain size of suspended sediment is within one standard deviation of the median grain size of the bottom sediment the acoustic concentration estimates of suspended sand should be accurate to within approximately a factor of two.

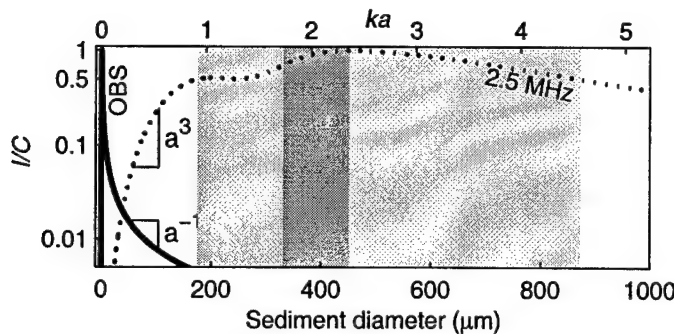


Figure 2-4 Acoustical and optical scattering intensities per unit sediment volume as a function of sediment diameter ( $D$ ) on the bottom axis and  $ka$  on the top axis. Intensities are normalized to have a maximum of unity. The acoustic results are generated using the expressions given by *Sheng and Hay [1988]*. The range of sediment diameters for which acoustic scattering intensity is within 50% of its maximum value is lightly shaded. This is approximately equal to the median grain size  $\pm 1$  std. The darker shaded region indicates the range of median grain diameters typically found at LEO-15.

### 2.2.3 Current meters and current meter data processing

Two types of current meters were used to measure water velocities on the tripod deployed at LEO-15. A Marsh-McBirney EMCM sensor was located 500 cm above the seafloor, and a vertical array of BASS sensors were located at 44, 80, 166, and 250 cm above the seafloor. Both systems had a burst sampling rate of 4Hz. The BASS sampled every hour with a burst length of 15 minutes while the EMCM sampled every 30 minutes for 8 minutes coherently with the ABS system. Since the BASS used a longer burst, the lowest BASS sensor is used to calculate burst-averaged quantities. Burst averaged root mean squared (rms) wave velocities ( $u_{w,rms}$ ) are calculated from the vector wave velocities by:

$$u_{w,rms} = \sqrt{\overline{|\vec{u}_w(t)|^2}}. \quad (\text{EQ 2.1})$$

The overbar is used to denote burst averaged quantities throughout the paper, and the wave velocity is calculated from the two horizontal velocity axes ( $\vec{u}$ )

$$\hat{\vec{u}}_w = \vec{u} - \hat{\vec{u}}_c \quad (\text{EQ 2.2})$$

where the vector mean current velocity ( $\hat{\vec{u}}_c$ ) with an alongshore component ( $v_c$ ) and an across-shore component ( $u_c$ ) is defined as:

$$\hat{\vec{u}}_c = \bar{\vec{u}} \quad (\text{EQ 2.3})$$

The vector wave velocity is rotated into a coordinate system that is aligned with the dominant wave direction and the dominant component of instantaneous wave velocity is defined as  $u_w$ . The dominant wave direction is calculated by rotating the 2-axis coordinate system until the variance is maximized along one axis. The dominant wave direction does not vary more than 30 degrees from directly onshore. Wave period ( $T=2\pi/\omega$ ) is calculated from the energy weighted mean frequency ( $\omega$ ) from the spectrum ( $u_{w,i}^2$ ) of wave velocities by [Madsen *et al.*, 1988]:

$$\omega = \frac{\sum \omega_i u_{w,i}^2}{\sum u_{w,i}^2} \quad (\text{EQ 2.4})$$

Since wave orbital diameter ( $d_o$ ) is an important factor for ripple geometry it is calculated directly from the wave velocity record by first integrating  $u_w$  to get an Eulerian particle trajectory:

$$x_w(t) = \int_0^t u_w(t') dt' \quad (\text{EQ 2.5})$$

This displacement time series ( $x_w(t)$ ) is then high-pass filtered using a filter with a 22 s cutoff to keep only wave velocities and remove infragravity motions. The significant orbital diameter ( $d_{o,1/3}$ ), which is equivalent to the orbital diameter based on significant wave height is then calculated by

$$d_{o,1/3} = 4\sqrt{\bar{x}_w^2} \quad (\text{EQ 2.6})$$

The rms orbital diameter ( $d_{o,\text{rms}}$ , i.e.  $d_o$  based on the rms wave height) can also be calculated by  $d_{o,1/3}=1.42d_{o,\text{rms}}$  [Longuet- Higgins 1952].

The results of these calculations for  $u_{w,\text{rms}}, T, d_{o,1/3}$ , and  $\hat{u}_c$  on data from the lowest BASS sensor are shown in figure 2-5. While the rms wave velocity reached peaks of 20 cm/s during the periods near day 241 and near day 253, the wave period became much greater (up to 16 s) during the latter period, and thus the orbital diameter is also much larger (up to 2 m) during the latter period. Mean currents in the alongshore direction, with peaks of up to 20 cm/s, are stronger than the weaker tidal currents in the across-shore direction with peaks of 5 to 8 cm/s. The peak alongshore currents are sometimes correlated with peaks in wave velocities, for instance, near day 243 and 240. However, at other times, for instance near day 256 and 259, there is a substantial phase lag since the waves are generated by storms located far offshore.

One of the important parameters in sediment transport that can be estimated from the current meter records is the bottom stress. The total bottom stress can be divided into a form drag component and

a skin friction component, where the skin friction is primarily responsible for sediment motion. When the bottom stress due to waves is much greater than that due to current the wave skin friction stress can be estimated by:

$$\tau_w^{sf} = \frac{1}{2} \rho f_{2.5} u_{w,m}^2 \quad (\text{EQ 2.7})$$

Here  $\rho$  is the water density, and the wave friction factor ( $f_{2.5}$ ) is that developed by *Swart* [1974] with the grain roughness defined by 2.5 times the median grain diameter ( $D_{50}$ ). The wave velocity used in eqn. 2.7 is defined by ( $u_{w,m} = \sqrt{2}u_{w,rms}$ ). Using this definition of wave velocity is equivalent to calculating wave velocity based on the rms wave height ( $H_{rms}$ ). An alternate representation of the wave velocity is  $u_{w,1/3} = 1.42\sqrt{2}u_{w,rms}$ . This calculation is consistent with using the significant wave height ( $H_{1/3}$ ) which is also consistent with the calculation of  $d_{o,1/3}$ . For the purpose of determining initiation of sediment motion and predicting sediment transport the skin friction bottom stress is often non-dimensionalized by taking the ratio of the stress to the immersed weight per unit area; i.e. the Shields parameter.

$$\theta_w^{sf} = \frac{\tau_w^{sf}}{\rho(s-1)gD_{50}} \quad (\text{EQ 2.8})$$

where  $g$  is gravity, and  $s=\rho_s/\rho$  is the ratio of sediment grain density to water density.

The component of skin friction bottom stress due to mean currents ( $\tau_c^{sf}$ ) was calculated in two different ways. The first method used was the *Grant, Glenn and Madsen* [1979,1983] (GGM) non-linear wave current interaction bottom boundary layer model as described by *Madsen and Wikramanayake* [1991]. The second method was a constant drag coefficient approach as described by *Sternberg* [1972]:

$$\theta_c^{sf} = \frac{C_d |\hat{u}_{c100}|^2}{(s-1)gD_{50}} \quad (\text{EQ 2.9})$$

where  $\hat{u}_{c100}$  is the current velocity one meter above the seafloor found from interpolating a log velocity profile fit to the BASS vertical array of current measurements, and  $C_d=0.003$ . This method was chosen since *Amos et al.* [1988] found it gave better separation of wave vs. current dominated ripple types. The constant drag coefficient gives peak current stress estimates that are about twice that of the GGM method, while the mean ratio of the two estimates is close to one. However, both methods show that the current stress is much weaker than the wave stress (figure 2-5) with the exception of the beginning of the deployment (before yearday 239) and a period near

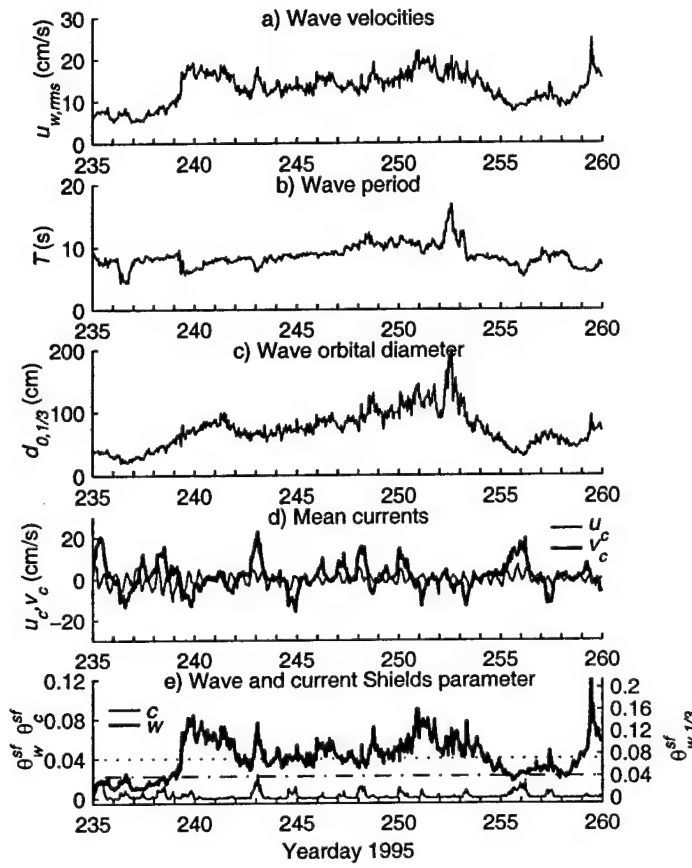


Figure 2-5 Current meter time series: a) Wave velocities, b) Wave period c) Wave orbital diameters, and d) Mean currents calculated from the BASS sensor 44 cm above the seafloor. e) Wave and current (constant drag coefficient) skin friction Shields parameter based on  $H_{rms}$  (left y-axis) and based on  $H_{1/3}$  (right y-axis). The critical Shields parameter for initiation of motion of  $\theta_{crit}^{sf} = 0.04$  is also shown as a dotted and dash-dotted line for each case.

yearday 256. Based on the constant drag coefficient approach the maximum value of  $\tau_c^{sf}/\tau_w^{sf}$  during periods of active ripple evolution (i.e. after yearday 239) is 0.6. This value occurred near day 256. The mean value over the entire period from day 235 to 260 of this ratio is 0.09.

Although the combined wave and current Shields parameter can be calculated from the vector sum of the wave and current stress, for the purposes of predicting initiation of motion, it is often sufficient to consider only the wave stress since the addition of current represents a negligible difference. The primary exceptions to this occurs near day 255 to 256, and at the beginning of the deployment.

## 2.3 Ripple Geometry

### 2.3.1 Temporal evolution of ripple characteristics and type

Features of the evolution of ripple patterns are best displayed by examining sequences of images directly. Computer animated movies of the hourly images provide a detailed view of these processes.<sup>1</sup> Representative images of the different stages of ripple evolution are shown in figure 2-7. Active ripple pattern changes and evolution is seen to occur throughout the period from day 238 to beyond day 260, despite the fact that  $\theta_w^{sf}$ , based on  $H_{rms}$ , often dips below the critical Shields parameter of  $\theta_{crit}^{sf} = 0.04$  (figure 2-5). This critical Shields parameter for the initiation of motion was calculated from the modified Shields curve [Madsen and Grant, 1976] for sand with  $D_{50}=400\text{ }\mu\text{m}$ , and is consistent with the value for combined flows used by Amos *et al.* [1988] for a slightly smaller sand size ( $D_{50}\sim 200\mu\text{m}$ ). If the Shields parameter is based instead on  $H_{1/3}$  the Shields parameter is consistently above the critical Shields parameter during the period when ripples are actively evolving. This makes physical sense because the calculations based on  $H_{rms}$  de-emphasize the contribution of the larger waves in a burst which do move sediment.

The deployment begins with *relic ripples* (Image 1), most likely left over from a strong “North Easter” storm that occurred one week prior to the deployment. The ripples have similar wavelength to actively evolving ripples on day 252 (Image 9), but the crests of the relic ripples were more rounded. By day 239.2 (Image 2)  $\theta_{w,1/3}^{sf}$  has exceeded  $\theta_{crit}^{sf}$  and wave ripples have begun to form. These short crested *3-d wave ripples* are similar to the variable bifurcated ripples and chaotic ripples described by Boyd *et al.* [1988]. They occur primarily as a transitional stage at the beginning of a storm event. During day 239 these *3-d wave ripples* become more organized into long crested *2-d wave ripples* (Image 3). This is the predominant ripple pattern seen at LEO-15 during this deployment. These are vortex ripples, as they have sharp crests that shed vortices regularly as seen by clouds of sediment in the ABS burst data.

From day 240 to day 242 the wave direction changes through  $30^\circ$  from a slightly down coast direction to straight onshore (figure 2-8). The ripples adapt to this change in wave direction by changing direction (Images 4,6) with a transitional stage consisting of *sinuous 3-d ripples* (Image 5). This sinuous pattern allows the ripple to change direction without sections migrating unreasonably long distances. By image 6 the sinuous kinks in image 5 have reconnected in the new direction. The crests are nearly straight and aligned with the directly onshore wave direction.

---

1. see <http://www.oal.whoi.edu/leo> [Traykovski 1996] for mpeg animations of ripple image data.

While these *sinuous 3-d ripples* occupy a similar transitional role as the variable bifurcated ripples described by *Boyd et al.* [1988] they are generally better organized into regular patterns, with more sinuous continuous crests, and fewer crest bifurcations. *Lee Young and Sleath* [1990] presented a model for serpentine (*sinuous*) ripples based on the interaction of waves and mean currents based on an oscillating tray in a flume experiment. Here a similar ripple pattern is generated by the changing wave direction. However, the fundamental physics of vorticity being swept along the ripple crest, presented by *Lee Young and Sleath* [1990], may be quite similar in both mechanisms of serpentine ripple formation. A simple physical model for the wavelength of the along-crest oscillations generated as the ripple change direction is shown in figure 2-6. From the intersection of the two ripple patterns the along-crest wave length  $p$  can be found to be

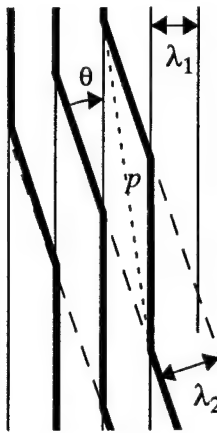


Figure 2-6 Along crest variation length scale schematic. The dashed solid lines are the steady-state ripple patterns generated by waves before a directional shift through an angle  $\theta$ . The thin solid lines are the steady state ripple pattern after the directional change. The thick lines are the transitional state (as seen in image 5) with along crest oscillations of wavelength  $p$ .

$$p = \sqrt{\frac{\lambda_1^2 + \lambda_2^2 + 2\lambda_1\lambda_2\cos(\theta)}{\sin^2\theta}} \quad (\text{EQ 2.10})$$

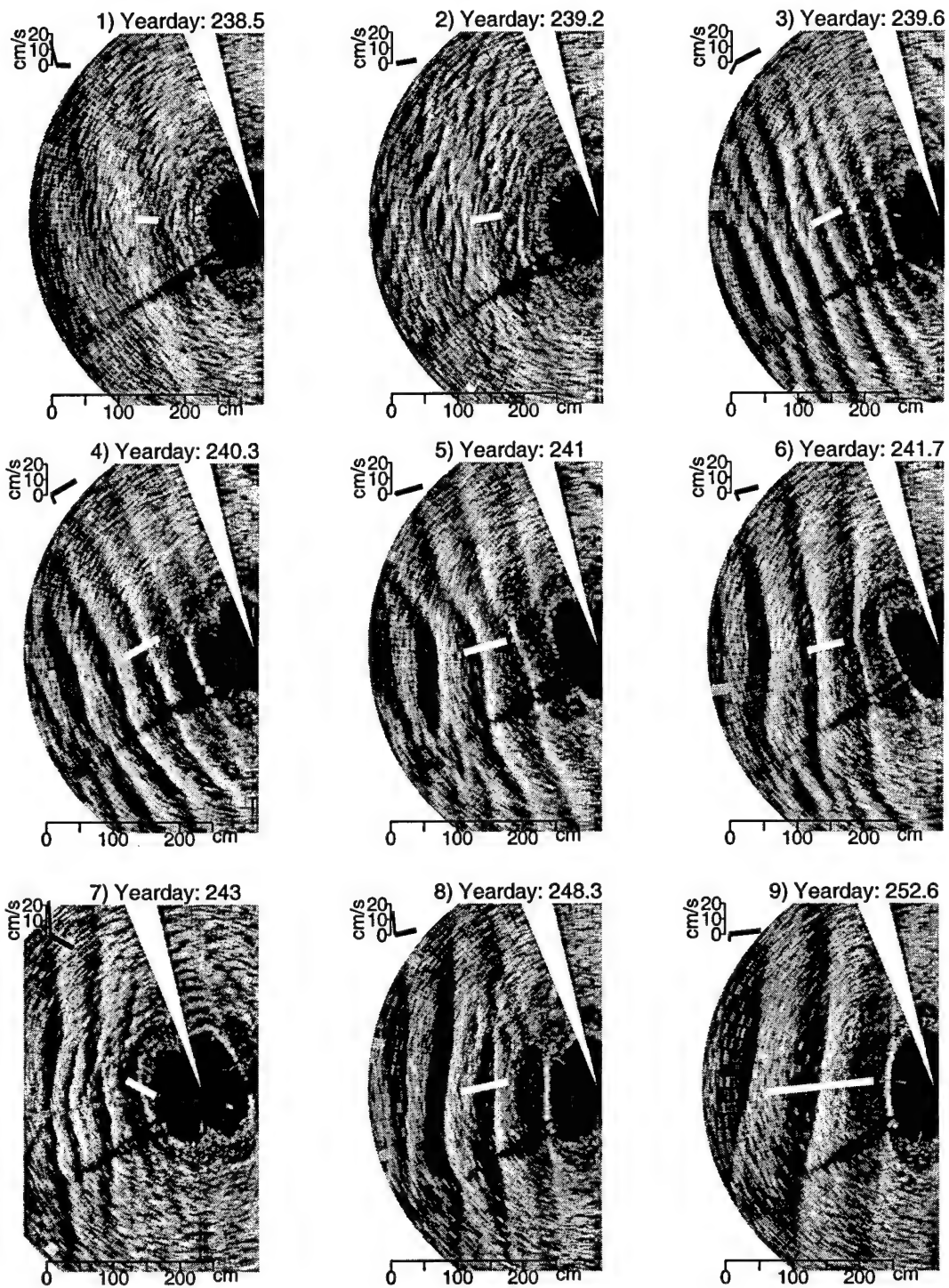
For example, during the period yearday 240.3 to 241.7 (Image 4 through 6) the ripples turned through  $30^\circ$  while changing wavelength from  $\lambda_1 = 50$  cm to  $\lambda_2 = 70$  cm. Eqn. 2.10 predicts an along crest oscillation wavelength of  $p=232$  cm while the measured value from image 5 is 220 cm.

On day 243 the largest alongshore currents of the deployment are present and small current ripples are visible in the troughs of the wave ripples (Image 7, particularly near the missing sector of the image). Due to the sector scanner geometry these ripples are only imaged when the acoustic beam points perpendicular to their crests. Presumably these current ripples are also present in the troughs of all the wave ripples. *Amos et al.* [1988] presented a classification of wave vs. current ripple

domination in terms of  $\theta_w^{sf}$ , and  $\theta_c^{sf}$ . In this case the values of  $\theta_w^{sf} = 0.08$  and  $\theta_c^{sf} = 0.02$  place these ripples in the wave ripple with superimposed, subordinate current ripples category of Amos *et al.* [1988], which is consistent with our observations. For most of our deployment  $\theta_c^{sf}$  is below 0.01 which according to Amos *et al.* [1988], is the region of wave dominated ripples, as is consistent with our observations.

The period from day 244 to day 253 is marked by an increase in wave orbital diameter up to a maximum of 200 cm on day 253. The 2-d *wave ripples* increase in wavelength, up to a maximum of 100 cm (image 9) in response to this forcing. On day 254 the waves have turned to a slightly down coast direction again, and have decreased orbital diameter to about 80 cm. With this evolution of the wave forcing, instead of forming *sinuous 3-d ripples* as in image 5 and turning to match the new wave direction, each of the large ripples begins to split along their crests into two ripples with half the wavelength (double the wavenumber) of the original ripples. These half wavelength ripples are parallel to the original crests (image 10). This can be best seen by examining the left most crest in image 10. In between the crests of the split ripple a set of subordinate diagonal cross ripples that matches the new wave direction has begun to form. The primary difference in the evolution of wave forcing, and thus ripple pattern, between the period near day 241 (image 5) and the period near day 254 (image 10) is that in the first case the waves changed direction without substantially changing orbital diameter, while in the second the waves also changed orbital diameter as they changed direction.

The transitional pattern shown in image 10 only lasts for several hours because by day 255.4 (image 11) the alongshore current speed becomes similar to the r.m.s. wave velocities. This has the effect of disorganizing the nearly 2-d wave orbital ripples into a more isotropic 3-d pattern. By yearday 256 the current has become substantially stronger than the r.m.s. wave velocities and has almost completely eroded the wave orbital scale ripples. The poorly organized bedforms in image 12 may be current ripples, but this image does not clearly show the current formed ripples that were visible in image 7. Presumably this period of ripple erosion is a period of large alongshore transport since the current is strong enough to flatten the 2-d wave ripples. In terms of relative wave vs. current stress on yearday 256  $\theta_c^{sf} = 0.015$  and  $\theta_w^{sf} = 0.025$ . At this value of the wave Shields parameter the current Shields parameter must exceed 0.04 for current ripples to dominate according to Amos *et al.* [1988]. This disorganized bedform pattern does not last long as the waves begin to form new 3-d *wave ripples* on day 257 (image 13), which eventually organize into 2-d *wave ripples* as previously.



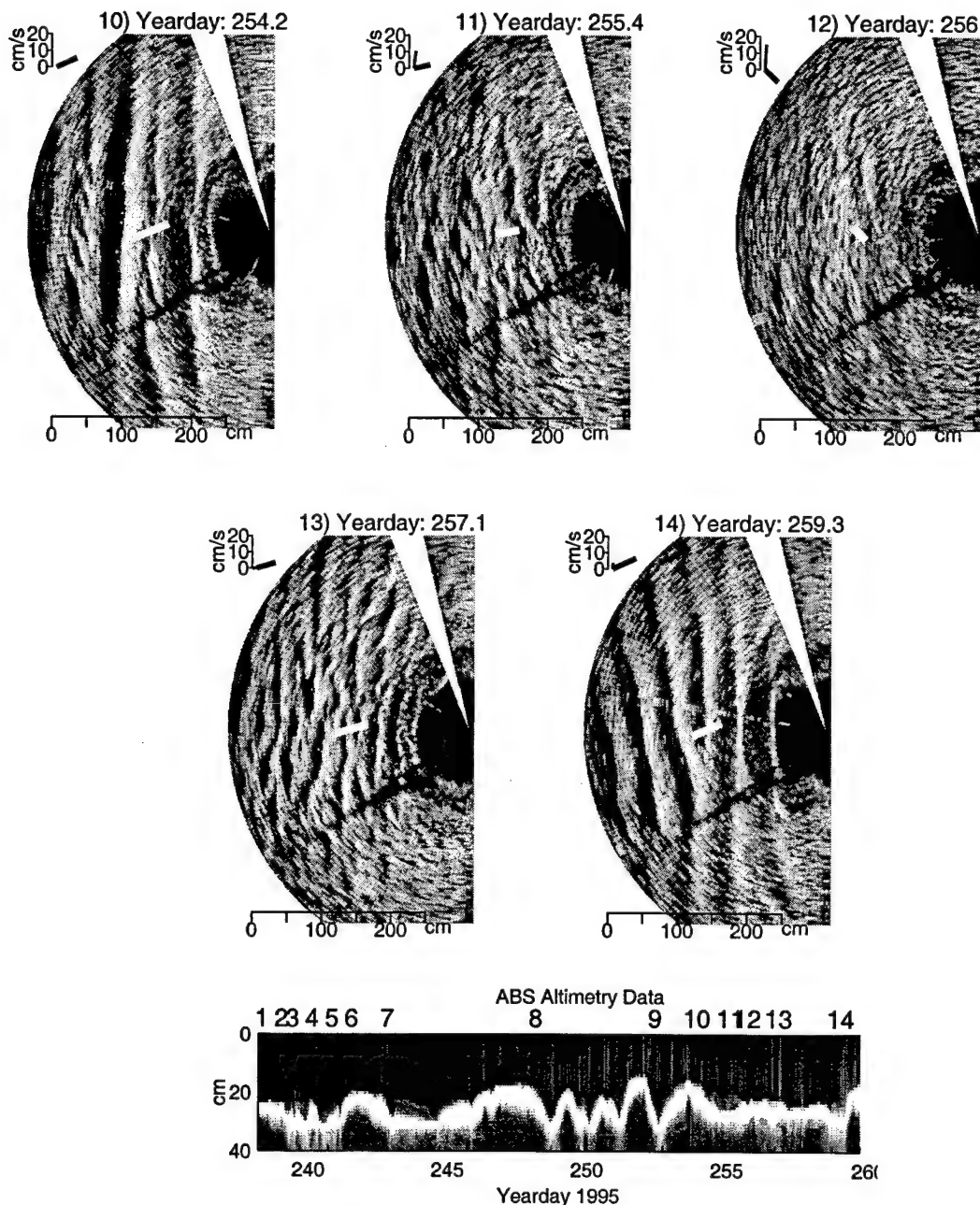


**Figure 2-7** Representative sector scanning sonar images. The thick white line near the center of each image represents the wave orbital diameter scaled by 3/4, and is aligned in the wave direction. The small plot below the upper left of each image displays the relative wave r.m.s. velocity (thick line) and current velocity (thin line).

### **2.3.2 Temporal evolution of ripple direction and wavelength**

From the rotary sidescan image data it is possible to measure time series of the geometric characteristics of the ripples such as wavelength and direction. A ripple direction estimate is found by manually locating end coordinates of a line normal to the ripple crests starting from the center of the image. The coordinate system is aligned such that a direction of 90° indicates a ripple with its crest running parallel to the average coastline orientation of 36°T. The projected distance along this line between several pairs of adjacent ripple crests is then used to estimate the ripple wavelength. If *3-d wave ripples* are present the wavelength is defined by the maximum separation between two adjacent crests. Enough pairs of points are chosen so that the standard deviation of the estimate is below 2 cm. In this procedure the first crest picked for a given image is the same as in the previous image so an estimate of ripple migration displacement between images can be found. Since the ripples only move a few centimeters per hour, as seen in the ABS altimetry record (figure 2-7), there are no difficulties identifying the same ripple in consecutive images. When a ripple crest leaves the image a new crest near the origin is tracked.

A high degree of correlation between ripple wavelength and scaled significant wave orbital diameter ( $0.75d_{o,1/3}$ ) is generally evident in the time series shown in figure 2-8. This indicates that the wave length of these ripples does scale with wave orbital diameter. During periods when *3-d wave ripples* are present the scaling factor appears to be smaller than 0.75.

Hysteresis effects (i.e. *relic ripples*) are visible at certain times during the deployment as indicated in figure 2-8. Most notably, at the beginning of the deployment 100 cm wavelength ripples were clearly visible in the sonar image from a storm which had occurred one week prior to the deployment. Near yeardays 242, and 253 delays of about one day are visible in ripples reacting to decreasing wave orbital diameter, before a step-like transition to the *2-d wave ripple* state occurs. Step-like transitions are also noted during the onset of storms between *3-d wave ripples* and *2-d wave ripples*. However, once 2-d ripples have formed the ripples are able to gradually adjust wavelength to match the increasing orbital diameter. This is somewhat consistent with the observation of *Boyd et al. [1988]* who noted “Storm arrival is accompanied by abrupt bed reorganization. In contrast as the storm moves away, a gradual step-like transition occurs through a characteristic sequence of reorganization and decay types.” Here the abrupt reorganization is the change from *3-d* to *2-d wave ripples*, and *Boyd's* step-like transitions at the end of a storm are similar to the step-like transition from periods of hysteresis to the next ripple type.

The temporal evolution of ripple direction (figure 2-8) also generally follows the dominant wave direction. Similar hysteresis effects to those seen in the wavelength time series are visible in the ripple direction time series. During the period from yearday 239 to 240 the ripple direction changes very closely match the wave directional changes. The largest discrepancy between ripple direction and wave direction occurs during the periods from yearday 235 to 238 and 253 to 256. During the first period the ripples are *relic ripples* and are not in equilibrium with the hydrodynamic conditions. During the latter period large ( $\lambda=1$  m) ripples are first being eroded by waves with a shorter orbital diameter, and then by large currents. The ripple pattern during this period is characterized by large 2-d wave ripples matching the original direction and the subordinate wave ripples matching the new wave direction as described in section 2.1 (Image 10).

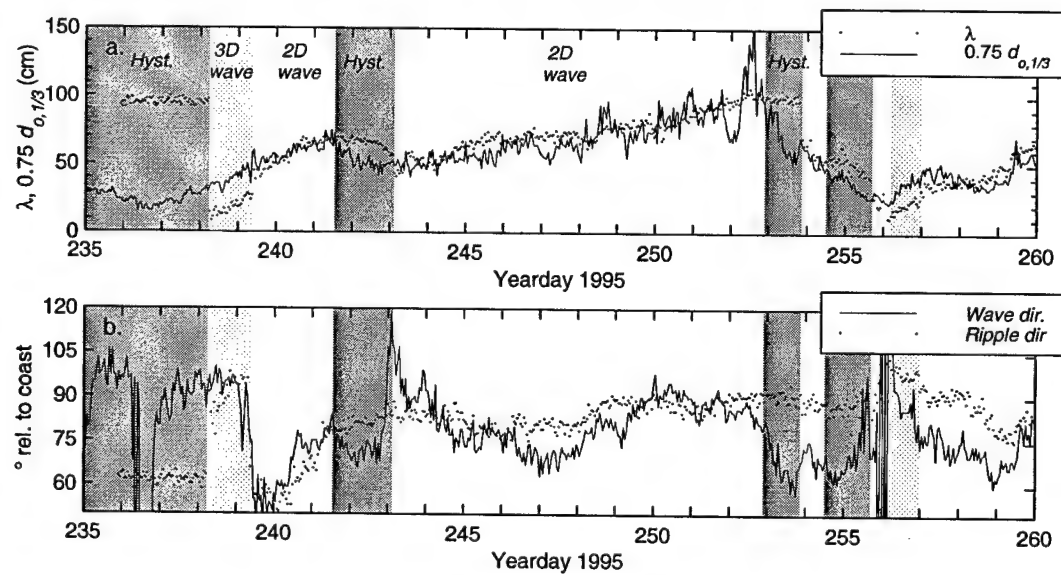


Figure 2-8 Temporal Evolution of Ripple features. a) Ripple wavelength ( $\lambda$ ) and scaled significant wave orbital diameter ( $0.75d_{0,1/3}$ ). Wave ripple type (2-d wave, 3-d wave), and periods of hysteresis (Hyst.) or *relic ripples* are indicated by the shaded regions b) Ripple direction and dominant wave direction.

### 2.3.3 Empirical models for ripple wavelength

Several authors have suggested linear relations between orbital diameter and ripple wavelength with similar scaling factors for wave ripples in a range of conditions. *Clifton and Dingler* [1984] summarized several data sets from both laboratory and field studies and suggested that ripple wavelength scales linearly with orbital diameter until wave orbital diameter / grain size ( $d/D$ ) reaches a value of 2000. In the range of  $2000 < d/D < 5000$  the ripples go through a transitional

stage, which they called suborbital ripples. For values of  $d/D > 5000$  ripple wavelength scales directly with grain size and *Clifton* [1984] suggested a scaling of  $\lambda = 400D$  to  $600D$ . *Wiberg and Harris* [1994] found a best fit with a scaling of  $\lambda = 535D$ .

For the scaling parameter relating  $\lambda$  to  $d_{0,1/3}$  *Inman* [1957] suggested a value of one. *Komar* [1974] suggested a value of 0.8 as a better fit to the data. Based only on flume data *Miller and Komar* [1980a] found a value of 0.65. *Miller and Komar* [1980b] also justified the use of  $d_0$  based on  $H_{1/3}$ , since they found that using  $H_{1/3}$ , as opposed to  $H_{rms}$ , gave better agreement to the relationship  $\lambda = 0.65d_0$  between field studies with irregular waves and laboratory studies with regular waves.

*Wiberg and Harris* [1994] classify ripple type based on the ratio of ripple height ( $\eta$ ) to wave boundary layer thickness ( $\delta_w$ ). Since  $\delta_w$  is roughly proportional to  $d_0$ , the classification ratio used is  $d_0/\eta$ . Limits of  $d_0/\eta = 20$  and  $d_0/\eta = 100$  are used to define the transitions from orbital to suborbital and suborbital to anorbital scale ripples. Classifying our data set based on observed  $\eta$  and  $d_{0,1/3}$  results in all the ripples being classified as orbital scale ripples (see section 2.3.6 for a discussion of observed ripple heights). For orbital scale ripples the predicted ratios of  $\eta_{orb}/\lambda_{orb} = .17$  and  $\lambda_{orb}/d_0 = .62$  are both constant and thus  $\eta_{orb}/d_0 = 0.1$  is also constant. Therefore  $d_0/\eta_{orb}$  cannot be used to predict a transition to suborbital or anorbital ripples. *Wiberg and Harris* [1994] resolved this problem by using the ratio of orbital diameter to anorbital ripple height ( $d_0/\eta_{ano}$ ) to define the transition. An empirical relationship was found to relate anorbital steepness to the ratio  $d/\eta_{ano}$ :

$$\frac{\eta_{ano}}{\lambda} = \exp \left[ -0.095 \left( \ln \frac{d}{\eta_{ano}} \right)^2 + 0.442 \ln \left( \frac{d}{\eta_{ano}} \right) - 2.28 \right] \quad (\text{EQ 2.11})$$

Since  $\lambda_{ano} = 535D$  and  $d_0/\eta_{ano} = 20$  and  $d_0/\eta_{ano} = 100$  define the transitions, eqn. 2.11 can be used to find the transitional points of  $d_0/D = 1754$  for orbital to suborbital and  $d_0/D = 5587$  for suborbital to anorbital. These values are fairly close to *Clifton and Dingler's* [1984] transitions at  $d/D = 2000$  and 5000.

To examine where our data falls in the context of this type of model, the ripple wavelength ( $\lambda$ ) normalized by measured median grain diameter ( $D_{50} = 400\mu\text{m}$ ) is plotted against significant wave orbital diameter normalized by median grain diameter ( $d_{0,1/3}/D_{50}$ ) in figure 2-9a.

The data points during periods of hysteresis are clustered along horizontal bands of constant ripple wavelength at  $\lambda/D_{50} = 1700$  and 2600. The hysteresis point located in the upper left corner of figure 9 are also characterized by  $\theta_w^{sf} < \theta_{crit}^{sf}$  as defined in section 1.3. The remaining data points fall

into two clusters depending on ripple type. The *2-d wave ripple* data points are well fit by a linear model of  $\lambda=0.76d_{0,1/3}$ , and have a correlation coefficient of  $R^2=0.86$ . The *3-d wave ripple* data points are also well fit by a linear model with a different slope of  $\lambda=0.38d_{0,1/3}$ , and have a correlation coefficient of  $R^2=0.80$ . A slightly better fit to the *3-d wave ripple* data points can be achieved if a linear model with an offset is used:  $\lambda=0.46d_{0,1/3}-5.0$ . While negative wavelengths are impossible, it is not implausible that the curves do not need to be extrapolated to pass though the  $\lambda=0, d_0=0$  point due to thresholding effects.

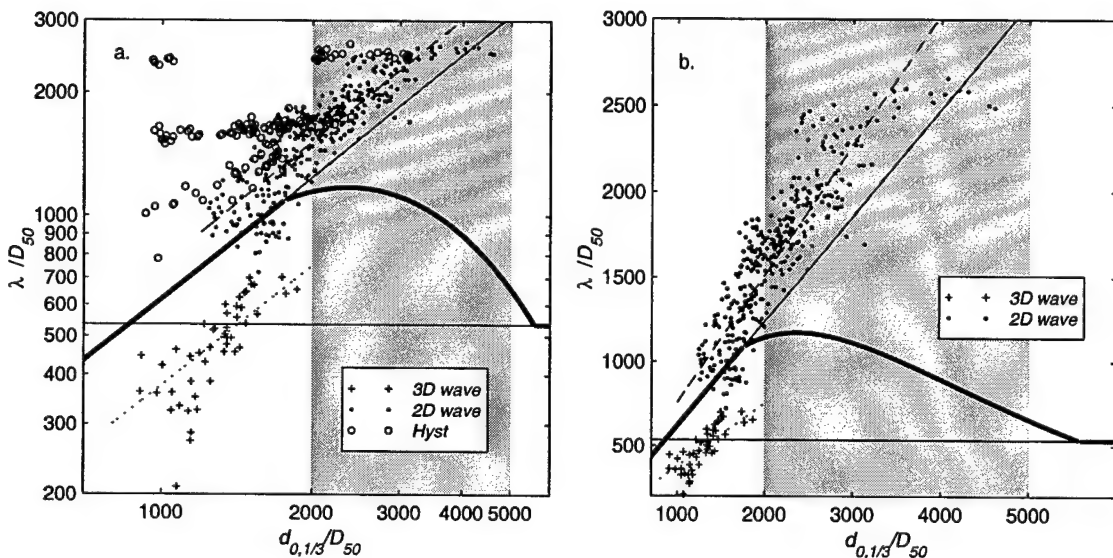


Figure 2-9 a) Ripple wavelength ( $\lambda$ ) as a function of wave orbital diameter ( $d_{0,1/3}$ ), with both quantities scaled by measured median grain size  $D_{50}=400\mu\text{m}$ . Points represented by open circles are during times of hysteresis as determined from the time series b) Same as a, but hysteresis points not displayed and linear axis scaling. Points represented by crosses are *3-d wave ripples* with a scaling of  $\lambda=0.38d_{0,1/3}$  shown as a dotted line. Points plotted as dots are *2-d wave ripples* with a best fit line of  $\lambda=0.76d_{0,1/3}$  shown as dashed line. The thick solid line is the *Wiberg and Harris [1994]* empirical model with the orbital scaling of  $\lambda=.62d_0$  and an orbital scaling of  $\lambda=535D$  continued beyond the transitional (gray shaded) region as thin lines.

### 2.3.4 Temporal evolution in $\lambda/D$ , $d_o/D$ space.

As an alternate method of examining effects such as hysteresis one can examine the temporal evolution of the relation between  $\lambda/D_{50}$  and  $d_{0,1/3}/D_{50}$ . The evolution of ripple wavelength over one storm event from day 238.2 to day 243.15 is shown in figure 2-10. The ripples start as *3-d wave ripple* and increase wavelength in response to increasing wave orbital diameter roughly along the *3-d wave ripple* orbital relation line of  $\lambda = 0.38d_{0,1/3}$ . By day 239.3 the ripples become organized into *2-d wave ripple* and increase wave length along the *2-d wave ripple* orbital relation

line of  $\lambda = 0.76d_{0,1/3}$ . By yearday 241.5 the ripples are close to their maximum wavelength, for this particular storm, of approximately 68 cm ( $\lambda/D_{50}=1700$ ) due to waves with  $d_{0,1/3}=88$  cm ( $d_{0,1/3}/D_{50}=2200$ ). During the next day a hysteresis period occurs as the wave orbital excursion diminishes and the ripples maintain a constant wavelength. By yearday 243 a strong current event combined with waves with  $d_{0,1/3}/D_{50}=1700$  reduce the ripple wavelength by a factor of 2/3. While the ripples do not exactly follow this type of 3 step triangular trajectory in  $\lambda/D_{50}$ ,  $d_{0,1/3}/D_{50}$  space for every storm, it is a fairly typical sequence of events. The hysteresis (*relic ripples*), in particular, where the ripples maintain constant wavelength for some period while the wave orbital diameters are diminishing is seen at the end of all the storm events in this data set.

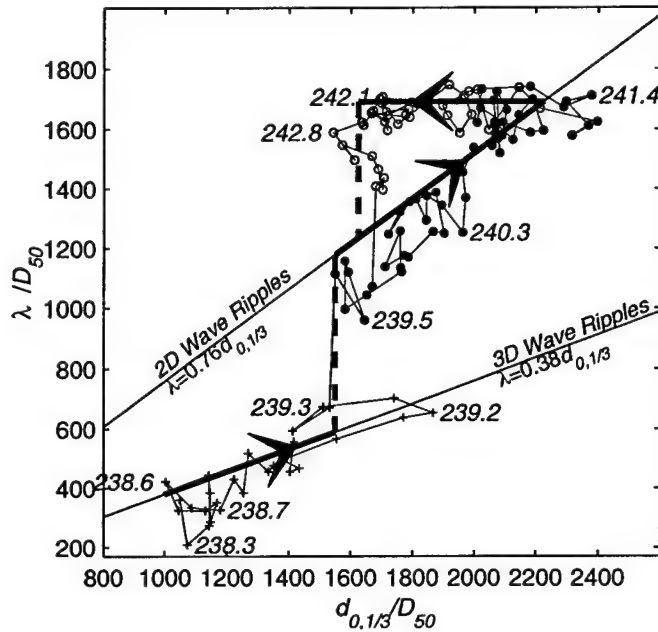


Figure 2-10 Temporal evolution of ripple wavelength as a function of wave orbital diameter with both quantities normalized by median grain size ( $D_{50}=400\mu\text{m}$ ). The dots, crosses, and open circles represent actual data points connected by lines in the order of occurrence. The different symbols indicate ripple type as in figure 2-9. The time of selected points is shown. The thick arrows are a conceptual model for the temporal evolution. The diagonal upward thick black lines are the trajectories along the orbital ripple scaling relations of  $\lambda=0.38d_{0,1/3}$  and  $\lambda=0.76d_{0,1/3}$ . The horizontal line with an arrow pointed to the left is the hysteresis path.

### 2.3.5 Maximum ripple wavelength and transition to suborbital scaling

The data show a maximum ripple wavelength of about 100 cm ( $\lambda/D_{50}=2500$ ) despite the fact that the wave orbital diameter exceeds 130 cm ( $d_{0,1/3}/D_{50}=3250$ ) for 10 hours near yearday 253 (figure 2-8). There are more than ten hourly sampled ripple wavelength points in figure 6 at the maximum wavelength of 100 cm due to hysteresis effects. With the waves only exceeding the linear relation

for a short time it is not clear that this is indeed the maximum wavelength ripple that will form at LEO-15 and that the data points with  $\lambda=100$  cm for  $d_{0,1/3}$  greater than 130 cm are in the transitional region. If the waves were to get significantly longer than 130 cm for extended periods of time and ripple wavelengths remained at 100 cm, this would be a clear indication of a transitional stage with a maximum wavelength of 100 cm. The probability of seeing such large waves at LEO-15 for an extended time is discussed in section 6.

According to the models, the transition to suborbital scaling should occur just after the orbital diameter exceeds the diameter which would cause the maximum predicted ripple wavelength. If we are indeed seeing a transition to suborbital ripples near an orbital diameter of  $d_s=130$  cm ( $d_{0,1/3}/D_{50}=3250$ ), scaling the data by the median grain size of  $D_{50}=400$   $\mu\text{m}$  would indicate a transition in the data at about  $d_{0,1/3}/D_{50}=3250$  as opposed to  $d_{0,1/3}/D_{50}=2000$  as predicted by the *Wiberg and Harris* [1994] model (figure 2-9a). For a  $D_{50}=400$   $\mu\text{m}$  grain size scaling, the maximum wavelength predicted by the model is 47 cm ( $\lambda/D_{50}=1175$ ). This is much smaller than the maximum observed wavelength of 100 cm. However if a larger grain size scaling of  $D_{85}=800$   $\mu\text{m}$  is used, the transition does occur near  $d/D=2000$  and the data, including the maximum observed wavelength of 1m, is well fit by the *Wiberg and Harris* [1994] model as seen in figure 2-9b. This larger grain size of  $D_{85}=800$   $\mu\text{m}$  is approximately one standard deviation above the median grain size. For our data, scaling the model by the observed median grain size  $D_{50}=400$   $\mu\text{m}$  results in an incorrect prediction of a transition to suborbital ripples as well as an under-prediction of the maximum ripple wavelength.

The largest wave orbital scale ripples that were included in the references to field data sets that *Wiberg and Harris* [1994] used to construct their empirical model were the  $\lambda=100$  cm ripples observed in  $D_{50}=500$   $\mu\text{m}$  sand by *Inman* [1957] which are also somewhat larger than the maximum predicted ripple wavelength of  $\lambda=68$  cm for  $D_{50}=500$   $\mu\text{m}$  sand.

*Miller and Komar* [1980] suggested an empirical formula for maximum ripple wave length based largely on laboratory studies of:

$$\lambda = 0.0027D^{1.68}. \quad (\text{EQ 2.12})$$

With  $D_{50}=400$   $\mu\text{m}$  sediment this formula predicts a maximum ripple wavelength of 65 cm which is also considerably smaller than the 100 cm wavelengths observed at LEO-15.

While *Clifton and Dingler* [1984] and *Wiberg and Harris* [1994] suggest that an orbital ripple wavelength scales with grain size alone, and thus the transitions can be defined in terms of  $d_o/D$ ,

other authors describe anorbital ripple wavelength as functions related to bottom stress. Based on field data by *Inman* [1957], *Dingler* [1974] and *Miller and Komar* [1980], *Nielsen* [1981] found  $\lambda/A$  as a function of mobility number ( $\psi$ ):

$$\frac{\lambda}{A} = \exp\left(\frac{693 - 0.37 \ln^8 \psi}{1000 + 0.75 \ln^7 \psi}\right) \quad (\text{EQ 2.13})$$

Mobility number is a measure of bottom stress forces ( $\propto$  velocity<sup>2</sup>) acting to move the sediment relative to gravitational forces stabilizing the sediment and is defined as:

$$\psi = \frac{(A\omega)^2}{(s-1)gD} \quad (\text{EQ 2.14})$$

where  $A=d_o/2$  is the wave orbital excursion amplitude,  $\omega$  is the wave frequency,  $g$  is gravity, and  $s=\rho_s/\rho_w$  is the ratio of sediment density to water density. With this type of model the transition to anorbital type of scaling depends not only on grain size and wave orbital diameter, but also on wave period. At longer wave periods the transition to anorbital scale ripples occurs at larger orbital diameters as shown in figure 2-11. This also allows the model to predict larger maximum wavelength ripples at longer wave periods before a transition occurs.

Our data show a maximum wavelength of 100 cm near yearday 253. During this storm the wave periods reached 14-16 seconds. With wave periods of 16 seconds *Nielsen's* [1981] model predicts a maximum wavelength of 96 cm ( $\lambda/D_{50}=2400$ ), consistent with our observed maximum wavelength of 100 cm.

Although the *Grant and Madsen* [1982] model does not explicitly contain a linear relation between orbital diameter and ripple wavelength the equations for  $\eta/A$  and  $\eta/\lambda$  define a nearly linear relation in their "equilibrium range". The slight variations from a linear relation are seen by the varying position, as a function of wave period, of the dashed lines in figure 2-11. This model defines a transition to a regime of lower ripple steepness at a "break-off" skin friction wave Shields parameter value. Since the Shields parameter is dependent on both wave period and velocity this model, like the *Nielsen* [1981] model, defines a transition that does not only depend on  $d_o/D$ . The *Grant and Madsen* [1982] model predicts the maximum observed ripple wavelength with a wave period of approximately 13 seconds.

The physical justification for the larger maximum wavelength ripples at longer wave periods could be that with the lower velocities associated with longer period waves with the same bottom orbital diameter as shorter period waves with higher velocities, the sediment transport is

dominated by bedload rather than suspended transport. Presumably the bedload mode is more conducive to orbital scale ripples, while fully suspended transport favors anorbital ripples or sheet flow conditions. Bedload forced formation of orbital scale ripples may also be related to the required scaling by a larger grain size to make the LEO-15 data agree with the empirical models that do not take wave period into account, since the larger grains are more likely to be transported as bedload rather than suspended load.

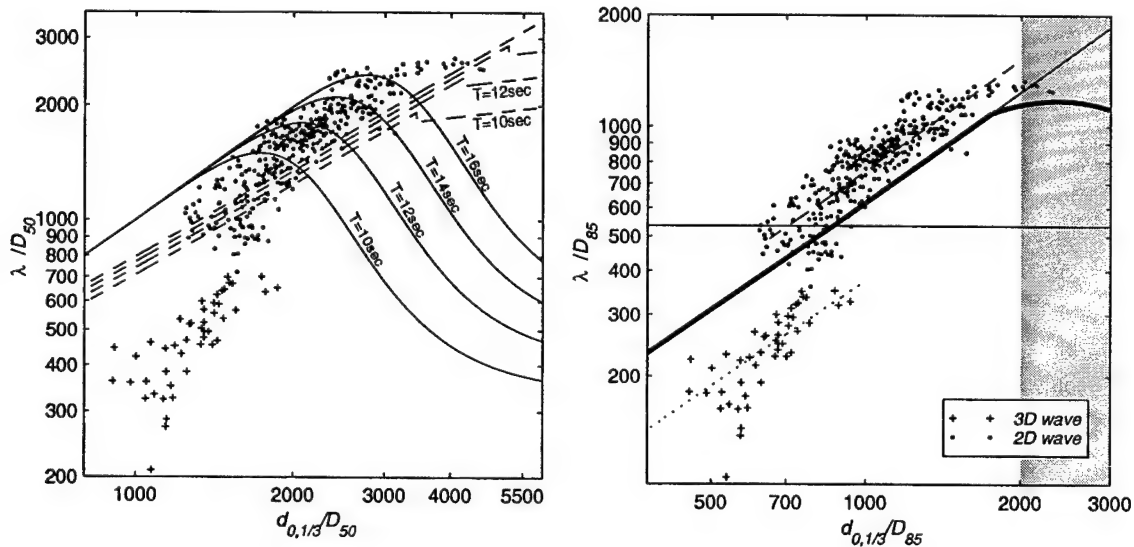


Figure 2-11 a) Ripple wave length as a function of significant wave orbital diameter with both quantities normalized by measured median grain size,  $D_{50}=400\mu\text{m}$ . The *Nielsen* [1981] model is shown as the solid lines with wave periods varying from 10-16 seconds. The *Grant and Madsen* [1982] model, also with periods from 10-16 seconds, is shown as the dashed lines. b) The *Wiberg and Harris* [1994] model normalized by  $D_{85}=800\mu\text{m}$  is shown as the thick solid line. The best fits to the 3-d and 2-d wave ripple data are shown as the dotted and dashed line respectively.

### 2.3.6 Ripple Height

The second important parameter that is used to describe the geometry of nearly 2 dimensional wave ripples is ripple height ( $\eta$ ). The instruments deployed on the LEO-15 tripod allow two different methods of estimating the temporal evolution of ripple height.

The bottom return from the ABS data can be used to estimate the distance to the local seafloor from the sonar head (figure 2-2 and figure 2-3). As a ripple migrates past the beam a height can be determined from the difference between crest and trough elevation. This gives a discrete time series with each height estimate generated at the time between the passage of a crest and trough. The  $30^\circ$  beamwidth of the ABS gives a footprint of 50 cm as defined by the half power points.

This could produce an error of a few cm in estimating the depth of the trough with large ripples, and completely averages out the height variations associated with ripples of wavelength much less than 50 cm. Data from a second acoustic backscattering system with a very narrow beam (2 cm footprint) that was operational until yearday 243 gives a similar height estimate to the ABS system since most of the ripples observed at LEO-15 had wavelengths greater than 50 cm.

The second height estimate is generated from the intersection of the SSS beampattern with the seafloor. The first bottom return in the SSS data is generated when the lower edge of the beampattern, which is angled down at  $45^\circ$ , hits the bottom. This appears in the sector scanner images as the edge between the black region in the center of the image and the grey area where the sound beam is hitting the bottom (figure 2-3). The variations in distance of this edge from the center of the image are clearly visible as the beam rotates around to point at the ripple trough and then the ripple crest. This distance is represented by the line AB in figure 2-12. If the variations in the length of line AB as the sector scanner rotates around are multiplied by a factor of  $\cos(45^\circ)$ , a series of elevation estimates ( $h-\zeta$ ) can be generated around the  $r \sim 1$  m radius circle where the SSS beampattern intersects the bottom. Here  $\zeta$  is defined as the local surface elevation above the ripple trough. The standard deviation of the  $h-\zeta$  estimates is then multiplied by a factor of  $2\sqrt{2}$  to give an estimate of ripple height ( $\eta$ ). This is based on assuming a sinusoidal ripple profile, since for a sine wave the height is equal to  $2\sqrt{2}$  times the elevation standard deviation (for a triangular ripple profile assumption, the factor would be  $2\sqrt{3}$ ). However, assuming a sinusoidal profile gives reasonable agreement with the ABS estimate thus  $2\sqrt{2}$  is used.

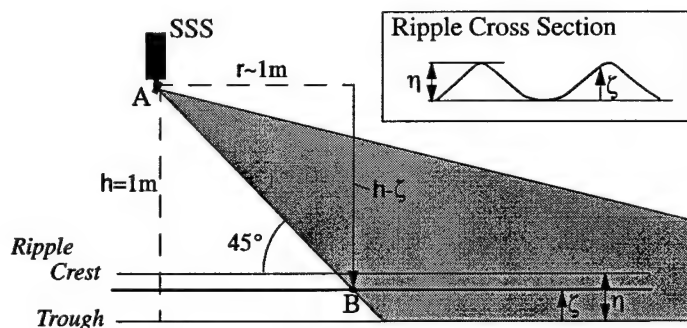


Figure 2-12 An estimate of ripple height can be calculated from each sector scan image by examining changes in the distance AB from the transducer head (A) to the point of intersection of the lower edge of the beam pattern with the ripple surface (B). The distance AB changes as the transducer rotates to aim the beam at different locations on the ripple surface.

While the SSS ripple height estimate generates hourly estimates of ripple height as opposed to the ABS estimate which depends on migration speed, the SSS estimate has an error depending on

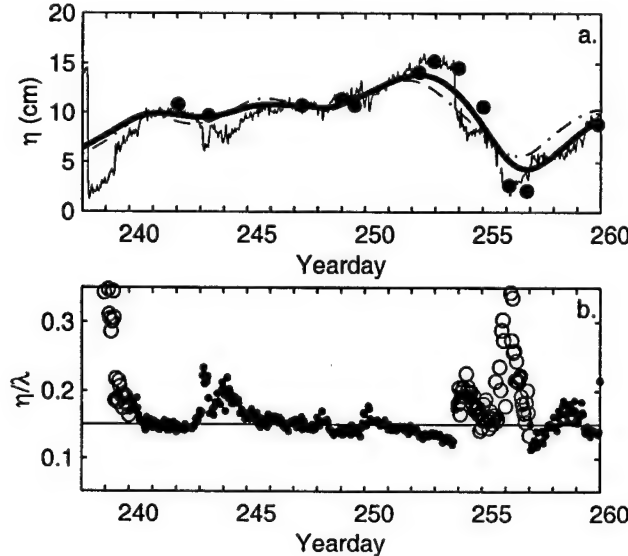


Figure 2-13 Evolution of ripple heights. a) Ripple heights (dots are the ABS altimeter estimates, dash-dot line is the SSS sidelobe estimate, and thick line is the average of the two estimates) and ripple wavelength scaled by 0.15 (thin solid line) as a function of time. b) Ripple steepness ( $\eta/\lambda$ ) as a function of time. The open circle points are not reliable as described in the text, and are not included in the calculation of the mean (thin line, at  $\eta/\lambda=0.15$ ).

whether the SSS is located over a ripple trough or crest. The SSS estimate is low-pass filtered with a smoothing filter that has a time scale of the longest ripple migration crest to crest time. The ABS estimates are interpolated with an interpolator that also has a similar time scale. The ABS and the SSS height estimates are averaged to give a single time series for calculation of ripple steepness as shown in figure 2-13.

The periods of high apparent steepness near year days 239 and 255 are probably not very significant since the ripple height estimate has the most error when the ripples are small and migration rates are low. Given the errors inherent in both methods of estimating ripple heights, the mean steepness of  $\eta/\lambda=0.15$  for the entire deployment is the most confident statement that can be made about ripple steepness. The periods of small ripples and high steepness denoted by open circle points in figure 2-13b were not included in this mean. This quantity agrees reasonably well with average steepness for wave orbital ripples of  $\eta/\lambda=0.17$  reported by *Wiberg and Harris [1994]*,  $\eta/\lambda=0.18$  reported by *Nielsen [1984]*, and  $\eta/\lambda=0.16$  reported by *Grant and Madsen [1982]*. Just as

a transition to an orbital ripple scaling was not evident in the wavelength data no evidence for a transition to a decreased steepness regime is evident in the steepness data.

## 2.4 Ripple Migration

Although the geometrical properties of wave ripples are important for their effect on the boundary layer hydrodynamics, and thus sediment transport, perhaps one of the important mechanisms for cross shore material transport is the migration of ripples.

Ripple migration displacement is found by tracking the coordinates of a particular ripple crest as discussed in section 2.1. Displacement is only measured in a direction normal to the ripple crests. Since the ripples are generally aligned with crests running nearly parallel to the coast, the direction of migration is referred to as simply on-offshore even though there may be some small alongshore component. The coordinate system used in this paper has the positive directions oriented offshore and up-coast.

The cumulative ripple migration displacement ( $X_m$ ) found by summing the hourly inter-image displacements from time zero (yearday 238) to the time indicated on the x-axis is shown in figure 2-14a. This figure also shows the rate of migration ( $v_m$ ) computed from the temporal derivative of the smoothed cumulative migration displacement. The direction of migration is seen to be consistently onshore with the only apparent exception occurring near yearday 240. This is a period during which the ripple direction is turning rapidly (figure 2-8b) and thus a particular section of ripple may be moving offshore as the ripple pattern evolves.

The total onshore migration of the ripples is 600 cm over a period of 25 days thus giving a average onshore migration rate of 24cm/day. Peak rates of 80 cm/day in the onshore direction are seen around yearday 250 when the ripples have the longest wavelengths observed throughout the deployment.

The ripple migration rate is seen to be greatest when the wave energy is highest (figure 2-14c) and does not appear to be related at all to either component of current velocity (figure 2-14d). In particular, ripple migration is in the across-shore direction (aligned with the waves) and currents in the across-shore direction are dominated by the weak (5 cm/s) semi-diurnal tides. This would indicate that current is not a forcing mechanism for ripple migration. In addition, purely linear monochromatic wave motion with no superimposed current would result in equal velocities in either direction and thus no transport. Wave non-linearity as waves enter shallow water results in

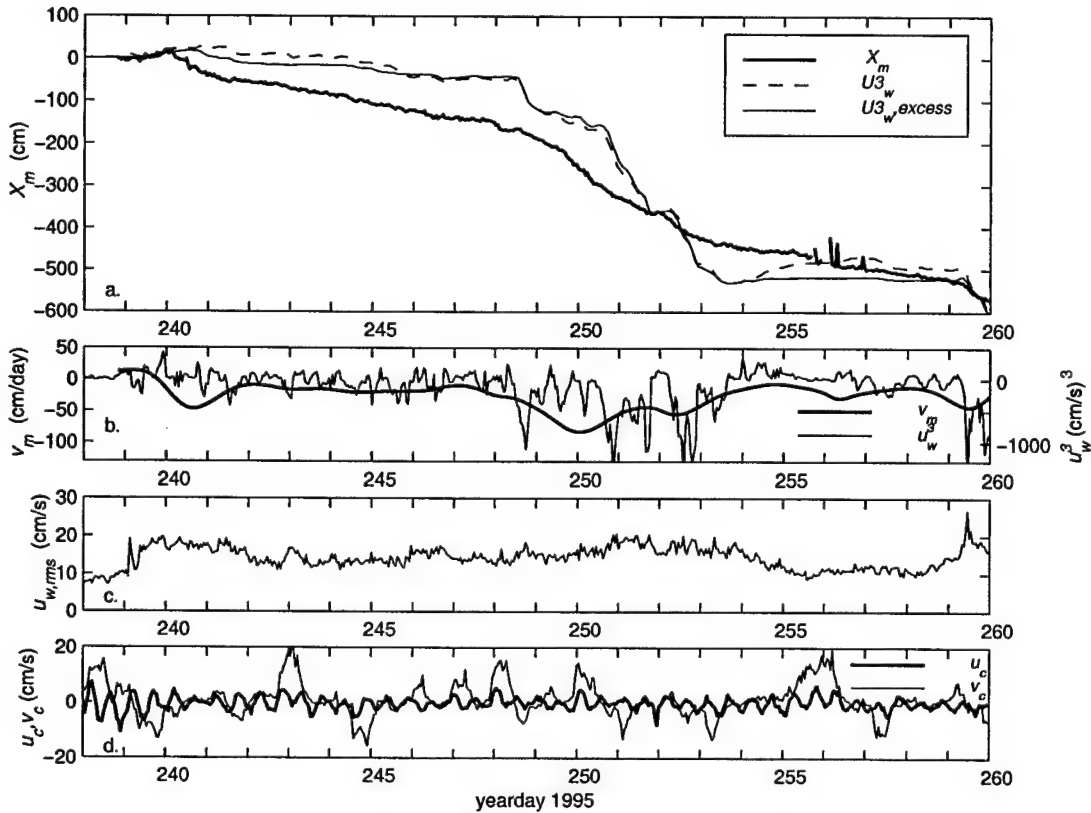


Figure 2-14 Ripple migration as related to wave and current parameters. a) Ripple crest displacement,  $X_m$  (thick line),  $U3_w$  (thin dashed line) and  $U3_{w,excess}$  (thin solid line) b) Ripple crest velocity  $v_m$  (thick line, left y-axis), and  $u_w^3$  (thin line, right y-axis.) c) rms wave velocity ( $U_{w,rms}$ ) d) Alongshore ( $v_c$ , thin line) and Cross-shore ( $u_c$ , thick line) current velocities from BASS burst averages 44 cm above the seafloor. The cross shore current is dominated by the semi-diurnal tide, is relatively weak, and thus transports little sediment compared to waves.

asymmetric velocity distributions about the mean velocity with larger onshore velocities for shorter periods and longer periods of weaker offshore velocities. This can clearly result in a net transport of sand, and thus possibly force ripple migration, particularly if there exists a threshold for sand movement that is exceeded more often by the onshore velocities.

To determine if wave non-linearity is a direct forcing mechanism for ripple migration, one could examine wave skewness ( $s$ ) calculated from the BASS sensor 44 cm above the bed.

$$s = \frac{\overline{u_w(t)^3}}{\overline{u_{w,rms}^3}} \quad (\text{EQ 2.15})$$

Skewness, however, weights large velocity waves equally to small velocity waves due to the  $u_{w,rms}^3$  in the denominator. Physically waves with larger velocities would be expected to mobilize

greater amounts of sand so a better forcing mechanism may be the burst averaged  $u_w^3$  shown in figure 2-14b.

$$\overline{u_w^3} = s u_{w, rms}^3 \quad (\text{EQ 2.16})$$

In the coordinate system with negative  $u$  directed onshore negative  $\overline{u_w^3}$  indicates larger onshore velocities. The  $\overline{u_w^3}$  record shows several negative peaks near yearday 250 and 259 consistent with a period of fast ripple migration. The  $\overline{u_w^3}$  time series shows a high degree of variability at the semi-diurnal tidal frequency, especially near periods of rapid migration such as near yearday 250. The tidal variability in  $\overline{u_w^3}$  is most likely forced by the tidal flows across the ridge as out going (positive) tidal currents can cause an increase in wave steepness which in turn increases (negative)  $\overline{u_w^3}$ . This is evident in figure 2-14b just after yearday 250. If tidal variability exists in the ripple migration velocity record, it is not seen since a substantial amount of smoothing is required in taking the derivative of the measured displacement record ( $X_m$ ) to get migration velocity ( $v_m$ ). The smoothing is required due to high frequency noise in  $X_m$ .

Since  $X_m$  is the actual measured ripple displacement, it is more appropriate to look at a forcing function that can be directly compared to  $X_m$ , such as the cumulative time integral of the wave forcing. In figure 2-14a the cumulative integral of  $\overline{u_w^3}$  is plotted with a single scaling constant to fit the ripple migration data.

$$U3_w(t) = \int_0^t \overline{u_w^3(t')} dt' \quad (\text{EQ 2.17})$$

While the general shape of  $U3_w$  time series matches the ripple displacement fairly well,  $U3_w$  would indicate greater migration during the most extreme event near yearday 250 and less migration during the other times<sup>1</sup>. A second similar function was also investigated.

$$U3_{w, excess}(t) = \int_0^t \overline{(u_{w, excess})^2 u_w} dt'$$

$$u_{w, excess} = \begin{cases} |u_w| - u_{crit} & |u_w| > u_{crit} \\ 0 & |u_w| < u_{crit} \end{cases} \quad (\text{EQ 2.18})$$

The critical velocity ( $u_{crit}$ ) for initiation of sediment motion of approximately 25 cm/s was found by using the methods discussed in section 2.2. This function should emphasize the larger waves more than  $U_w^3$ , since waves with velocities below  $u_{crit}$  are not included in the mean. However,

---

1. Capital variables are used to denote cumulative quantities.

both  $U3_w$  and  $U3_{w,excess}$  give fairly similar results. Both of these proposed forcing functions are attempting to relate ripple migration to an integrated wave statistic. This does not account for the possibility that larger ripples may require greater amounts of wave motion to force ripple migration at the same rate as smaller ripples. This concept will be discussed further in the next section.

#### **2.4.1 Sediment transport due to ripple migration and suspended sediment transport**

To further investigate a possible forcing mechanism for ripple migration, suspended sand transport itself can be examined. Since the observation system measures both water velocity and vertical profiles of sand concentration, instantaneous Eulerian transport rate calculations can be performed by multiplying these two quantities together assuming that sediment moves at the water velocity.

$$\hat{q}(z) = \hat{u}(z)C(z). \quad (\text{EQ 2.19})$$

The sand concentration profile is measured from 80 cm above the bed to a within a few centimeters of the bed, where the bottom return contaminates the acoustic backscattering measurement of suspended sediment.

Suspended sediment transport rates were calculated with both the mean current velocities ( $\hat{u}_c(z)$ ) and wave velocities ( $u_w$ ). The depth dependence of the steady current was calculated by fitting a log profile to the BASS current meter vertical array. It was found that the net sediment transport due to the mean currents was a factor of five less than the transport due to wave velocities<sup>1</sup>. The net suspended sediment transport due to the current is also mostly in the alongshore direction with only a small component in the across-shore direction. Since the wave velocity contribution to sediment transport is much larger than the current component, and the ripples migrate in the across-shore direction of the wave propagation only the wave component of transport is considered as a possible forcing function for ripple migration.

For  $u_w$  the velocity is assumed to be constant with depth over the lower 80 cm of the water column. Since most of the longer period waves at LEO-15 are shallow water waves, this should be valid outside of the thin wave boundary layer. By examining wave velocities along the BASS vertical array it was confirmed that wave velocities were relatively constant with depth over the lower portion of the array. The height of the wave boundary layer over large orbital scale ripples is not well defined for wave orbital scale ripples since wave boundary layer models predict a

---

1. This will be the topic of a future paper.

boundary layer thickness smaller than the ripple height. In fact, the *Wiberg and Harris* [1994] wave ripple model defines wave orbital ripples as having heights larger than the wave boundary layer. The boundary layer that does exist is probably a transient boundary layer that forms on the upstream face of ripple before the flow detaches at the ripple crest. The amount of suspended sediment transported by the wave velocities in a burst is calculated by:

$$m_{suspended,w}(z) = \sum_0^{T_b} C(z) u_w \Delta t. \quad (\text{EQ 2.20})$$

Here  $\Delta t$  is the temporal burst sampling interval of 0.5 seconds and  $T_b$  is the burst length of 240 seconds from the ABS sampling schedule. The units of  $m_b$  are grams/cm<sup>2</sup>, and  $m$  is related to the average sediment transport rate by

$$\bar{q} = \frac{1}{T_b} m \quad (\text{EQ 2.21})$$

Figure 2-15a shows the cumulative sum of depth-integrated burst-integrated wave induced transport

$$M_{suspended,w}(t) = \sum_0^t \sum_{z=0}^{z_{max}} m_{suspended,w}(z, t) \frac{\Delta T_b}{T_b} \quad (\text{EQ 2.22})$$

$$z = z_{min} - z_t$$

The units of  $M_{suspended,w}$  are grams/cm width. The time  $t$  is the time from the beginning of the deployment. The factor of  $(\Delta T_b/T_b)$  is the ratio of the burst length ( $T_b$ ) to the inter-burst time ( $\Delta T_b$ ) of 30 minutes. This accounts for the fact that burst sampling only occurs for a fraction of the total time and assumes stationary statistics for estimating the total transport, which may not be fully valid since the suspension process depends strongly on the tails of the wave velocity distribution. The depth variable  $z$  is defined as the distance from the instantaneous local bottom, and  $z_t$  is the distance from sonar transducer. The change of variables from  $z$  to  $z_t$  in eqn. 2.19 places the temporal averaging across depth bins into a coordinate system relative to the instantaneous local bottom elevation. The lower limit of depth integration  $z_{min}$  is set at 6 cm above the maximum bottom return to avoid calculating transport with range cells that are contaminated by the bottom return. The upper limit of integration  $z_{max}$  is set 80 cm above  $z_{min}$  since the wave induced transport is generally close to zero at this height.

As a first order estimate of the error in the suspended sediment transport calculation caused by integrating only to within 6 cm of the bottom, the calculations in eqn. 2.20 and eqn. 2.22 were repeated with the depth averaged sediment concentration in the bottom three centimeters (6-9cm above bottom) extrapolated down an additional 5cm. This had the effect of increasing  $M_{suspended,w}$

from 260 g/cm to 360 g/cm. While this is a substantial difference it is of the same order as the potential factor of two error from the ABS concentration estimate.

To examine the depth-dependence of this process the time integrated net depth dependent mass transport can be calculated by:

$$m_{d, \text{suspended}, w}(t, z) = \sum_0^t m_{\text{suspended}, w}(z, t) \frac{\Delta T_b}{T_b} \quad (\text{EQ 2.23})$$

This quantity is plotted for the time intervals yearday 235 to 245, 245 to 255, 255 to 260, and for the whole deployment in figure 2-15b. These three periods were chosen since there is offshore transport in the first, onshore in the second, and offshore again in the third.

By examining the thick line in figure 2-15b it is evident that for the entire deployment the transport is directed offshore above  $z=7\text{cm}$ , and onshore below  $z=5\text{cm}$ .

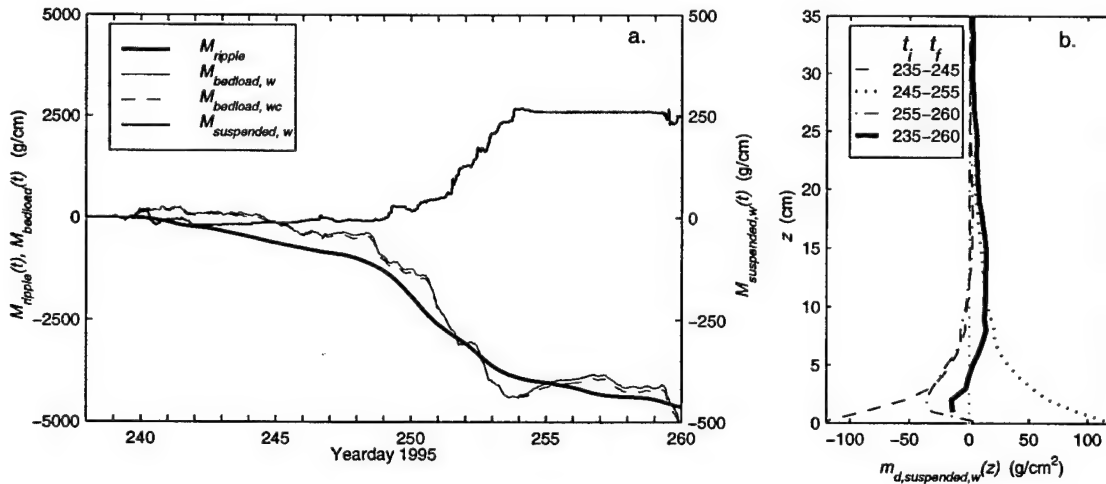


Figure 2-15 Suspended sand transport and Ripple sand transport. a) Temporal evolution of cumulative net depth integrated suspended transport ( $M_{\text{suspended},w}$ ). The scale for  $M_{\text{suspended},w}$  is on the right y-axis. Sand transport associated with ripples based on the assumption that ripples transport their entire volume of sand ( $M_{\text{ripple}}$ ). The scale for  $M_{\text{ripple}}$  is on the left y-axis. Bedload model forced with wave stresses as ( $M_{\text{bedload},w}$ , left y-axis) calculated by the instantaneous wave velocities ( $u_w(t)$ ) and forced with combined wave-current stresses ( $M_{\text{bedload},wc}$ , left y-axis) b) Depth dependent transport  $m_{c,\text{wave}}$  for periods yearday 235 to 245 (dashed line), 245 to 255 (dotted line), 255 to 260 (dash-dotted line), and 235 to 260 (thick line). Negative transports are onshore.

The positive y-direction in figure 2-15 is offshore, thus the total cumulative wave induced transport ( $M_{\text{suspended},w}$ ) over the entire deployment is directed offshore. During the period from

yearday 250 to 254 where onshore ripple migration displacement is greatest the wave induced suspended transport is also large, but in the offshore direction. Over the entire period yearday 238 to 260 the amount of suspended transport is a factor of 20 less than the transport associated with ripple migration ( $M_{ripple}$ ) as seen in figure 2-15a.

The total mass of sediment per unit cm width associated with the ripples that migrated past the SSS system at any time  $t$  can be estimated as:

$$M_{ripple}(t) = \int_0^t \rho_s(1-\varepsilon)\zeta V_m dt \quad (\text{EQ 2.24})$$

where  $\rho_s$  is the sediment density in g/cm<sup>3</sup>,  $\varepsilon$  is the porosity ( $\varepsilon=.35$ ) [Sleath 1984],  $\zeta$  is the instantaneous ripple elevation, and  $V_m$  is the rate of migration.  $M_{ripple}$  is plotted in figure 2-15a.

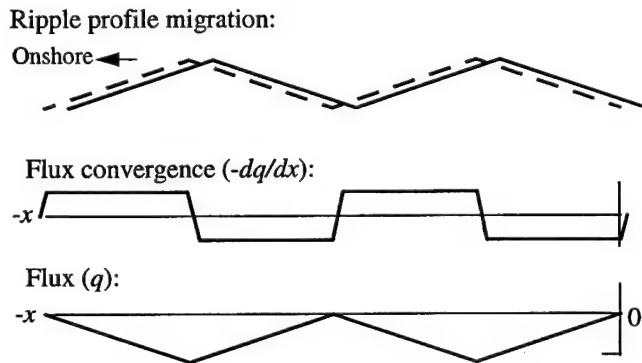


Figure 2-16 A simple conceptual model for relating bedload transport to ripple migration. The migration of the ripple profile over half a wave cycle is related to the temporally integrated flux convergence over the half wave cycle. The diagram is shown for the onshore half cycle of wave motion.

Equation 2.24 can be derived by examining the continuity equation for sediment mass (figure 2-16), [Engeleund and Fredsoe, 1982]:

$$\frac{\partial q}{\partial x} = \rho_s(1-\varepsilon)\frac{\partial}{\partial t}\zeta. \quad (\text{EQ 2.25})$$

If the bedforms are assumed to migrate with velocity  $V_m$  and maintain constant shape (i.e.  $\zeta = F(x - V_m t)$ ) then:

$$\rho_s(1-\varepsilon)\frac{\partial}{\partial t}\zeta = -\rho_s(1-\varepsilon)V_m\frac{\partial}{\partial x}\zeta, \quad (\text{EQ 2.26})$$

and thus

$$q = \rho_s(1 - \varepsilon)V_m\zeta + q_0. \quad (\text{EQ 2.27})$$

Here  $q_0$  is an arbitrary constant of integration which is set to zero based on the assumption that the ripples transport their entire volume of sand with them. This is not generally the case. In unidirectional flows bedforms can migrate the opposite direction to the net transport. For low shear stresses where most of transport occurs as bedload  $q_0$  is often assumed to be zero in unidirectional flows [Fredsoe and Diegaard, 1992]. If there is no exchange of sediment from one ripple to the next this is a valid assumption. For wave orbital scale ripples the transport is limited to a distance equal to or less than one ripple wavelength. While the ABS instrument is unable to resolve the thin layer of sediment transport with a few cm of the ripple surface, it is unlikely that sediment is transported from one ripple to the next in this thin layer. Reasons for this include the high velocity shear within the wave boundary layer and the generation of eddies in the lee of each ripple that limit the transport distance. Outside of this thin layer the ABS does not observe a sufficient amount of suspended sediment transport to make the constant of integration ( $q_0$ ) substantially different from zero. From qualitative laboratory observations it is evident that with wave orbital ripples most of the sand exchange from one face of a ripple to another occurs over the crest of the ripple and not the trough [Bagnold, 1946]. With these constraints the sand transport associated with the ripple migration should approximately equal the volume of sand contained in the ripples times the migration rate.

Unfortunately the ABS system is unable to observe the thin layer of bedload or near bottom suspended transport that is responsible for forcing the ripple migration, and the ripple transport is in the opposite direction and an order of magnitude larger than the wave induced sand transport 6 to 80 cm above the bottom that the ABS does observe. Thus it is hypothesized that bedload, or near bottom suspended transport that is not well observed by the ABS and current meter system is the dominant form of cross shelf transport for the medium to coarse grained sediments that occur on the ridge at LEO-15, and is the forcing mechanism for ripple migration.

#### 2.4.2 Bedload Modeling

Since bedload or near bottom suspended transport was not measured directly, to test the hypothesis that it is forcing ripple migration, one can compare the sediment transport associated with the migration of the ripples to sediment transport predicted by a bedload model. Dimensionless bedload flux ( $\Phi_B$ ) models typically take a form of:

$$\Phi_B = \frac{Q_B}{\rho_s D \sqrt{g D(s-1)}} = \begin{cases} C_B (|\theta_w^{sf}| - \theta_{crit})^{1.5} \frac{\theta_w^{sf}}{|\theta_w^{sf}|} & |\theta_w^{sf}| > \theta_{crit} \\ 0 & \theta_w^{sf} < \theta_{crit} \end{cases} \quad (\text{EQ 2.28})$$

where  $Q_B$  is the bedload flux in g/cm s,  $\theta_w^{sf}$  is the wave skin friction Shields parameter,  $\theta_{crit}$  is the critical Shields parameter ( $\theta_c=0.04$ ), and  $C_B$  is a constant of proportionality. The quantity  $|\theta_w^{sf}| - \theta_{crit}$  is the excess Shields parameter above the critical threshold. The well tested (for flat beds, and steady flow) *Meyer-Peter & Muller* [1948] formula suggests use of eqn. 2.28 with  $C_B=8$ . To extend this type of formula to spectral waves with non zero skewness *Nielsen* [1992] suggests using

$$\theta_w^{sf}(t) = \frac{1}{2} f_{2.5} \frac{\sqrt{2} u_{w, rms} u_w(t)}{g D(s-1)} \quad (\text{EQ 2.29})$$

to calculate an instantaneous Shields parameter. In eqn. 2.29  $f_{2.5}$  is calculated based on  $H_{rms}$  for a burst, and the wave period calculated by eqn. 2.4. A zero degree phase lag between stress and velocity is also assumed. Since  $u_w(t)$  are the instantaneous wave velocity samples within a burst eqn. 2.29 generates a time series of instantaneous Shields parameters within the wave cycle. From the time samples of instantaneous Shields parameter within the bursts the cumulative bedload transport is calculated as:

$$M_{bedload}(t) = \sum_0^t Q_B(t) \frac{\Delta T_b}{T_b} \Delta t. \quad (\text{EQ 2.30})$$

$M_{bedload}$  is compared to the sediment transport associated with ripple migration ( $M_{ripple}$ ) in figure 2-15a. In order to make the magnitude of  $M_{bedload}$  agree with  $M_{ripple}$  over the period yearday 238 to 260 a scaling factor of  $C_B=8*62$  was used instead of the 8 suggested in *Meyer-Peter & Muller* [1948] formula. While *Nielsen* [1992] recommended the use of  $\sqrt{2} u_{w, rms} u_w(t)$ , based on the rms wave height, for the velocity squared factor in eqn. 2.29 other possibilities exist. Table 2-1 shows the required scaling constants for the velocity squared factor based on the rms wave height, the significant wave height and the actual instantaneous wave velocity. The motivation for using the instantaneous wave velocities is from *Madsen* [1991] who suggested bedload responds virtually instantaneously to time varying velocities associated with waves. The fact that the scaling constants are substantially larger than 8 indicates that either scaling for this type of bedload formula needs to be substantially larger for the bedload transport associated with orbital scale

ripple migration, or that a significant portion of the transport is occurring as near bottom suspended load.

Wave Height Definition	Velocity squared factor	$C_B$
$H_{rms}$	$\sqrt{2} u_{w, rms} u_w(t)$	8*62
$H_{I/3}$	$1.42 \sqrt{2} u_{w, rms} u_w(t)$	8*21
Instantaneous	$u_w(t)$	8*10

Table 2-1 Various velocity squared factors and the associated bedload model scaling constants.

Another possibility for the difference in the magnitude of transport between the data and the model with  $C_B=8$  is that there is velocity enhancement as the flow passes over the crest of the ripple. This type of velocity enhancement is particularly important when the wave stresses are near the critical stress for initiation of motion. However, if sediment is in motion only near the crest there exists a trade-off in increased bedload transport due to the increased flow velocity and decreased bedload transport due to the spatial average over the ripple wavelength. If sediment is in motion over the entire face of the ripple the flow enhancement at the crest is balanced by flow speed reduction over the trough and the spatially averaged transport rate does not increase substantially.

*Nielsen [1992]* based on data from *Du Toit and Sleath [1981]* suggested a velocity enhancement factor of  $1/(1 - \pi\eta/\lambda)$  based on velocity measurements over orbital scale vortex ripples. Thus the enhanced Shields parameter is given by

$$\frac{\theta_w^{sf}}{(1 - \pi\eta/\lambda)^2} \quad (\text{EQ 2.31})$$

Using this Shields parameter and the original model scaling constant of  $C_B=8$  gives a  $M_{bedload}$  that agrees well with  $M_{ripple}$ . This calculation does not account for the reduction in bedload transport due to spatial averaging over a ripple wavelength and thus over estimates  $M_{bedload}$ . The use of a flow enhancement factor is also not universally agreed upon in the literature. *Wiberg and Harris [1994]*, based on measurements by *Ikeda [1991]*, suggested that a flow enhancement factor should only be used for anorbital ripples. In a recent paper *Li et al. [1997]* used this flow enhancement factor to predict initiation of bedload motion over a rippled bed.

Comparing figure 2-15a ( $M_{ripple}$  and  $M_{bedload}$ ) to figure 2-14a (Ripple migration  $X_m$  and  $U3_w$ ) one can see there is better agreement of the shape of the curves in figure 2-15a. This is due to the fact that while the shape of  $M_{bedload}$  and  $U3_w$  are similar, the ripple migration transports less sand

during periods of slow migration when the ripples are small, and more sand during periods of fast migration when the ripples are larger. This forces the slope of  $M_{ripple}$  to become steeper than the slope of  $X_m$  in the period around yearday 250 and flatter elsewhere. In general, the shape of curves  $M_{ripple}$  and  $M_{bedload}$  agree well, thus this type of bedload model with the appropriate velocity squared factor and scaling constant can be used as a predictive tool for sediment transport associated with ripple migration in conditions similar to those found at LEO-15 during this deployment.

To test the possible role of bedload caused by mean currents the bedload flux model calculations were also performed with the combined stress estimates generated using the *Grant, Glenn, Madsen [1979,1983]* model for the stress due to currents and eqn. 2.29 for the stress due to waves. In figure 2-15 it is shown that the model results for the combined case and for waves alone are virtually identical indicating that the contributions from mean currents is negligibly small.

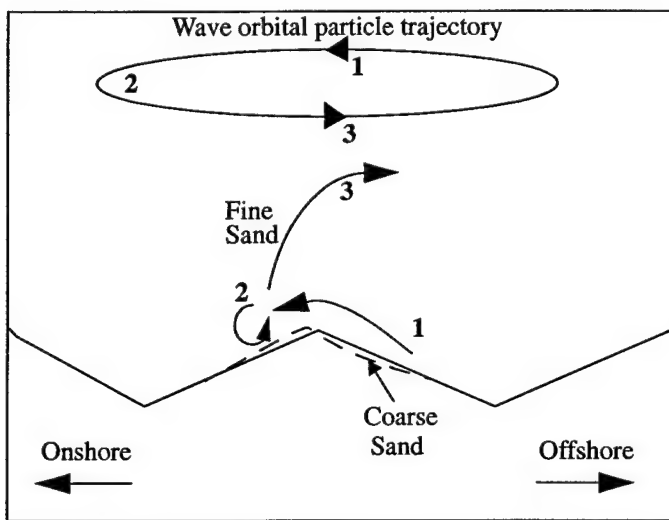


Figure 2-17 Vortex ejection and bedload forcing of ripple migration mechanism. The greatest velocities are in the onshore direction. This onshore portion of the wave cycle moves fine and coarse sand over the crest (1) where most of the coarse sand is deposited to force the ripple migration as seen by the dashed line. This is the dominant cross shore transport mechanism. However some of this sand (particularly the finer fractions) that passes over the crest is entrained into a vortex in the lee of the ripple (2). This vortex is ejected upward into the water column during the wave reversal and is transported offshore in the next half of the wave cycle as it decays and sand settles out (3). The grain size dependence of this process is described in *Bagnold [1946]*, and could account for the offshore suspended transport during periods of high wave velocity. While this process reverse every half wave cycle the stronger onshore velocities associated with non-linear waves allows the onshore phase to dominate.

The fact that the ripple migration is onshore and is forced by bedload and near-bed suspended transport, and that the suspended sand transport above 5 cm off the bottom is offshore during the period of largest waves can be interpreted in terms of a vortex ejection process as described by *Bagnold* [1946], *Inman and Bowen* [1963], *Nielsen* [1992] and others. Flow separation and vortex formation is occurring at LEO-15 as indicated by the sharp crested ripples (figure 2-2.) High frequency ABS images of plumes of suspended sediment rising to 60-80 cm above the bottom are also consistent with a vortex ejection process. One possible explanation of the observed phenomena is shown in figure 2-17.

The observations of ripple migration directed onshore with suspended transport directed offshore (presumably carrying the finer fractions) are consistent with *Craghan's* [1995] observations of grain size distributions across Beach Haven ridge where the coarsest sediments are found on the landward flank and become progressively finer over the crest. This consistency assumes the ripple migration is forced by bedload and carries coarser sediments and the suspended transport consists of finer fractions as consistent with a vortex ejection mechanism.

## 2.5 Wave ripple climatology for LEO-15

The data analyzed in this paper was taken over six week period during an active hurricane season. Wave climatology can be used to examine whether the observed wave orbital ripples are the dominant type of bedform at LEO-15 in other seasons or over a longer time scale. Data of this type is readily available from the *National Data Buoy Center's* [1995] wave buoy 44009 located in 30m depth water at the mouth of the Delaware Bay approximately 100 km south of LEO-15. Figure 2-18 displays the frequency of occurrence distribution vs. wave period and significant wave height taken from 56788 hourly records during a 9 year period from 10/1984 to 12/1993. Also plotted on this figure is the Shields critical stress threshold for initiation of motion for the observed median grain size of  $D_{50}=400 \mu\text{m}$  and one standard deviation larger ( $D_{85}=800 \mu\text{m}$ ). The transitional region ( $2000 < d/D < 5000$ ) from wave orbital scale ripples to anorbital ripples based on wave orbital diameter scaled by a grain size of  $D_{85}=800 \mu\text{m}$  is shown as the hatched region. A scaling based on  $D_{85}$  is used since this scaling predicts a transition from orbital ripples to anorbital ripples that is not inconsistent with the observations from LEO-15. The critical stress is found from the wave height and period by using linear wave theory to find velocities. The 2.5 grain diameter wave friction factor ( $f_{2.5}$ ) is used to relate velocity to skin friction shear stress.

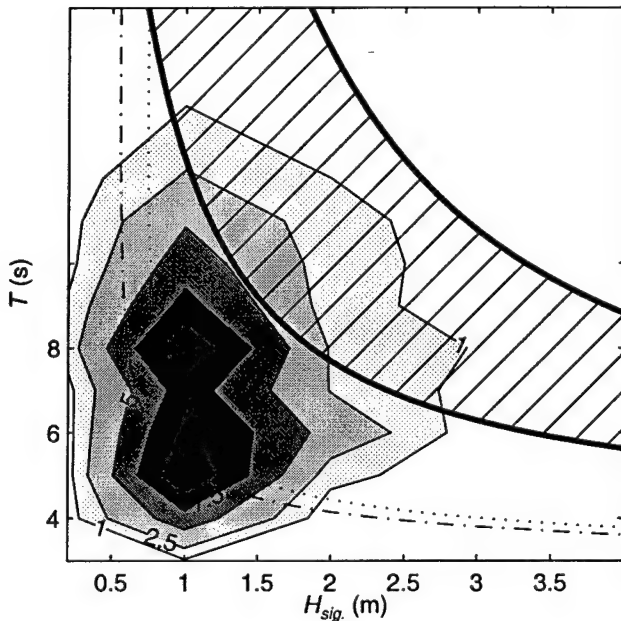


Figure 2-18 Annual significant wave height vs. dominant period frequency of occurrence distribution from 8 years of NDBC [1995] buoy 40009 hourly observations located at the mouth of the Delaware Bay in 28m of water. The total area under the contours integrates to 100%, and contours are labelled in percent. The hatched area is the transitional region from wave orbital scale ripples to anorbital scale ripples defined with  $D=800\mu\text{m}$ . The dash-dotted and dotted lines are the Shields critical limits for initiation of motion for grain sizes of 400 and  $800\mu\text{m}$  respectively.

By integrating the part of the frequency of occurrence distribution that lies above the critical stress it is seen that 74% of the observations fall into this category based on a grain size of  $400\mu\text{m}$ . Thus stresses are typically large enough to form wave orbital ripples that are in equilibrium with wave forcing. By integrating the part of the distribution that lies above the lower limit of the transitional region it is seen that 18% of the observations fall into this category. In our data set 90% of the points lie above the critical stress and only 2% are in the transitional region defined with a grain size of  $800\mu\text{m}$ .

Thus if a transition occurs it will only happen in the more severe storms at LEO-15. Although our deployment occurred during an active tropical storm season, all of these storms passed well offshore of the LEO-15 site generating long period swell, but not locally large waves. The dominant periods of the waves during the most severe event in the deployment were 16-18 seconds, but the significant heights were rarely over 1.5 m. A winter or late fall deployment would be more likely to catch the severe northeast wind storms that would generate locally large waves. Such a deployment could help determine whether the maximum observed ripple wavelength of

100 cm is truly the maximum wavelength possible before a transition to anorbital scaling occurs, or whether the ripples can grow longer than 100 cm.

The wave climatology indicates that until further information is available on the transition to anorbital scaling, a wave orbital scale ripple model is valid at LEO-15 for a large percentage of the time.

## 2.6 Conclusions

Wave orbital scale ripples with  $\lambda/d_s=0.74$  and  $\eta/\lambda=.15$  are clearly the dominant type of bedform observed at LEO-15. The only exception to this is during periods when the current stress becomes significant relative to the wave stress (i.e.  $\tau_c^{sf}/\tau_w^{sf} \sim O(1)$ ), or during periods when the bedforms are not in equilibrium with the wave forcing. Although it is unclear whether a transition to anorbital ripple scaling is occurring, models such as *Clifton and Dingler [1984]* and *Wiberg and Harris [1994]*, with the transition occurring at  $d/D \sim 2000$ , with  $D$  defined by the median grain size ( $D_{50}$ ) do not predict this data set well since this transition predicts a maximum wavelength of 45 cm while the maximum observed wavelength is 100 cm. Scaling the relation  $d/D$  by a grain size one standard deviation above the median ( $D_{85}$ ) allows the model to predict the maximum observed wavelength of 100 cm before a transition occurs. This indicates that scaling these types of models by median grain size alone may not be appropriate and some measure of the width of the grain size distribution should be included. In the case of LEO-15, the presence of the larger grains allowed the ripples to grow larger than the model predicted. Models such as *Nielsen [1992]* or *Grant and Madsen [1982]* that use wave period are able to predict the correct maximum wavelength even when scaled by the median grain size. Collecting data during severe winter storms, with large wave orbital diameters, would help clarify the issue of a orbital-anorbital transition. Also collecting data grain size distribution spatial variability across ripples crest and troughs, along with formulating detailed models of the relative roles of suspended sediment and bedload in the ripple formation process, may help determine the appropriate scaling for a transition. A laboratory study with a narrow and wide grain size distributions with the same median size, and varying wave period with constant orbital diameter could also help clarify the roles of grain size distributions and wave period on ripple geometry.

Although understanding bedform geometry is important for its effect on near-bed hydrodynamics and thus the sediment transport process, the migration of ripples may be the dominant mode of cross-shore sediment transport at a site such as LEO-15 with medium to coarse sand. If the

assumption that the volume of sand contained in the ripples is transported with the ripple is correct, then the ripple transport accounts for an order of magnitude more mass transport than the net suspended transport. Transport models are able to relate this mode of sand transport with a forcing function related to (excess stress)<sup>1.5</sup> with an appropriate scaling constant. Better instrumentation is needed to carefully measure bedload and near-bottom suspended transport and to relate these transport modes to ripple migration. The observations indicate a process where ripples migrated onshore yet suspended sediment travels offshore during storms. Vortex ejection is a possible mechanism for this transport pattern, but it should be emphasized that while the existing observations are consistent with this hypothesis, high resolution 2 or 3-dimensional observations are required to better understand these processes.

### Acknowledgments

The authors would like to thank Dr. Scott Glenn at Rutgers University for making the BASS data available, and the Rutgers University Marine field station and WHOI staff for assistance with the deployment. This work was supported by NOAA New York Bight Research Center grant. NA46GU0149 and ONR grant. N00014-97-1-0556. This is WHOI contribution #

### References

- Amos, C.L., A.J. Bowen, D.A Huntley and C.F.M. Lewis, Ripple generation under the combined influences of waves and currents on the Canadian continental shelf, *Cont. Shelf Res.* Vol. 8, No 10, p. 1129-1153, 1988
- Boyd, R., D.L. Forbes and D.E. Heffler, Time-sequence observations of wave formed sand ripples on an ocean shoreface, *Sedimentology*, 35, p449-464, 1988
- Bagnold, R.A., Motions of waves in shallow water; interaction between waves and sand bottoms, *Proc. R. Soc. London, Ser. A*, 187, 1-15, 1946
- Carstens, M.R., F.M. Nielsen, and H.D. Altinbilek, Bed forms generated in the laboratory under an oscillatory flow: analytical and experimental study, *Tech Memo 28*, 39 pp., U.S. Corps of Eng., Coastal Eng. Res. Cent., Washington, D.C., 1969
- Clifton, H.E., and J.R. Dingler, Wave-formed sedimentary structures and paleoenvironmental reconstruction, *Mar. Geol.*, 60, 165-198, 1984
- Clifton, H.E., Wave-formed sedimentary structures: A conceptual model, in Beach and Nearshore Sedimentation, edited by R.A. Davis, Jr. and R.L. Ethington, SEPM Spec. Publ., 24, 126-148, 1976.
- Craghan, M., Topographic changes and sediment characteristics at a shoreface sand ridge- Beach Haven Ridge, New Jersey, M.Sc. Thesis, 123pp, Rutgers University, New Jersey, 1995
- Dingler, J.R., Wave-formed ripples in nearshore sands, Ph. D. thesis, 136 pp., Univ. of Calif., San Diego, 1974

- Duane, D.B., M.E. Field, E.P. Meisburger, D.J. Swift, and S.J. Williams, Linear shoals on the Atlantic Inner Continental Shelf, Florida to Long Island. Chap. 22. In *Shelf Sediment Transport; Process and Pattern*, edited by D.J. Swift, D.B. Duane and O.H. Pilkey. Dowden, Hutchinson and Ross, Stroudsburg, PA, p 447-498, 1972
- Du Toit, C.G and J.F.A. Sleath Velocity Measurements close to rippled beds in oscillatory flow. *J. Fluid Mech.* 112, p71-96, 1981
- Engelund, F. and J. Fredsoe. Sediment Ripples and Dunes, *Ann. Rev. Fluid Mech.*, 14, p13-37, 1982
- Fredsoe, J. and R. Deigaard, Mechanics of Coastal Sediment Transport, World Scientific, Singapore, 1992
- Grant, W.D. and O.S. Madsen, Combined wave and current interaction with a rough bottom, *J. of Geophys. Res.* 84, p1797-1808, 1979
- Grant, W.D. and O.S. Madsen, Movable bed roughness in unsteady oscillatory flow, *J. of Geophys. Res.* 87 p469-481, 1982
- Grant, W.D. and S.M. Glenn, *Continental shelf bottom boundary layer model, Vol. 1, Theoretical model development*, Woods Hole Oceanographic Inst. 1983.
- Hay, A.E. and D.J. Wilson, Rotary sidescan images of nearshore bedform evolution during a storm, *Mar. Geol.*, 119, p57-65, 1994
- Horikawa, K., Nearshore Dynamics and Coastal Processes, Theory, Measurement, and Predictive Models. Univ. Tokyo Press, Tokyo 1988
- Inman, D.L., Wave generated ripples in nearshore sands, Tech Memo 100, 66pp., U.S. Army Corps of Eng., Beach Erosion Board, Washington D.C. 1957
- Inman, D.L. and A.J. Bowen, Flume Experiments on sand transport by waves and currents. *Coastal Engineering*, Proc. 8th Conf., Am. Soc. Civil Eng., p137-150, 1963
- Irish, J.D., J.F. Lynch, P. Traykovski, and A.E. Newhall "A self contained sector scanning sonar for bottom roughness observations as part of suspended sediment studies," submitted to *J. Atmos. and Ocean Technol.* 1997
- Lee Young, J.S. and J.F.A. Sleath, Ripple formation in combined transdirectional steady and oscillatory flow, *Sedimentology*, 37 p509-516, 1990
- Li, M.Z., C.L. Amos and D.E. Heffler. Boundary layer dynamics and sediment transport under storm and non-storm conditions on the Scotian Shelf, *Mar. Geol.*, 141, 157-181, 1997
- Longuet-Higgins M.S. On the statistical distribution of the height of sea waves. *J. of Marine Research*, Vol. 11, p245-266, 1952
- Lynch, J.F., J.D. Irish, C.R. Sherwood, and Y.C. Agrawal, Determining suspended sediment particle size information from acoustical and optical backscatter measurements, *Cont. Shelf Res.* Vol. 14, No. 10/11, p. 1139-1165, 1994

- Madsen, O.S., Mechanics of cohesionless sediment transport in coastal waters, *Coastal Sediments '91 proceedings*, ASCE, Seattle, p15-27, 1991
- Madsen, O.S. and W.D. Grant, *Sediment Transport in the Coastal Environment*, Report No 209, Ralph M. Parsons Lab. MIT, 1976
- Madsen, O.S., Y. K. Poon and H.C. Graber, Spectral Wave Attenuation by Bottom Friction: Theory, *Coastal Engineering*, Proc. 21th Conf., Am. Soc. Civil Eng, Vol. 1, p492-504, 1988
- Madsen, O.S., P.N. Wikramanayake, "Simple models for turbulent wave current bottom boundary layer flow," US Army Corps of Engineers Coastal Engineering Research Center Dredging Research Program contract report DRP-91-1, 1991
- Meyer-Peter, E. and R. Muller, Formulas for bedload transport, *Proc. Int. Ass. Hydr. Struct. Res.*, Stockholm. 1948
- Miller, M.C. and P.D. Komar, Laboratory investigation of oscillation sand ripples, *J. Sedimentary Petrology*, Vol. 50, No 1, p173-182. 1980
- Mogridge, G.R. and J.W. Kamphuis, Experiments on bedform generation by wave action, *Coastal Engineering*, Proc. 13th Conf., Vancouver, B.C. Am. Soc. Civil Eng., p1123-1142, 1972
- National Data Buoy Center, Climate Summary Tables, Feb. 1995, <ftp://seaboard.ndbc.noaa.gov/data/climatic/44009.txt.gz> (28 Jan. 1997)
- Nielsen, P. *Coastal bottom boundary layers and sediment transport*. World Scientific, Singapore, 1992
- Nielsen, P., "Dynamics and geometry of wave-generated ripples," *J. of Geophys. Res.*, **86**(c7) p 6467-6472 (1984)
- Sheng, J., and A.E. Hay, An examination of the spherical scatterer approximation in aqueous suspensions of sand, *J. Acoust. Soc. Am.*, **83**(2), 598-610, 1988
- Sleath, J.F.A. *Sea Bed Mechanics*, John Wiley & Sons, Inc. New York, 1984
- Sternberg, R., Predicting initial motion and bedload transport of sediment particles in the shallow marine environment, in *Shelf Sediment Transport: Process and Pattern* edited by D.J.P. Swift, D.B. Duane, O.H. Pilkey, p447-498, Van Nostrand Reinhold, New York, 1972
- Swart, D.H., Offshore sediment transport and equilibrium beach profiles. *Delft Hydr. Lab. Publ. No. 131*. 1974
- Traykovski, P., *Sediment Transport at LEO-15*, <http://www.oal.whoi.edu>. 1996
- Wiberg, P.L. and C.K. Harris, Ripple geometry in wave-dominated environments, *J. Geophys. Res.*, **99**, 775-789, 1994
- Wheatcroft, R.A. Temporal variation in bed configuration and one-dimensional roughness at the mid-shelf STRESS site, *Cont. Shelf Res.* Vol. 14, No 10/11, p. 1167-1190, 1994

Wikramanayake, P.N, and O.S. Madsen, Calculation of Movable Bed Friction Factors, US Army Corps of Engineers Coastal Engineering Research Center Dredging Research Program contract report

Williams, A.J., J.S. Tochko, R. L. Koehler, W.D. Grant, T.F. Gross, and C.V. Dunn, Measurement of turbulence in the oceanic bottom boundary layer with an acoustic current meter array, *Jour. of Atmos. and Oceanic Tech.* Vol. 4, No 2, 1987

## CHAPTER 3

### Observations and Models of Sediment Transport at LEO-15: Wave or Current domination?

Peter Traykovski, James D. Irish and James F. Lynch

*Dept. of Applied Ocean Physics and Engineering, Woods Hole Oceanographic Institution, Woods Hole, MA.*

#### Abstract

Suspended sediment transport mechanisms due to wave forcing alone and combined wave-mean current interaction are examined in terms of observations from the LEO-15 site located on the inner continental shelf off southern New Jersey. It was found that wave-forced sediment transport dominated over sediment transport due to mean currents. The wave-forced transport occurred primarily as a result of a vortex ejection mechanism whereby sediment is ejected into the water column after the stronger onshore phase of the non-linear waves. The resulting offshore transport in the next half wave cycle was modeled using a simple grab and dump model for sediment transport over vortex ripples [Nielsen, 1988]. The vertical length scale of the suspension events was found to be equal to the ripple height, and time-averaged transport models that incorporate this vertical scaling were found to predict the transport due to mean currents adequately. Analysis of a long-term current meter record with both wave-forced and mean-current forced transport models revealed that over longer time periods, the wave forced mechanisms are dominant.

#### 3.1 Introduction

On the continental shelf the role of surface gravity waves in sediment transport is usually to initiate sediment motion and/or to suspend sediment. The mean currents are generally responsible for the net transport of sediment, because the waves transport equal amounts of sediment forwards and back. However, as the waves begin to shoal, non-linearities emerge, which create faster onshore velocities for a shorter period of the wave cycle and slower offshore velocities for a longer period of the wave cycle. This non-linear effect combined with a velocity threshold for the initiation of sediment motion as well as the non-linear response of sediment motion to water velocity can result in substantial sediment transport forced by waves alone. In general, on the inner continental shelf the net sediment transport is caused by a combination of sediment transport due to the interactions of waves and currents and sediment transport due to waves alone. This paper investigates the relative roles of these two mechanisms based on observations from the inner continental shelf LEO-15 site. These observations will also be used to examine models for sediment transport due to waves alone and models which account for the combined effect of waves and currents.

Previous studies, both in the laboratory and in the field, have led to a wealth of knowledge about the mechanisms of sediment transport. Laboratory studies on sediment transport due to waves over rippled beds, including those of *Bagnold* [1946], *Inman and Bowen* [1963], *Nakato et al.* [1977], *Sleath* [1982], and *Sato and Horikawa* [1986], have described a vortex ejection process whereby sediment is entrained from the upstream side of a ripple into a vortex in the lee of a ripple crest during the maximum velocity portion of the wave phase. This vortex, and its associated sediment, is then ejected upwards at the velocity reversal. The sediment is then transported back over the ripple crest in the next half wave cycle, and eventually settles out of suspension at a rate determined by the settling velocity. With asymmetrical wave velocities as described by *Sato & Horikawa* [1986] or combined co-linear wave and current flows as described by *Inman and Bowen* [1963], this process leads to a suspended sediment transport that is in the opposite direction of the maximum velocity flow direction. Analysis of field observations of sediment transport due to waves performed by *Vincent and Green* [1990] and *Vincent et al.* [1991] have confirmed these laboratory observations. Simple quantitative models for sediment transport associated with the vortex ejection process have been suggested by *Nielsen* [1988]. More complicated two dimensional numerical models describing the details of the flow structure over the ripples, including the vortex ejection, have been presented by *Longuet-Higgins* [1981], and *Blondeaux and Vittori* [1990]. *Hansen et al.* [1991] included a sediment component in their numerical calculations. Despite the fact that both field and laboratory measurements have confirmed the existence of a vortex ejection process for sediment transport due to wave action over a rippled bed and that models exist to quantify the sediment transport due to this process, there have been no attempts to apply these types of models to field measurements to date. One of the objectives of the work presented in this paper was to compare quantitative models for sediment transport due to waves to field observations.

In contrast, sediment transport models for combined wave and mean current mechanisms, (i.e. where the waves do not transport sediment) have been well tested with field observations. Probably some of the most used models of this type are those developed by Grant, Glenn and Madsen [*Grant and Madsen*, 1979, 1982; *Grant and Glenn*, 1983] (GGM). Their model calculates time averaged velocity and sediment concentration profiles based on wave and current interactions. The sediment profile is determined by a balance between upward turbulent diffusion and gravitational settling. As an alternative to models based on turbulent diffusion, *Nielsen* [1992] suggested an advective model which is more closely related the vortex ejection process. A recent

comparison of these two types of models to field data by *Lee and Hanes* [1996] found that the advective model fit the data better under low energy waves with ripples present, whereas the diffusion-based model fit the data better under higher wave energy conditions, which resulted in sheet flow over a flat bottom.

The analysis of suspended sediment transport presented in this paper is closely related to the analysis of bedform geometry, migration, and the relation between bedform migration and sediment transport presented in *Traykovski et al.* [submitted] (Chapter 2 of this thesis). In that paper the authors showed that the predominant type of ripples present at LEO-15 during the observational period were 2-D wave orbital scale vortex ripples. The ripple wavelength ( $\lambda$ ) was found to be well correlated to the significant wave orbital diameter ( $d_{0,1/3}$ ) with a scaling relation of  $\lambda=0.74d_{0,1/3}$ . The maximum ripple wavelength reached 100 cm, and the mean ripple steepness ( $\eta/\lambda$ ) was found to be 0.15. The ripples migrated consistently in the onshore direction forced by asymmetrical wave velocities. The sediment transport associated with ripple migration was consistent with a wave forced bedload model of  $C_B \theta_{ex}^{1.5}$ , where  $\theta_{ex}$  is the excess Shields bottom stress parameter calculated from wave velocities alone, and  $C_B$  is a constant scaling factor. The scaling factor  $C_B$  was found to be at least ten times greater than  $C_B=8$  as suggested in the *Meyer-Peter and Muller* [1948] formula. While the ripples migrated onshore, the suspended sediment transport due to waves was in the offshore direction. However, based on the assumption that the volume of sediment contained in a ripple is transported at the ripple migration rate, the onshore ripple migration was responsible for twenty times more mass transport than the offshore suspended load. The authors discussed a hypothesis that bedload or near bottom suspended load of the coarser size fractions was swept over the ripple crest in the stronger onshore phase of wave motion, and most of the sediment was deposited on the lee face of the ripple, thus forcing the ripple migration. However, some of the sediment (particularly the finer size fractions) was entrained in the lee vortex, and was subsequently ejected at the velocity reversal and transported offshore. While in *Traykovski et al.* [submitted] the wave forced suspended sediment transport was examined as a possible forcing mechanism for onshore ripple migration, the details of the mechanisms leading to offshore suspended sediment flux will be analyzed and compared to existing models in this paper.

### 3.2 Site Description and Observational Techniques

The observations described in this paper were made during between August 24th and September 9th, 1995 at the Long-term Ecosystem Observatory (LEO-15) site located in 11m depth water off the coast of southern New Jersey. However, biofouling of the instruments became a serious problem towards the end of the deployment so only 25 days of data were used in this analysis. During this time period several tropical storms, some of which retained hurricane strength, passed to the east of the study site. The geophysical environment at LEO-15 consists of a system of sand ridges extending north and east from the coast. The LEO-15 site is located on the southern end of Beach Haven ridge (shown as the closed contour in figure 3-1). These ridges consist largely of medium sand on top of a bed of Holocene lagoonal mud between the ridges [Duane *et al.*, 1972]. The median grain diameters ( $D_{50}$ )

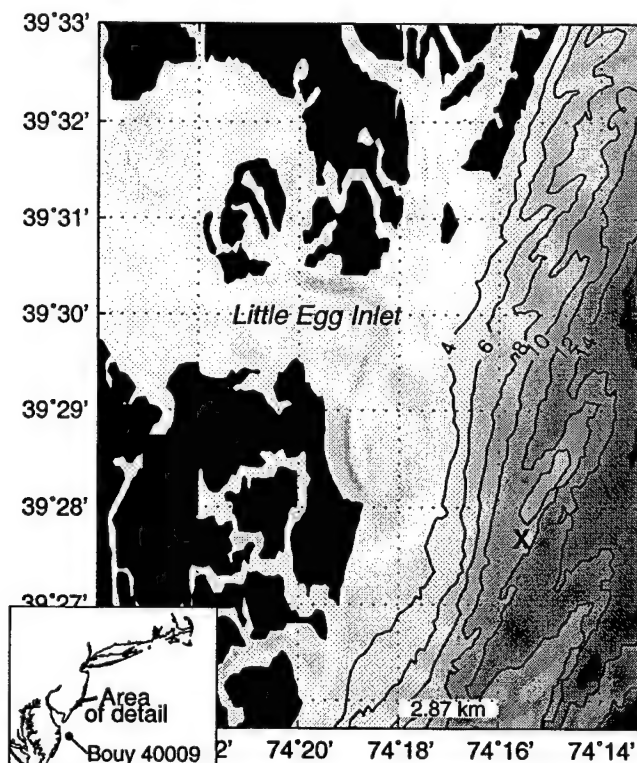


Figure 3-1 LEO-15 bathymetry. The tripod location on the southern end of Beach Haven ridge is marked by an X. Depth contours are labelled in meters, and the grid spacing is 2.87 km.

measured at LEO-15 are typically 1.1 to 1.6  $\phi$  ( $D_{50} \sim 465$  to 330  $\mu\text{m}$ ) with standard deviations of  $\pm 0.5$  to  $\pm 1.0 \phi$  ( $2 \phi = 250 \mu\text{m}$  to  $0.1 \phi = 933 \mu\text{m}$ ) [Craghan 1995].

The instrumentation used to perform the measurements consisted of a rotary sidescan (sector scanning) sonar system, an Acoustic Backscattering System (ABS), and a vertical array of Marsh-McBirney Electro-Magnetic Current Meters (EMCM) and Benthic Acoustic Stress Sensor (BASS) current meters [Williams *et al.* 1987]. The rotary sidescan sonar system provided images of the bedform topography and is described in detail in *Traykovski et al.* [submitted] and *Irish et al.* [submitted].

### 3.2.1 Current meter data processing

The BASS current meters were located at 44, 80, 166, and 250 cm above the seafloor, while the EMCM was located 5 m above the seafloor. Both systems had a burst sampling rate of 4Hz. The BASS sampled every hour with a burst length of 15 minutes, while the EMCM sampled every 30 minutes for 8 minutes, coherently with the ABS system. Since the BASS used a longer burst, the lowest BASS sensor is used to calculate burst-averaged quantities. Burst averaged root mean squared (rms) wave velocities ( $u_{w,rms}$ ) are calculated from the vector wave velocities as:

$$u_{w,rms} = \sqrt{\overline{u_w(t)}^2}. \quad (\text{EQ 3.1})$$

The overbar is used to denote burst averaged quantities throughout the paper. The wave velocity is calculated from the two horizontal velocity axes ( $\hat{u}(t)$ )

$$\hat{u}_w(t) = \hat{u}(t) - \hat{u}_c \quad (\text{EQ 3.2})$$

where the vector mean current velocity ( $\hat{u}_c$ ) with an alongshore component ( $v_c$ ) and an across-shore component ( $u_c$ ) is defined as:

$$\hat{u}_c = \bar{\hat{u}} \quad (\text{EQ 3.3})$$

The vector wave velocity is rotated into a coordinate system that was aligned with the dominant wave direction and the component of instantaneous wave velocity with the maximum variance is defined as  $u_w(t)$ . The dominant wave direction does not vary more than 30 degrees from directly onshore. Wave period ( $T=2\pi/\omega$ ) was calculated from the energy weighted mean frequency ( $\omega$ ) from the spectrum ( $u_{w,i}^2$ ) of wave velocities by [Madsen *et al.*, 1988]:

$$\omega = \frac{\sum \omega_i u_{w,i}^2}{\sum u_{w,i}^2} \quad (\text{EQ 3.4})$$

An important parameter to measure the non-linearity of shoaling waves is the third moment  $\overline{u_w(t)^3}$ <sup>3</sup> or, when normalized by the rms velocity, the skewness:

$$s = \frac{\overline{u_w(t)^3}}{u_{w, rms}^3} \quad (\text{EQ 3.5})$$

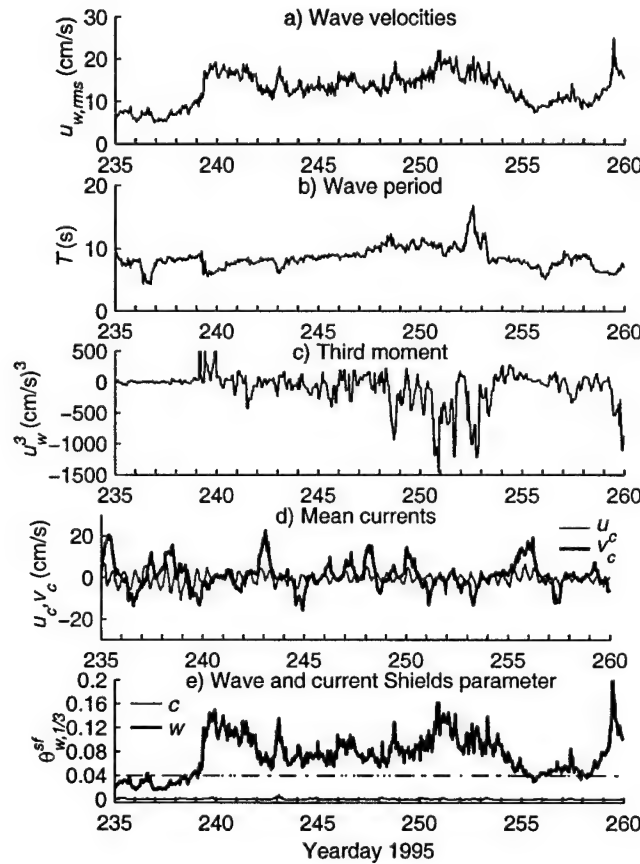


Figure 3-2 Current meter time series: a) Wave velocities, b) Wave period c) Third moment, and d) Mean currents calculated from the BASS sensor 44 cm above the seafloor. e) Wave and current skin friction Shield's parameter based on  $H_{1/3}$  (right y-axis). The critical Shield's parameter for initiation of motion of  $\theta_{crit}^{sf} = 0.04$  is also shown as a dashed line.

The results of these calculations for  $u_{w,rms}$ ,  $T$ ,  $\overline{u_w(t)^3}$ , and  $\dot{u}_c$  on data from the lowest BASS sensor are shown in figure 3-2. While the rms wave velocity reached peaks of 20 cm/s during the periods near day 241 and near day 253, the wave period became much greater (up to 16 s) during the latter period. The third moment also shows several negative (onshore) peaks during this latter time

period. Mean currents are stronger in the alongshore direction (with peaks of up to 20 cm/s) than the weaker tidal currents in the across-shore direction (with peaks of 5 to 8 cm/s).

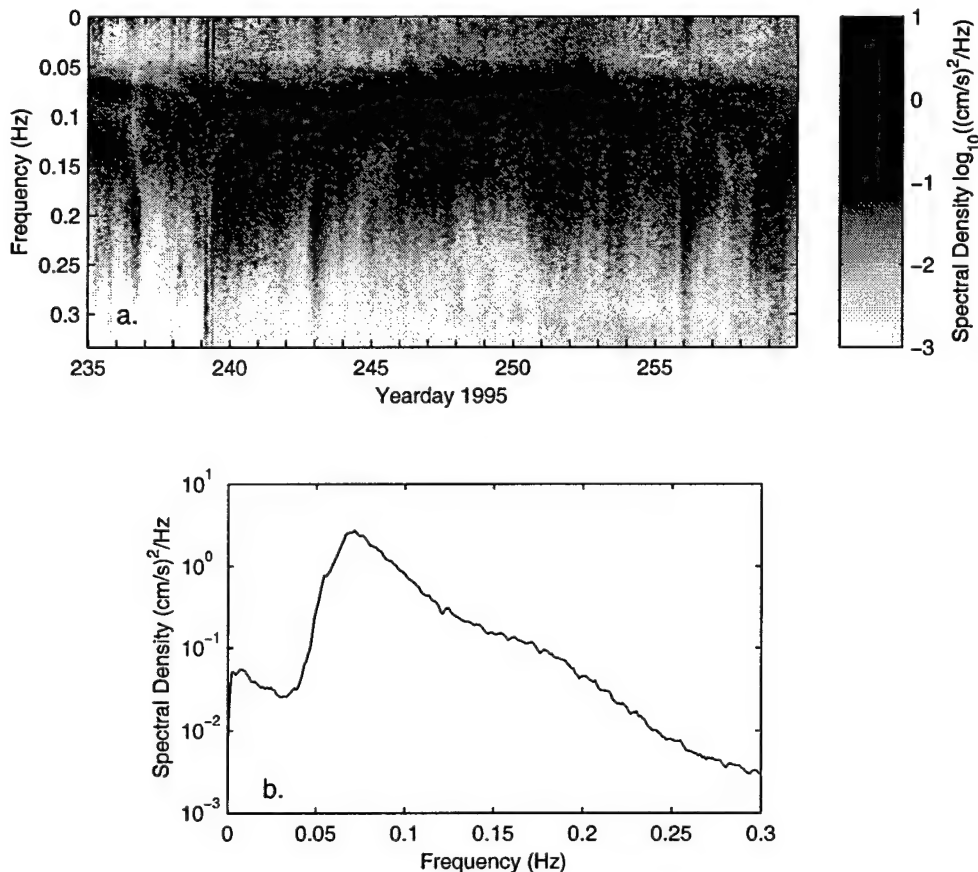


Figure 3-3 a) Spectra of the wave velocity ( $u_w$ ) for each data burst. The spectral level is represented by the grey scale. b) Time average of the spectra from yearday 248 and 254.

As an alternative to the simple one parameter description (wave period) of the spectral energy content of the wave velocities ( $u_w$ ), the spectra for each data burst is shown in figure 3-3a. The temporal variation of the location of the peak in the spectra is fairly reflective of the temporal variation of the wave period shown in figure 3-2b. Several periods are evident where the sea (Frequency  $\sim 0.2$  Hz) is clearly distinguishable from the swell energy (Frequency  $\sim 0.05$  to  $0.1$  Hz). There appears to be a slight increase of low frequency infragravity energy (Frequency  $< 0.04$  Hz) between yearday 248 and 254. The temporally averaged spectra for this period is shown in figure 3-3b. The infragravity spectral density levels are approximately two orders of magnitude less than the swell energy during this period. Integrating the spectral density of entire infragravity band and

the surface gravity wave band ( $0.04 \text{ Hz} < \text{Frequency} < 0.3 \text{ Hz}$ ) reveals that the infragravity band only account for 5% of the wave energy. Thus, it is not expected that the infragravity energy will play a large role in the resuspension dynamics.

The bottom stress is one of the important parameters for sediment transport that can be estimated from the current meter records. The total bottom stress can be divided into a form drag component and a skin friction component, where the skin friction is primarily responsible for sediment motion. When the bottom stress due to waves is much greater than that due to current, the wave skin friction stress can be estimated as:

$$\tau_{w, 1/3}^{sf} = \frac{1}{2} \rho f_{2.5} u_{w, 1/3}^2 \quad (\text{EQ 3.6})$$

Here  $\rho$  is the water density, and the wave friction factor ( $f_{2.5}$ ) is that developed by *Swart* [1974] with the grain roughness defined by 2.5 times the mean grain diameter ( $D_{50}$ ). The wave velocity amplitude ( $u_{w, 1/3} = 1.42\sqrt{2}u_{w, rms}$ ) is defined in a manner consistent with calculating the velocity amplitude based on the significant wave height ( $H_{1/3}$ ). For the purposes of determining initiation of sediment motion and predicting sediment transport, the skin friction bottom stress was non-dimensionalized by taking the ratio of the stress to the immersed weight per unit area; i.e. forming the Shields parameter:

$$\theta_{w, 1/3}^{sf} = \frac{\tau_w^{sf}}{\rho(s-1)gD_{50}} \quad (\text{EQ 3.7})$$

where  $g$  is gravity, and  $s=\rho_s/\rho$  is the ratio of sediment density to water density. A Shields parameter  $\theta_{w, rms}^{sf}$  based on the rms wave velocity amplitude can also be calculated by using  $\sqrt{2}u_{w, rms}$  instead of  $u_{w, 1/3}$ .

The component of skin friction bottom stress due to the mean currents ( $\tau_c^{sf}$ ) was calculated using the GGM non-linear wave current interaction bottom boundary layer model as described by *Madsen and Wikramanayake* [1991]. Although the combined wave and current Shields parameter can be calculated from the vector sum of the wave and current stress, for the purposes of predicting initiation of motion, it is often sufficient to consider only the wave stress since the addition of the current stress makes a negligible contribution.

### 3.2.2 ABS data processing and transport calculations

The 2.5 MHz ABS system measured profiles of acoustic backscattered intensity at a sampling rate of 0.5 s per profile over the bottom 1 m of the water column with 1 cm depth resolution. The system sampled for 4 minutes every half hour. The acoustic beamwidth was 30° as defined by the half power points, which produced a footprint of 25 cm radius at 1 m. The profiles of acoustic intensity were calibrated to estimate profiles of sediment concentration ( $C(z, t)$ ) with units of g/cm<sup>3</sup> [Lynch *et al.*, 1994]. An acoustic system using this frequency is most sensitive to sand from 200μm to 800μm, and is thus ideally suited to measuring the sand sizes found at LEO-15. The possible errors in calibration due to the size dependence of the scattering are not expected to exceed a factor of two [Traykovski *et al.*, submitted].

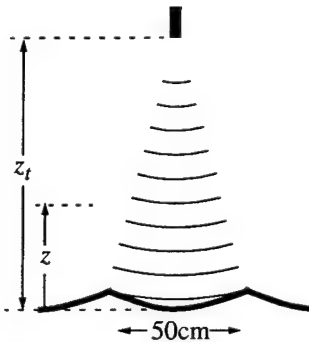


Figure 3-4 Schematic of the ABS sampling volume and ripple morphology

Depth integration of the ABS concentration profiles was calculated as

$$C_z(t) = \int C(z, t) dz. \quad (\text{EQ 3.8})$$

where  $z$  is defined as the distance from the seafloor. The location of the seafloor is determined from the depth bin with the maximum backscattered intensity return in the ABS depth profile ( $z_{t,max}$ ). The depth coordinate  $z$  was calculated based on the distance from the transducer ( $z_t$ ) by  $z=z_{t,max}-z_t$ . The location of  $z_{t,max}$  changes by up to 15 cm over time scales of hours as the ripples migrate past the ABS beam, but changes of more than 1 cm are not visible within the 4 min ABS burst. The lower limit of integration is set at 6 cm to avoid contamination of the ABS suspended sediment concentration estimate by returns from adjacent ripple surfaces when the ABS is located over a ripple trough (figure 3-4). Extrapolating the instantaneous concentration profiles over the bottom 6 cm that are not included in  $C_z(t)$  gives depth-averaged concentration estimates that are usually less than twice as large as the  $C_z(t)$  calculated by equation 3.8. The extrapolation is

performed by setting the concentration in the each of lowest 6 cm to equal to the depth-average of the bins from  $z=6$  to 9 cm (figure 3-5). The upper limit of integration was set at 80 cm to avoid transducer ringing in the first 10 cm.).

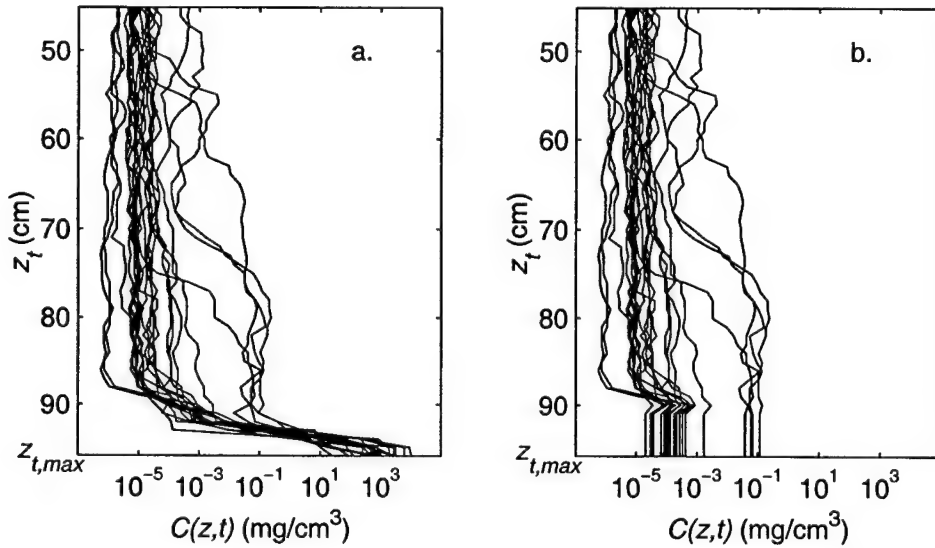


Figure 3-5 Several ABS profiles from a data burst on yearday 248.69. Profiles are separated by 10 seconds. a) The location of the seafloor ( $z_{t,\max}$ ) as defined by the maximum return is located at  $z_t=96\text{cm}$ . The data for concentrations over  $10^{-4}\text{ mg}/\text{cm}^3$  is corrupted below 90cm by the return from adjacent ripple crests. b) The 6 cm above ( $z_{t,\max}$ ) have been extrapolated as described in the text.

The depth integrated instantaneous transport rate was calculated by:

$$Q_{z,w}(t) = u_w(t)C_z(t). \quad (\text{EQ 3.9})$$

In this calculation, the wave velocity has been assumed to be constant over the depth of integration of  $C_z$ . This assumption is justified since the wave velocities across the BASS/EMCM vertical array are essentially constant as a function of depth for the waves with periods over 8 seconds. Linear wave theory predicts a 5% reduction in wave velocity over the bottom 5 m of the water column for 10 second waves. The wave boundary height over orbital-scale vortex shedding ripples is poorly defined, since the ripple height is often greater than the boundary layer thickness (Wiberg and Harris [1994]). However, applying boundary layer thickness scaling of  $\kappa u_{*w}/\omega$ , with  $u_{*w}$  determined from the ripple roughness wave stress, gives wave boundary layer thicknesses less than 8 cm for the range of wave periods and velocities in this data set.

### 3.3 Description of Acoustic Backscattering Data

The acoustic backscattering profiler provides a unique view of the sediment suspension process. Figures 3-6 through 3-9 show 200 seconds of ABS sediment concentration depth profiles ( $C(z,t)$ ), depth integrated sediment concentration ( $C_z(t)$ ), EMCM wave velocity data ( $u_w(t)$ ), and depth integrated wave transport rate ( $Q_{z,w}(t)$ ) for each of the four sampling periods.

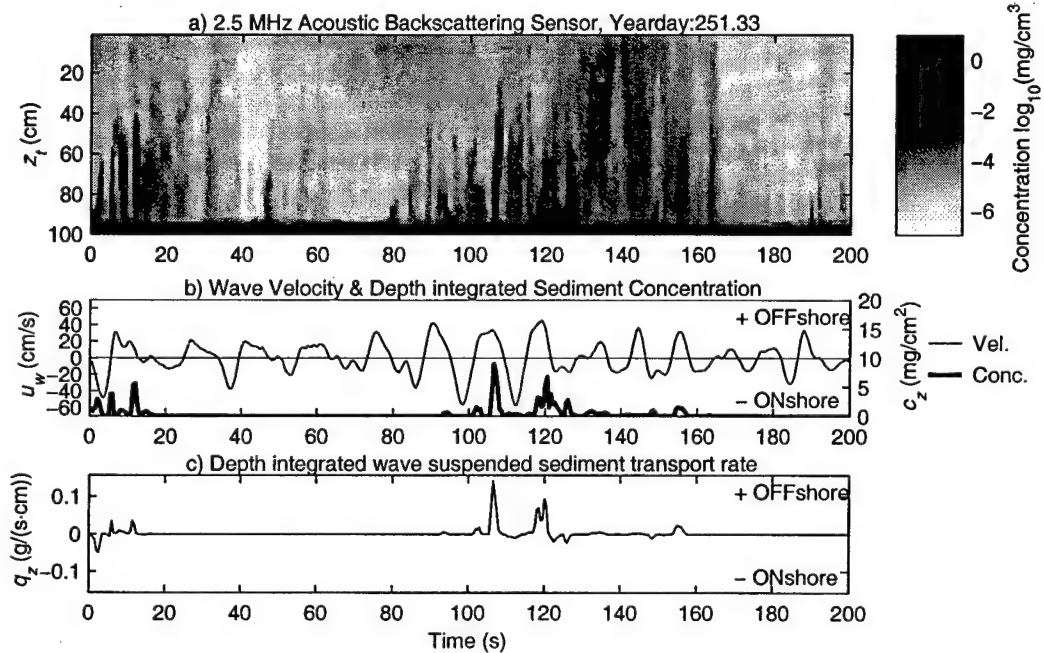


Figure 3-6 a) Acoustic Backscattering System concentration depth profile time series from yearday 251.33. The strong return at 100 cm is from the seafloor. b) Wave velocity ( $u_w$ , left y-axis) and depth integrated sediment concentration ( $C_z$ , right y-axis) time series. c) Depth integrated suspended sediment transport rate due to waves ( $Q_z = u_w C_z$ ). The pulses of offshore transport at 105 and 120 seconds due to a group of non-linear waves are examples of the vortex ejection transport mechanism.

In figure 3-6, for yearday 251.33 a group of two non-linear waves is visible 90 to 120 seconds into the EMCM record. These waves have maximum onshore velocities of 56 cm/s and maximum offshore velocities of 35 to 45 cm/s. There are two distinct peaks in the depth-integrated concentration record which occur in the next half wave cycle after the large onshore velocities. Smaller waves do not produce increased sediment concentrations. These two peaks occurring during the offshore phase of the wave motion result in two pulses of offshore sediment transport. This is consistent with a vortex ejection process in which a cloud of sediment is ejected at the wave velocity reversal. The peak in the ABS record may not occur exactly at velocity reversal, since there may be a time lag associated with the horizontal advection of the cloud of sediment that

was suspended near the ripple crest [Hay and Bowen, 1994]. Following the peak observed in the concentration time series, the concentration falls off rapidly due to the rapid settling velocity of the coarse sediment and the horizontal advection of the cloud of sediment out of the ABS beam. Calibration tank settling tests and empirical fall velocity curves [Gibbs *et al.*, 1971] give settling velocities of  $w_f = 6$  cm/s for the 400 $\mu$ m mean diameter sand present at this location. It is important to note that even if the sediment does not settle out within a half wave cycle, offshore transport can occur if the sediment is suspended at the landward extent of the wave trajectory (*i.e.* the onshore to offshore velocity reversal.)

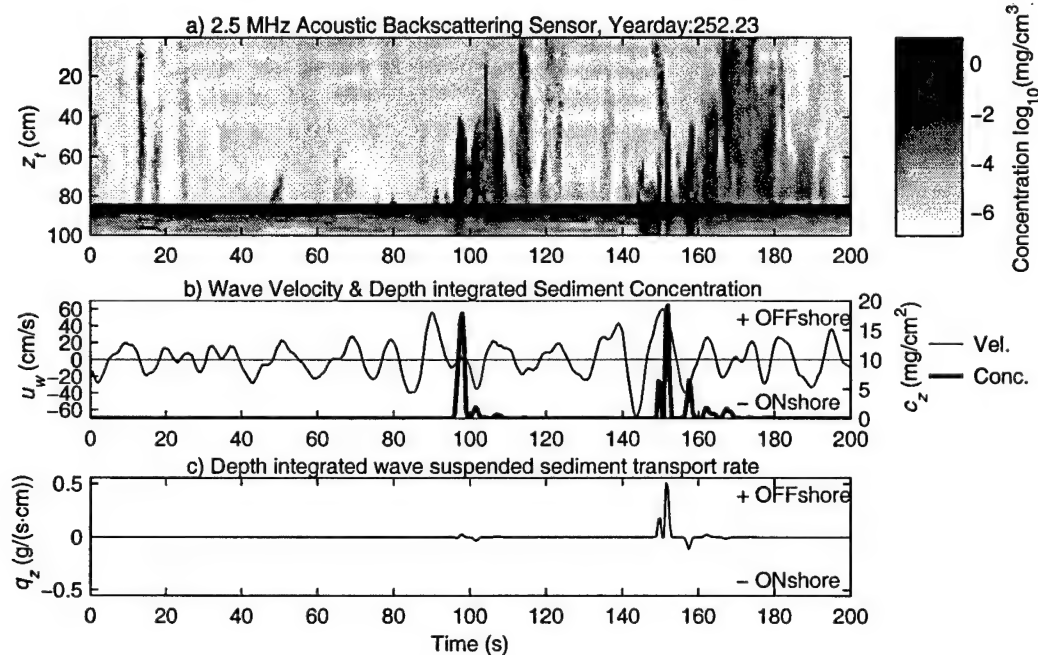


Figure 3-7 Same plots as figure 3-6 with data from yearday 252.23. Examples of the vortex ejection mechanism are visible at 100 and 150 seconds.

Although the concentration drops off rapidly after the peak on the linear scale, the log scale images of  $C(z,t)$  show low concentration clouds of sediment persisting long after the waves have passed. The clouds of sediment suspended between 100 and 120 seconds reach a maximum distance from the seafloor of approximately 60cm (to the center of the cloud) at 135 seconds. Thus, while the peaks of high sediment concentration occur in response to individual waves, the group of waves is capable of forcing low concentration clouds of sediment higher into the water column than can be achieved by single waves, as observed by Osborne and Greenwood [1992,1993] and Huntley and Hanes [1986].

Figure 3-7 (same plots for yearday 252.23) also shows two peaks in sediment concentration due to non-linear waves. The first peak (at 95 seconds) occurs a half wave cycle after a 55 cm/s offshore peak. The particular interference of this wave and a smaller, higher frequency wave cause little transport due to this sediment concentration peak. The peak in concentration at 150 seconds occurs after a maximum onshore velocity of 68 cm/s and is advected offshore by the 60 cm/s velocity in the next half cycle. As in figure 3-6, a low concentration cloud of sediment is seen to rise 60 cm above the seafloor 20 seconds after the wave has passed.

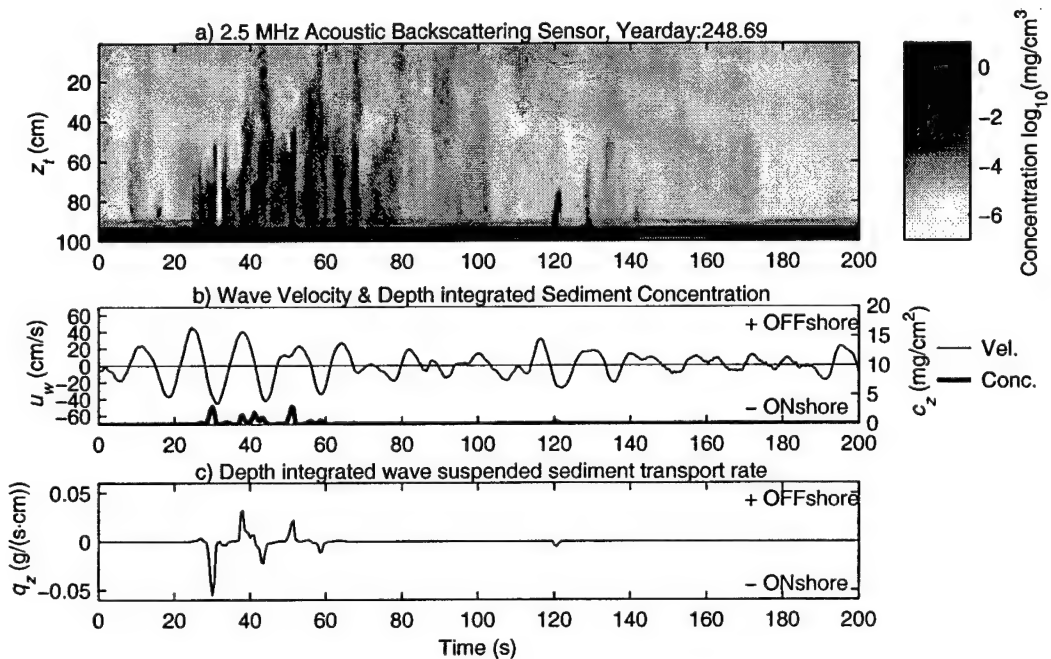


Figure 3-8 Same plots as figure 3-6 with data from yearday 248.69. In this case the group of waves at 20 to 60 seconds has approximately equal onshore and offshore velocities, thus producing little net transport.

While figures 3-6 and 3-7 represent classic examples of the vortex ejection mechanism with nonlinear waves, figure 3-8 is an example of a group of linear waves with nearly equal onshore and offshore velocities of 40 to 45 cm/s. This set of waves results in peak sediment concentrations occurring after each half wave cycle, with the exception of after the first onshore half wave cycle. This is not easily explained, since the third onshore peak (with equal velocity to the first) does result in a concentration maximum. Because there is a concentration peak during each half wave cycle, the transport occurs roughly in equal amounts in both the onshore and offshore directions, resulting in little net transport. This is consistent with the expected behavior of a vortex ejection mechanism in the presence of linear waves.

The data in figure 3-9 show behavior that is not consistent with a vortex ejection mechanism. Here a group of waves is visible 30 seconds into the record, yet there is no peak in the concentration time series until 20 seconds after the waves have passed. There is also a peak in concentration 110 seconds into the record that occurs after a relatively small wave, with larger waves just after it that do not cause peaks in concentration. This uncorrelated response of sediment concentration to water velocity (as measured by the EMCM) shown in figure 3-9 demonstrates that there may be additional water velocity structure or some other agent to suspend sediment that is not well sampled by the EMCM.

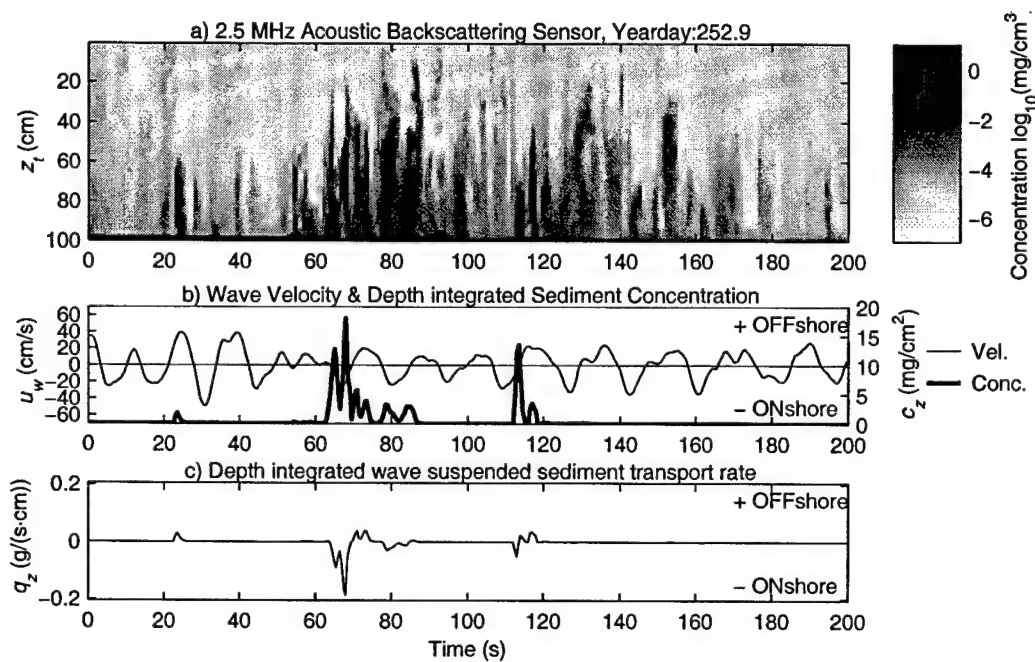


Figure 3-9 Same plots as figure 3-6, with data from yearday 252.9. This burst is not well described the vortex ejection mechanism, since the highest sediment concentrations occur 20 seconds after the large waves have past.

The data bursts shown in figures 3-6 through figure 3-8 were chosen for illustrative purposes as good examples of the vortex ejection mechanism, and are fairly representative of the entire data set. Of the 1280 data bursts analyzed, most show behavior that is consistent with the vortex ejection process. However occasionally data bursts (*e.g.* figure 3-9) show behavior that is not consistent with a vortex ejection mechanism, or any mechanism that the authors are aware of. This variability will be quantified in the following sections as burst-averaged quantities are examined.

### 3.4 Wave time scale bottom boundary condition analysis

In order to quantify the sediment resuspension processes shown in figures 3-6 through figures 3-9, a relation between the hydrodynamic forcing and the amount of sediment in the water is needed. From examining those figures it is clear that bursts of high sediment concentration are only visible after the largest waves. This would indicate either a thresholding effect, or a highly non-linear response of sediment concentration to water velocities.

The bottom boundary condition for sediment resuspension can be specified by two different methods. For the calculation of time-averaged sediment concentration profiles, a reference concentration at a certain height near the bottom ( $\bar{c}_r(z_r)$ ) can be specified. *Smith and Mclean [1977]* suggested the reference concentration is linearly related to the excess bottom stress:

$$\bar{c}_r(z_r) = \begin{cases} \gamma(1-\varepsilon)\left(\frac{|\tau^{sf}|}{\tau_{cr}} - 1\right) & |\tau^{sf}| \geq \tau_{cr} \\ 0 & |\tau^{sf}| < \tau_{cr} \end{cases} . \quad (\text{EQ 3.10})$$

where the sediment concentration is expressed as the volume concentration  $c = C/\rho_s$ , and  $\varepsilon$  is the sediment porosity, with a value of 0.35. The empirical constant  $\gamma$  typically takes on values of about 0.002 for rippled sand beds [*Wikramanayake and Madsen, 1992*]; however this has been a source of much debate in the literature and values from  $10^{-5}$  to  $10^{-3}$  have been reported [*Vincent et al., 1991*]. The critical stress for initiation of motion ( $\tau_{cr}$ ) was determined by a critical Shields parameter of 0.04 from bedform stability, as discussed in *Traykovski et al. [submitted]*.

#### 3.4.1 Determination of pickup function

Alternatively, for time dependent calculations, the bottom boundary condition can be expressed in terms of a vertical flux of sediment from the bottom. This type of boundary condition is often called a pickup function ( $p(t)$ ). The pickup function can be related to the reference concentration by noting that in the time-average over many waves during equilibrium conditions the flux up from the bottom  $\bar{p}$  is equal to the rate of deposition  $w_f \bar{c}_r$ . Based on measurements over a rippled bed, *Nielsen [1992]* suggested a time averaged pickup function of the form:

$$\bar{p} = 0.005 w_f (\theta_{w,e}^{sf})^3 \quad (\text{EQ 3.11})$$

with the enhanced Shields parameter (due to flow enhancement near the ripple crest) given by:

$$\theta_{w,e}^{sf} = \frac{\theta_w^{sf}}{(1 - \pi\eta/\lambda)^2} \quad (\text{EQ 3.12})$$

This time-averaged pickup function may not be directly transferable to the individual wave time scale, since the Shields parameter is based on a time average of wave velocity squared (i.e the r.m.s velocity) as opposed to the actual time average of  $\theta_w^{sf}$ . Since the response of the sediment to individual wave half cycles is desired to quantify the suspension process shown in the previous section, the ABS data was used to estimate the pickup function on the individual wave time scale. This was performed by calculating an instantaneous Shields parameter:

$$\theta_w^{sf}(t) = \frac{1}{2} \frac{f_{2.5} u_w^2(t)}{gD(s-1)}, \quad (\text{EQ 3.13})$$

where  $f_{2.5}$  is the same as used in equation 3.6. This instantaneous Shields parameter was then used to calculate a pickup function of the form

$$p(t) = C_p [\theta_w^{sf}(t)]^n \quad (\text{EQ 3.14})$$

where the constant  $C_p$  and the exponent  $n$  are determined from the data. This pickup function is then integrated over each half wave cycle to estimate the amount of sediment suspended (in units of cm) [Nielsen, 1988].

$$V_{d,u} = \int_{T/2} p(t) dt \quad (\text{EQ 3.15})$$

Here the subscripts d,u indicate vortex ejections at the down and up zero-crossings, respectively. This can be compared to the amount of suspended sediment averaged over the next half wave cycle in the ABS record

$$V_{d,u}^{ABS} = \frac{2}{\rho_s T} \int_{T/2} C_z(t) dt \quad (\text{EQ 3.16})$$

which also has units of cm.

To determine the exponent  $n$ , the time average over a half wave cycle of the instantaneous Shields parameter is calculated as:

$$\theta_{T/2}^{sf} = \frac{2}{T} \int_{T/2} \theta_w^{sf}(t) dt \quad (\text{EQ 3.17})$$

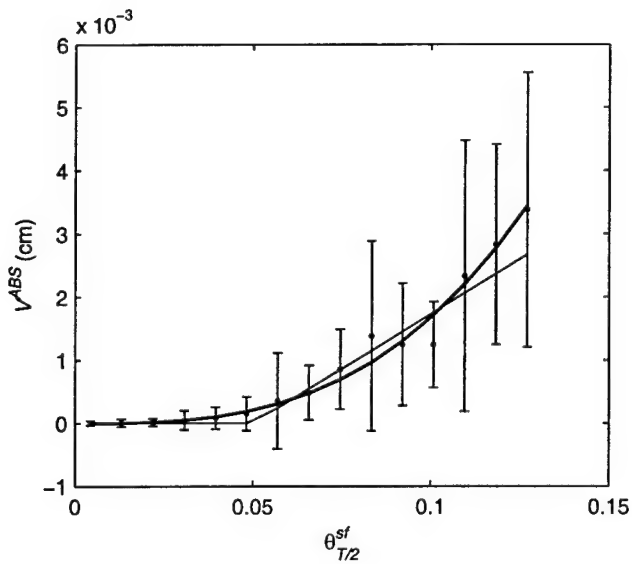


Figure 3-10 Plot of  $V^{ABS}$  vs. the half wave cycle averaged Shields parameter  $\theta_{T/2}^{sf}$ . Dots with error bars represent the mean and standard deviation of the amount sediment suspended by each wave ( $V^{ABS}$ ) as calculated by bin-averaging over 65,000 waves. The thicker line is a cubic relation  $[V^{ABS}] = [θ_{T/2}^{sf}]^3$  and the thin line is a linear relation to the excess Shields parameter as given in equation 3.10.

along with  $V^{ABS}$  for the next half wave cycle, for all of the waves in the portions of the EMCM records that are coherent with the ABS record. Since this represents over 65,000 waves, the results are binned into 15 bins of increasing Shields parameter and the mean and standard deviation of  $V^{ABS}$  is calculated for each bin (figure 3-10).

The bin-averaged data is well described by a model relating the amount of suspended sediment ( $V^{ABS}$ ) to  $[θ_{T/2}^{sf}]^3$ . It should also be noted that although equation 3.10 is for a reference concentration (not a flux boundary condition as is implied by this analysis), a model relating  $V^{ABS}$  linearly to the excess Shields parameter also fits the bin-averaged data quite well. The correlation of the cubic model ( $R^2=0.98$ ) to the bin-averaged data points is about the same as the linear model with thresholding ( $R^2=0.97$ ).

Since the choice of an exponent of  $n=3$  seems to be an appropriate, in order to determine the constant  $C_p$ , equations 3.14 and 3.15 are used with  $n=3$  to calculate  $V$ . In figure 3-11  $V$  is plotted against  $V^{ABS}$  with bin-averaging performed as in figure 3-10. Although there is considerable amount of scatter in the data (as indicated by the high error bars), the bin-averaged mean data display a linear relation between  $V^{ABS}$  and  $V$  with a correlation coefficient of  $R^2=0.85$ . The scaling

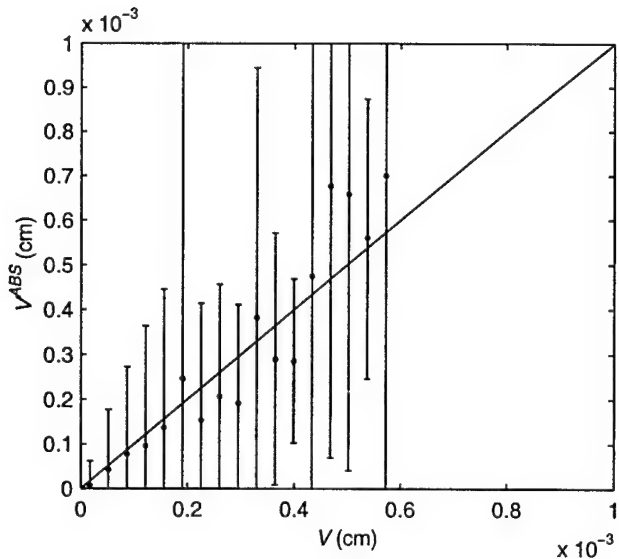


Figure 3-11 The amount of sand suspended in each half wave cycle measured by the ABS ( $V^{ABS}$ ) vs. the amount predicted by equations 3.14 and 3.15 using the EMCM velocity record ( $V$ ). The 45° solid line indicates the best fit of  $V$  to  $V^{ABS}$  using a scaling constant of  $C_p$

constant of  $C_p = 0.11$  was determined using a least squares fit. If the enhanced wave Shields parameter (equation 3.12) is used in equation 3.14, the constant  $C_p$  becomes 0.0025. The large discrepancy between the result with the enhancement factor and the result without is due to the fact that the enhancement factor  $1/(1 - \pi\eta/\lambda) = 1.9$  is raised to the sixth power (i.e.  $0.12/1.9^6 = 0.0026$ ).

The scaling constant of  $C_p = 0.0025$  is a factor of twelve lower than Nielsen's [1992] use of  $C_p = 0.005w_f = 0.03$  for the time-averaged pickup function. Some of this discrepancy can be explained by the difference between calculating the time averaged Shield parameter based on a rms wave height and then raising it to the third power  $(\theta_{w, rms}^{sf})^3$  (as suggested by Nielsen) vs. time-averaging the instantaneous Shields parameter cubed  $(\theta_w^{sf})^3$ . For the wave velocity records in this deployment the ratio  $(\theta_w^{sf})^3 / (\theta_{w, rms}^{sf})^3$  is typically in the range from one to five. The factor of twelve difference between the result from this data set and Nielsen's [1992] result could also be partially attributed to the fact that in this data set the bottom few centimeters are not included in the depth integrated concentration estimate. While the scaling constant for the suspended load had to be increased by an order of magnitude to fit this data set to an existing model, Traykovski *et al.* [submitted] found that the scaling constant in the Meyer-Peter and Muller [1948] bedload model had to be decreased by an order of magnitude. This could be explained by

the fact that some of the near bottom suspended load, which was not observed by the ABS, is partially responsible for the ripple migration.

### 3.4.2 Temporal dependence of the pickup function

In figure 3-10, for values of the half wave cycle averaged Shields parameters above 0.06 the standard deviations become quite large. Some of this variability may be due to the fact that the ejection of sediment due to a large wave does not always occur in the next half wave cycle after the large wave, as shown in section 3.3. To examine this further, the temporal lagged correlation between the depth integrated concentration  $C_z(t)$  and the absolute value of wave velocity  $u_w(t)$  is calculated by:

$$R_{cu}(T_d) = \frac{\int C_z(t') |u_w(t' - T_d)| dt'}{\sqrt{\int C_z^2(t') dt' \int |u_w(t')|^2 dt'}}. \quad (\text{EQ 3.18})$$

The time scale ( $t'$ ) is stretched by the wave period ( $t' = t/T$ ) so that correlation lags can be compared for waves of different periods (figure 3-12a). Thus the units of  $T_d$  are wave periods. Since it was determined that the sediment concentration responds to  $\tau^3$ , the temporal lagged correlation  $R_{cu}^6(T_d)$  was also calculated with  $|u_w^6(t)|$ . These temporal correlations are then averaged across all of the data bursts in the deployment (figure 3-12b).

In figure 3-12a the maximum correlation typically occurs around a lag of  $T_d=0.5$  wave cycles, consistent with the vortex ejection mechanism. There is some variability about this value as spurious peaks can be seen at other correlation lags. The data from yearday 235 to 339 and from 256 to 257 that exhibit flat correlation functions (*i.e.* no peaks are visible) are periods of low suspended sediment activity. While  $R_{cu}$  (the averaged correlation of concentration to  $|u_w|$ ) shows a broad peak around a time lag of  $T_d=0.5$ ,  $R_{cu}^6$  (the averaged correlation of concentration to  $|u_w^6|$ ) shows a much sharper peak.  $R_{cu}^6$  has a maximum value at a lag of  $T_d=0.4$  wave cycles and the centroid of the peak only ( $R_{cu}^6(T_d) - 0.09$ ) occurs at  $T_d=0.6$ . Although the averaged correlation values appear quite low, with a maximum of  $R_{cu}^6(T_d = 0.4) = 0.24$ , the maximum values in the individual data burst correlations are typically around 0.7. The average (over all the data bursts) of the maximum correlation in each burst is equal to 0.68.

By examining a histogram of the temporal lag for maximum correlation of  $R_{cu}^6$  (figure 3-13), it is evident that most of the maxima occur between a delay of 0.25 wave cycles and 1 wave cycle. The

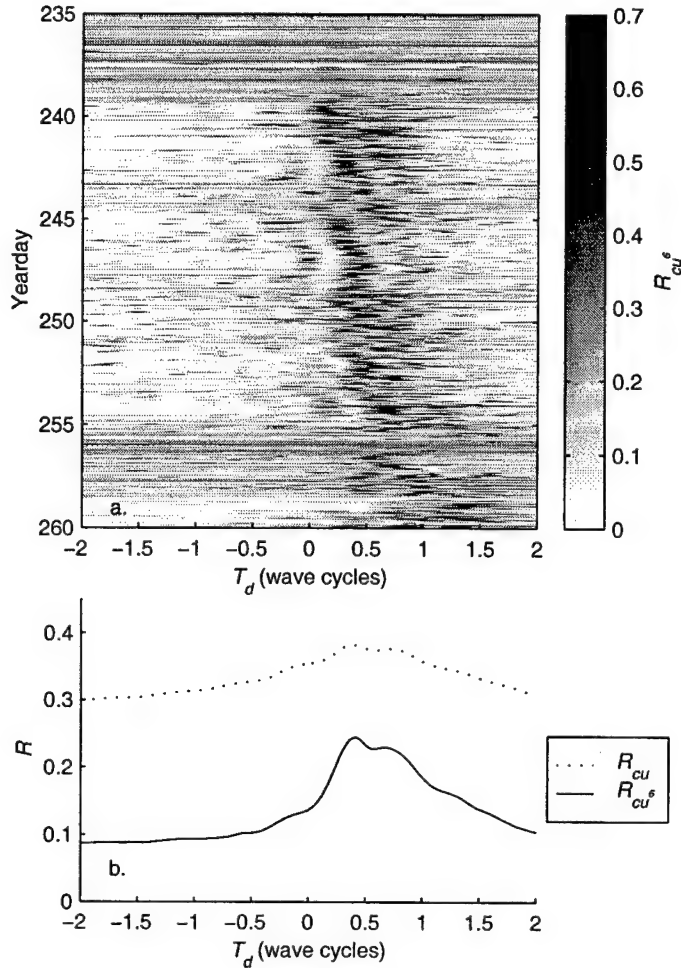


Figure 3-12 a) Temporal lagged correlation values ( $R_{cu}^6$ , gray scale) as a function of time lag ( $T_d$  in wave cycles) for each data burst (yearday) in the deployment. b) The average of  $R_{cu}$  and  $R_{cu}^6$  across all data bursts as a function of time lag ( $T_d$ ).

histogram was calculated for observations between yearday 240 to 255, since this is a period of active resuspension. Integrating the number of maxima that occur between a delay of 0.25 wave cycles and 1 wave cycle reveals that 65% percent of the observations fall within this delay interval.

Both the individual data burst correlations and the averaged correlations show a skewed structure whereby there are higher correlations after  $T_d=0.5$  than before. This is most likely due to the fact that the sediment can stay in suspension for longer than a half wave cycle, and the next half wave cycle may suspend additional sediment. The vortex ejection mechanism predicts that sediment should be ejected at the wave velocity reversal, which would give a maximum correlation lag of

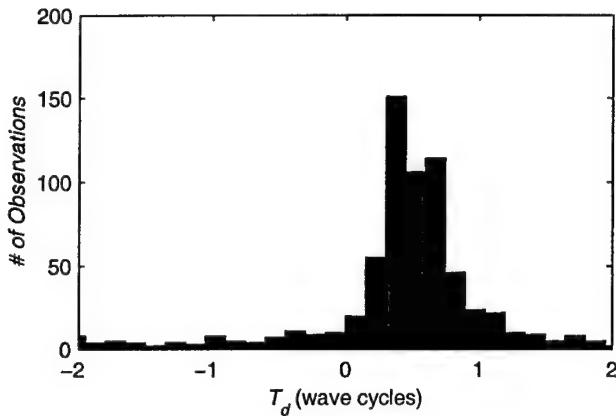


Figure 3-13 Histogram of the temporal lag for maximum correlation of  $R_{cu_g}$ .

$T_d=0.25$ . However, the peak in the ABS record occurs at  $T_d=0.5$ , which is most likely due to the horizontal advection time from the ripple crest (where the ejection occurs) to the location of the ABS beam. The averaged correlation rises sharply after  $T_d=0.25$  to its maximum value at  $T_d=0.4$ . The relation between the lag time and the relative position of the nearest ripple crest to the ABS beam was investigated but no systematic correlation was noted.

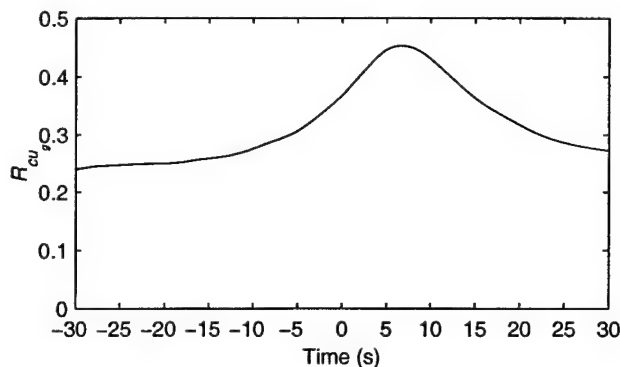


Figure 3-14 Temporal lagged correlation  $R_{cu_g}$  of wave group velocity ( $u_g$ ) and depth integrated sediment concentration ( $C_z$ ) averaged over the data bursts in the period yearday 235 to 260.

Studies performed by *Osborne and Greenwood* [1992,1993] and *Huntley and Hanes* [1986] have noted an increase in suspended sediment concentration towards the end of a wave group. To examine this, the temporal correlation of depth integrated sediment concentration with the wave velocity group envelope ( $u_g$ ) was calculated. Figure 3-14 shows the temporal correlation ( $R_{cu_g}$ )

averaged over the data bursts in the period yearday 235 to 260. The group envelope was calculated by interpolating between the maximum values of  $|u_w|$  in each half wave cycle on to a 2 Hz time basis. The correlation function ( $R_{cu_s}$ ) shows a maximum at a lag of 5 to 8 seconds. This is consistent with the ejection of sediment following a half wave cycle behind the largest wave in the group. A sediment response delayed until the end of the wave group is not evident from this correlation function or in the individual ABS data records (figures 3-6 through 3-8.) However, it should be noted that low concentration clouds of sediment are visible several waves after the largest wave has passed in figures 3-6 through 3-8. The difference between the observations of *Osborne and Greenwood* [1992,1993] and those conducted at LEO-15 are probably due to the fact that the larger grain sizes at LEO-15 allow most of the sediment to settle out within a wave period, which is not true of the suspensions of finer grain sizes observed by *Osborne and Greenwood* [1992,1993].

### 3.5 Simple models for sediment transport by waves

Since the flux of sediment from the seafloor as observed by the ABS is fairly well described by a simple pickup function with a time dependence consistent with the vortex ejection mechanism, the transport due to this mechanism should be predictable by simple models that take the physics of the vortex ejection mechanism into account. *Nielsen* [1988] suggested a very simple “Grab and Dump” (GD) model for sediment transport due to the vortex ejection process. In this model, parcels of sediment are entrained (grabbed) at the velocity reversal after each half wave cycle, transported an average distance of  $A$  (the wave orbital amplitude) in the opposite direction of the entrainment velocity, and then deposited (dumped). The vertical distribution of suspended sediment is not included in this simple transport model. *Nielsen* [1988] calculated the entrainment coefficients ( $V_d V_u$ ) which represent the amount of sand suspended in each half wave cycle as:

$$V_d = 0.5\bar{p}(U_{max}/U_1)^6 \quad V_u = 0.5\bar{p}(U_{min}/U_1)^6 \quad (\text{EQ 3.19})$$

where  $U_{max}$  is the larger onshore velocity maximum,  $U_{min}$  is the smaller offshore velocity, and  $U_1$  is the amplitude of the first harmonic. In this paper, to account for the irregular waves the entrainment coefficients ( $V_d V_u$ ) were calculated using equation 3.15. According to the grab and dump model, the average transport rate over each wave cycle is then:

$$\overline{q_{z,w}} = A(V_u - V_d)/T = \frac{1}{2\pi}(V_u - V_d)U_1 . \quad (\text{EQ 3.20})$$

To account for irregular waves the transport distance was calculated as:

$$A_i = \frac{1}{2} \int_{T/2} u_w(t) dt \quad (\text{EQ 3.21})$$

where the time integral is calculated over the next half wave cycle from the half cycle that was used to calculate  $V_d, V_u$ . The predicted transport rate averaged over each half wave cycle by the grab and dump model is then:

$$q_{z,T/2}^{GD} = 2A_i V/T . \quad (\text{EQ 3.22})$$

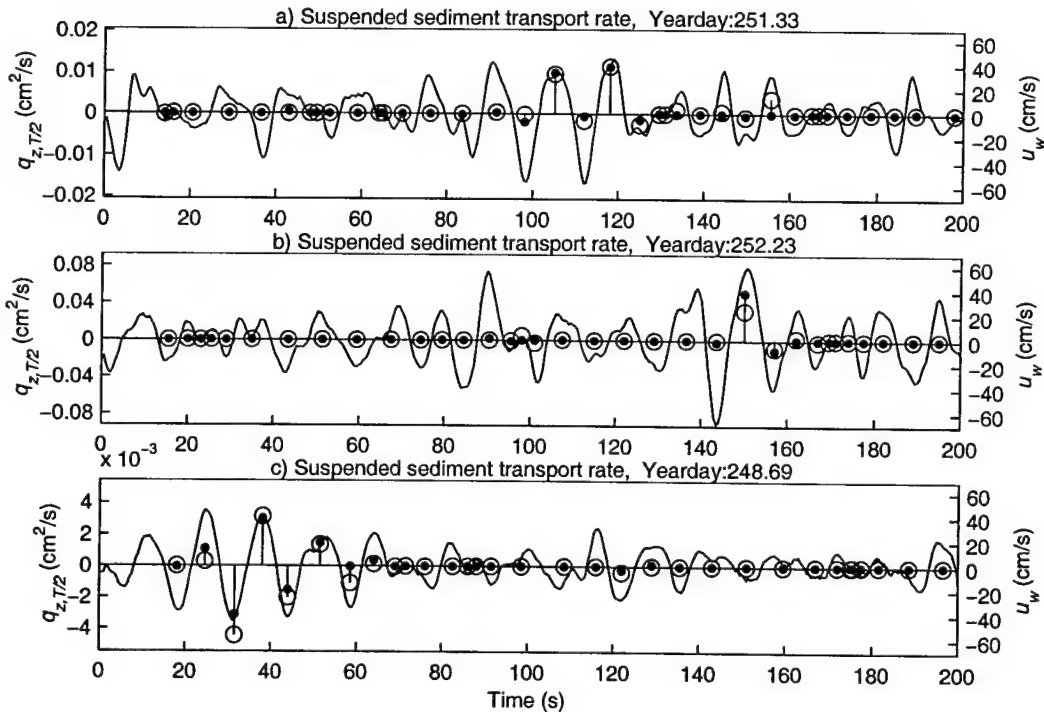


Figure 3-15 Predicted transport rates averaged over each half wave cycle (dots) are compared to measured sediment transport rates averaged over each half wave cycle (open circles) for the first three data bursts (a, b, and c respectively) shown in section 3.3. The instantaneous wave velocity  $u_w(t)$  is also shown (solid line) with scaling indicated by the right y-axis.

The GD predicted transport rate averaged over each half cycle  $q_{z,T/2}^{GD}$  is compared to the equivalent quantity estimated from the ABS data ( $2A_i V^{ABS}/T$ ) for the first three data bursts shown in section 3.3 in figure 3-15. The half cycle averaging begins after the first zero crossing in

each data burst. The fourth data burst shown in section 3.3 will obviously not be well predicted by the model.

The GD model reacts only to the largest waves in each burst, as a result of its dependence on velocity to the sixth power. Both the observed and the predicted sediment transported rate ( $\overline{q_{z,T/2}}$ ) are also related to this non-linear dependence. While the maximum velocity only increases from 45 cm/s (figure 3-15c) to 68 cm/s (figure 3-15b), the sediment transport rate increases from 0.003 cm<sup>2</sup>/s to 0.04 cm<sup>2</sup>/s, consistent with a  $u_w^6$  dependence (*i.e.*  $0.003/0.04=0.075$ ,  $(45/68)^6=0.084$ ). The agreement between the model predicted sediment transport rates in each half wave cycle to the measured data is excellent. Some slight discrepancies of the magnitudes of the individual peaks can be noted.

### 3.5.1 Cumulative wave forced sediment transport

In order to test the model over the whole data set, the measured burst-averaged sediment transport rate ( $\overline{q_{z,w}}$ ) was compared to the burst averaged transport rate predicted by the grab and dump model ( $\overline{q_{z,T/2}}$ ) (figure 3-16a). The cumulative transport flux

$$m_w(t_y) = \int \overline{q_{z,T/2}(t)} dt \quad (\text{EQ 3.23})$$

predicted by the model was also compared to the cumulative transport flux from the data (figure 3-16b). While there are some discrepancies between the model and the observed burst-averaged transport rates (figure 3-16a, as expected given the results of the temporal correlation analysis), the overall magnitudes are in reasonable agreement. The cumulative transport flux shows a period of consistent offshore transport between yearday 245 and 254. This is the same period in which the third moment of wave velocity shows a broad negative peak (figure 3-2c). Thus the offshore sediment transport during this period is consistent with that predicted by a vortex ejection mechanism. The cumulative flux predicted by the grab and dump model shows excellent agreement with the measured data. The higher level of agreement between the modeled and observed cumulative results vs. the burst averaged results is due to the increased averaging time-scale implicit in a cumulative calculation.

### 3.5.2 Grab, Lift and Trickle model

In an attempt to provide a more physically realistic model for the sediment transport due to a vortex ejection mechanism, the grab and dump model was modified to include the effects of a

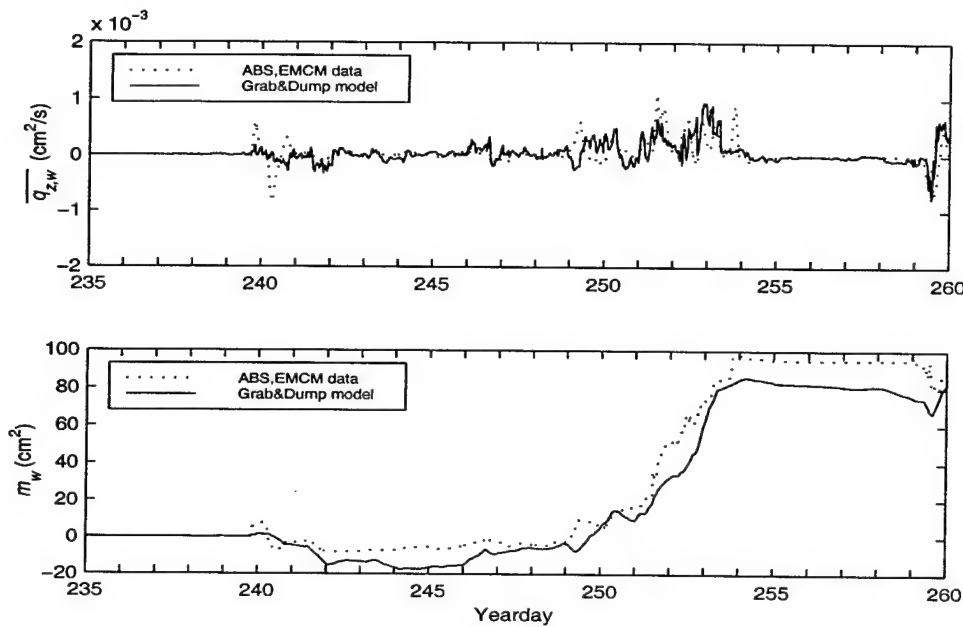


Figure 3-16 a) Burst averaged wave sediment transport rate vs. time for both grab and dump model predictions and measured data. b) Cumulative wave-forced sediment transport flux vs. time for both model predictions and measured data.

vertical distribution of ejection heights. In the “Grab, Lift and Trickle” (GLT) model, sediment is entrained at the velocity reversal according to a pickup function in a similar manner as in the grab and dump model. However, instead of simply transporting the sediment a distance  $A$  from the pickup location, the GLT model entrains the sediment to a certain height based on the hydrodynamic forcing. The sediment is then allowed to settle out over the next few wave cycles (or as long as it takes) according to its settling velocity. This model is similar in concept to the heuristic entrainment model suggested by *Dean* [1973] and more recently *Nielsen* [1988].

The entrainment height is estimated from the ABS data by selecting sediment suspension events occurring in each half wave cycle that meet the criterion of  $C_z > 2 \text{ mg/cm}^2$ . The profile with the maximum depth-integrated concentration ( $C_z$ ) in each event was then used to estimate the vertical length scale ( $L_z$ ) of the suspension as:

$$L_z = \frac{\int z C(z) dz}{\int C(z) dz} \quad (\text{EQ 3.24})$$

where the limits of integration are the same as in equation 3.8. The relationship between this length scale ( $L_z$ ) and the wave orbital diameter ( $2A_i$ ) from the previous half wave cycle was analyzed,

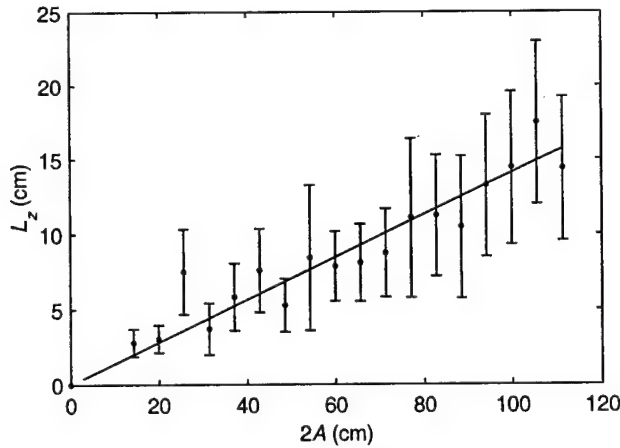


Figure 3-17 Vertical length scale of the suspended sediment profile  $L_z$  vs. the wave orbital diameter ( $2A_i$ ). The data has been bin-averaged and the best linear fit of  $L_z = 0.14(2A_i)$  is shown (solid line).

revealing that there is a linear relationship between them (figure 3-17). As a result of the scatter in the data and the relatively constant wave period, it was also possible to find a linear relation relating velocity and the vertical length scale. However, analysis of the time-averaged vertical length scale (see section 3.6.2) reveals that the length scale is related to the time-averaged wave orbital diameter and not the time-averaged wave velocity. A best fit of  $L_z = 0.14(2A_i)$  was found. This indicates that the vertical length scale is approximately 1.3 times the ripple height ( $\eta$ ), since the ripple wavelength is related to the orbital amplitude by  $\lambda=0.75(2A)$ , the ripple steepness was found to be  $\eta/\lambda=0.15$ , so that  $\eta=0.11(2A)$ .

The GLT model assumes that the sediment is instantly entrained to a height of  $2L_z$  at the velocity reversal ( $t_i$ ), has zero concentration above this height, and a uniform concentration of  $(V/2L_z)$  below this height. The resulting sediment transport rate for each half wave cycle is then calculated as::

$$q_{w,T/2}^{GLT} = \frac{2}{T} \int_{t=t_i}^{t_i + 2L_z/w_f} V \left( 1 - \frac{w_f}{2L_z} (t - t_i) \right) u_w(t) dt \quad (\text{EQ 3.25})$$

where the quantity  $w_f V / 2L_z$  represents the deposition flux onto the seafloor. Since the suspension height ( $2L_z \approx 20$  to  $30$  cm) divided by the fall velocity ( $w_f = 6$  cm) is typically about half a wave

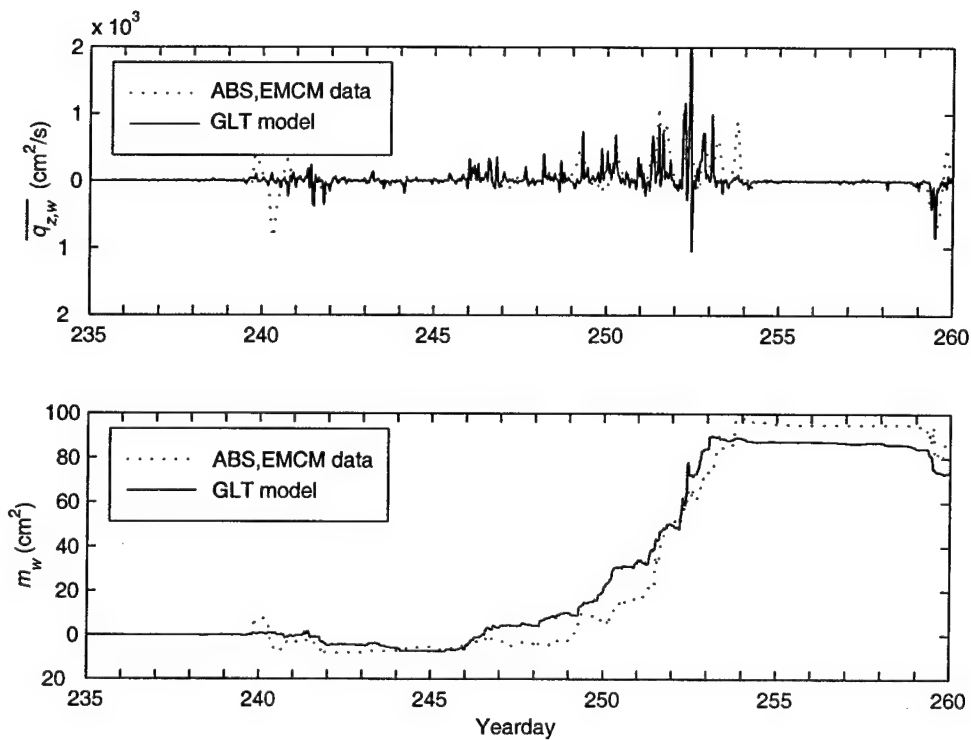


Figure 3-18 a) Burst-averaged wave forced sediment transport rate vs. time for both GLT model predictions (solid line) and measured data (dotted line). b) Cumulative wave sediment transport flux vs. time for both model predictions and measured data.

period, the sediment is transported an average distance of the wave orbital amplitude ( $A_i$ ) consistent with the simpler grab and dump model. Since the GLT model does not predict burst averaged transport rates and cumulative transport flux (figure 3-18) significantly more accurately than the simpler grab and dump model for this data, it would appear that the additional complexity incorporated into the GLT model is not necessary to explain depth integrated wave-forced suspended sediment transport at LEO15.

### 3.6 Sediment transport due to wave-current interaction

#### 3.6.1 Transport Measurements

While the vortex ejection mechanism produces a substantial net offshore sediment transport due to wave motions alone, it is of interest to compare the magnitude of transport due to this mechanism with the transport due to mean currents. Sediment transport due to mean currents was estimated

from the data by multiplying the burst averaged concentration profile  $\overline{C(z)}$  by the burst-averaged velocity profile estimated by the BASS vertical current meter array ( $\overline{\dot{u}_c(z)}$ ).

$$\overline{Q_c} = \overline{\dot{u}_c(z)} \overline{C(z)} \quad (\text{EQ 3.26})$$

While the ABS measures a continuous vertical profile with resolution of 1 cm, the BASS sensors are located at 4 discrete heights of 44, 80, 166 and 250 cm. To calculate a continuous velocity profile for  $\overline{\dot{u}_c(z)}$ , it is necessary to interpolate between the velocity sensors. This was performed using two different methods. The first involved fitting a “law of the wall” log profile to the across-shore ( $\overline{u_c(z)}$ ) and alongshore ( $\overline{v_c(z)}$ ) components of  $\overline{\dot{u}_c(z)}$ .

$$\overline{v_c(z)} = \frac{v_{*c}}{\kappa} \log \frac{z}{z_0} \quad (\text{EQ 3.27})$$

Here  $\kappa=0.4$  is von Karman’s constant and a least-squares fit is used to find the friction velocity ( $v_{*c} = \sqrt{\tau_c/\rho}$ ) and the parameter  $z_0$ . However, this type of fit predicts a zero velocity below  $z_0$ , as can be seen in figure 3-19 where  $z_0$  is equal to 7.7 cm. This would produce unrealistically small sediment transport because the currents are not zero at  $z_0$  due to increasing turbulence in the wave boundary layer. A simple approach to estimating more realistic sediment transport values in the wave boundary layer is to interpolate the current profile from the log fit value at  $z=44$  cm (the elevation of the lowest BASS sensor) to  $\overline{v_c}=0$  at  $z=1$  cm. This modified log fit method is well suited for interpolating velocity profiles with a changing bottom location due to migrating ripples.

An alternate method of generating a continuous velocity profile is to use the GGM wave current interaction model as described by *Madsen and Wikramanayake [1991]*, based on the velocity from the BASS sensor at  $z=44$  cm. This yields a decreased velocity in the lower portion of the water column compared to the modified log profile. While the difference in burst-averaged transport  $\overline{q_c}$  for the profiles shown in figure 3-19 is 60% depending on the method of fitting the current profile, the effect of the choice of fitting method on the net transport is less significant (15 to 25%). The increase in net transport due to using the modified log fit is roughly equivalent to using the GGM profile with the ABS concentration interpolated down to  $z=1$  cm as opposed to using a bottom limit of integration at  $z = 6$  cm.

Figure 3-20 shows the cumulative transport due to the mean current in both the alongshore and across-shore directions, which is calculated by

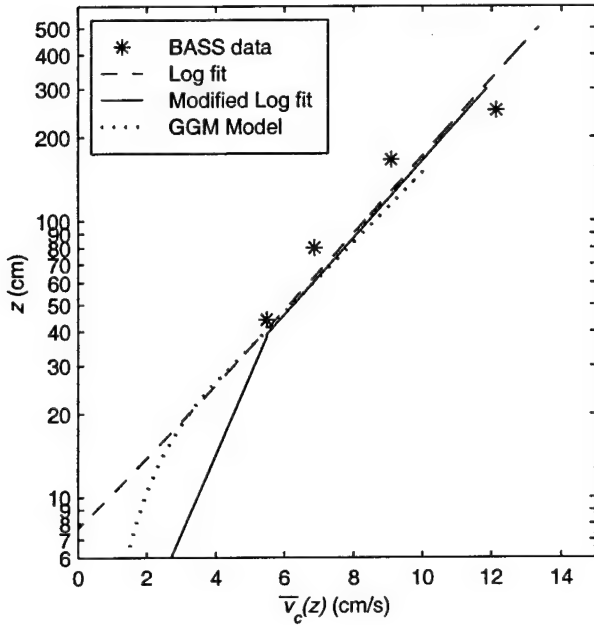


Figure 3-19 Alongshore current profile  $\bar{v}_c(z)$  from the BASS current meter array for a data burst on yearday 245.75. The dashed line is a best log fit to the data, with interpolation to  $\bar{v}_c=0$  at  $z=1\text{cm}$  shown as a solid line. The dotted line is the GGM model fit.

$$M_c(t_y) = \int_{t=235}^{t_y} \int_{z=6\text{cm}}^{80\text{cm}} \bar{Q}_c(t) dz dt \quad (\text{EQ 3.28})$$

using the GGM model current profile and the ABS data. For comparison the cumulative transport due to waves alone ( $M_w = \rho_s m_w$ , equation 3.23) is also shown. While the transport due to mean currents is greater in the alongshore direction than in the across-shore direction, the transport due to waves alone in the offshore direction is over a factor of five times greater than the total transport due to currents. Thus, the dominant mechanism for suspended sediment transport at LEO-15 during this observational period is due to the transport of sediment by non-linear shoaling waves. However, as *Traykovski et al.* [submitted] demonstrated, for this site the transport associated with ripple migration in the onshore direction is a factor of twenty times greater than the suspended transport due to the waves.

### 3.6.2 Modeling of concentration profiles and resulting transport

In order to predict sediment transport due to the mean currents, models for both the mean current vertical profile and the sediment concentration profile are required. In this paper the analysis and

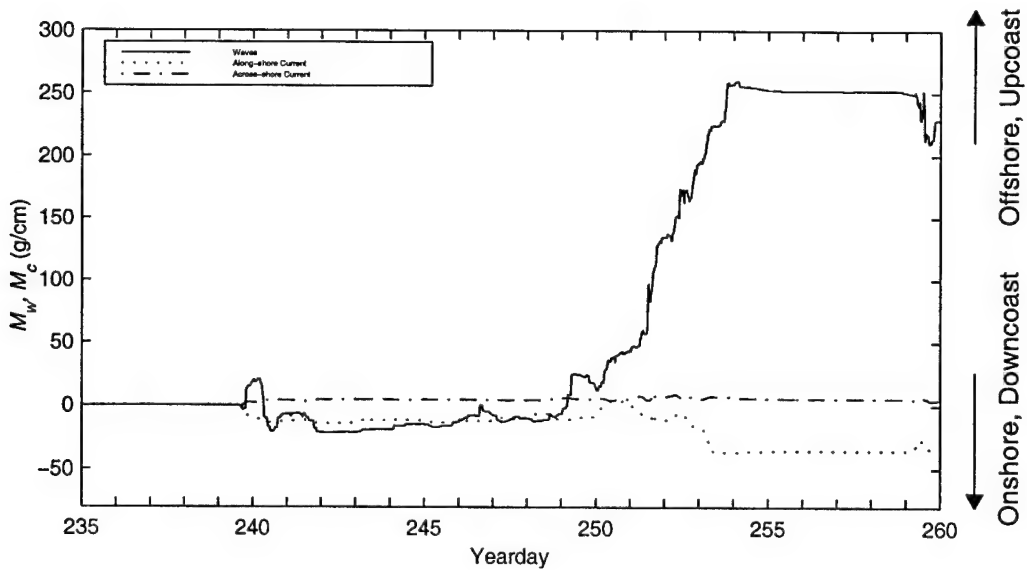


Figure 3-20 Cumulative observed net transport flux due to waves alone ( $M_w$ ) and due to mean currents ( $M_c$ ).

discussion are restricted to sediment concentration profile modeling since models for the current profiles observed at LEO-15 during this period (e.g. dotted line in figure 3-19) are discussed by Styles [1998].

While there are many approaches to comparing models for suspended sediment concentration profiles to data, a simple method of comparison is to examine the time-averaged vertical length scale ( $\bar{L}_z$ ) dependence on hydrodynamic and bottom roughness parameters. The time-averaged vertical length scale (which is an indication of the height of the center of mass of the suspended sediment) can be estimated from the time-averaged concentration profile ( $\bar{c(z)}$ ) by:

$$\bar{L}_z = \frac{\int z \bar{c(z)} dz}{\int \bar{c(z)} dz} \quad (\text{EQ 3.29})$$

Vertical length scales are only calculated when there is a substantial amount of sand in the water column, since if the acoustic scattering is very weak it is probably dominated by fine sediment or organic matter, and may have a uniform distribution over the bottom 1 m of the water column. Two energetic periods were chosen for comparison: the first period is from yearday 240 to 241.5, the second is from yearday 249 to 254. In figure 3-21a, the time-averaged concentration profiles  $\bar{c(z)}$  are displayed along with the vertical length scale ( $\bar{L}_z$ ) in a vertical reference frame relative to the

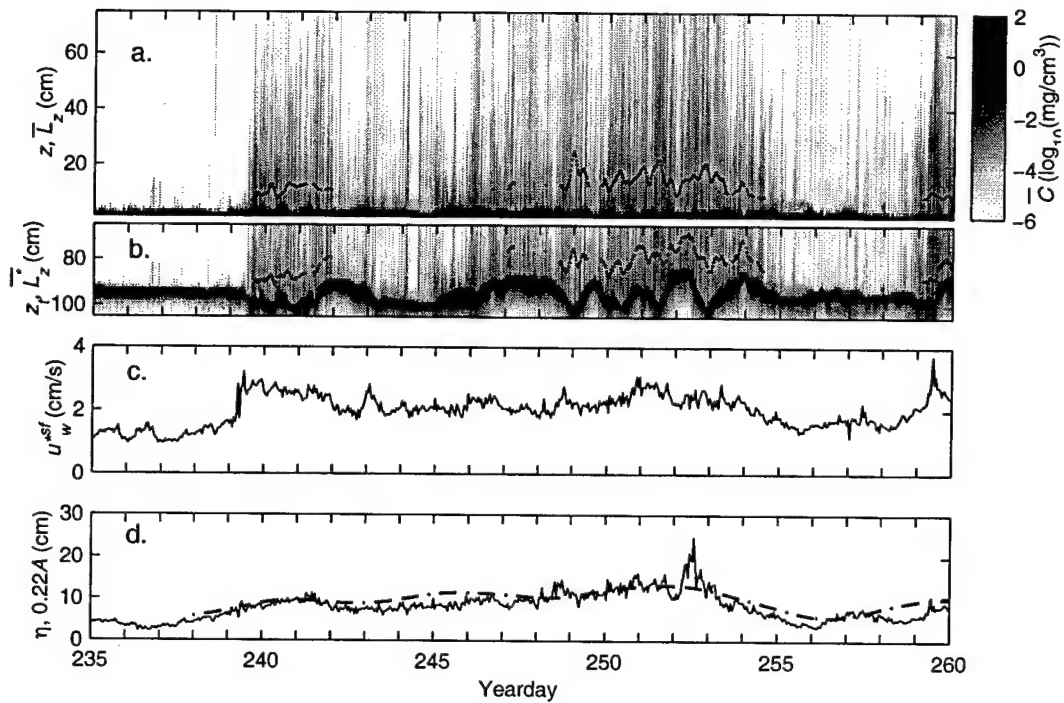


Figure 3-21 a) The gray scale shading represents burst-averaged sediment concentration as a function of time and depth. The time averaged length scale  $\bar{L}_z$  is also shown as the dots approximately 10 cm above the seafloor. b) Same data as panel a, but in the reference frame of the transducer ( $z_t$ ) so that  $\bar{L}_z = z_t - \bar{L}_z$ . c) Wave skin friction velocity  $u_w^{*sf}$  as a function of time. d) The ripple height ( $\eta$ , dash dotted line) and the scaled wave orbital amplitude ( $0.225A$ , solid line) as a function of time.

instantaneous bottom elevation ( $z$ ). If the same data is displayed in a vertical reference frame relative to the transducer ( $z_t$ , figure 3-21b) the migration of the ripples is clearly evident from the strong acoustic return from the seafloor. By comparing figures 3-21a and b there appears to be some correlation between the vertical length scale and the location of the ABS transducer relative to the ripple crest. The vertical length scale appears to be systematically shorter (as measured from the instantaneous bottom) just before a ripple crest migrates past. However, if the vertical length scale is examined in the reference frame of the transducer, the suspended sediment is seen to be closer to the transducer over the ripple crest. If the vertical length scale is averaged over the passage of several ripples, it is evident that the sediment is suspended higher in the second period (yearday 249 to 254) than in the first (yearday 240 to 241.5), (table 3-1). This can be examined in the context of models for the vertical distribution of suspended sediment.

The suspended sediment concentration profile is usually modeled by assuming a time-averaged balance between downward settling and upward gradient diffusion:

$$w_f \frac{d}{dz} \overline{c(z)} = -v_s \frac{d^2}{dz^2} \overline{c(z)} \quad (\text{EQ 3.30})$$

where  $v_s$  is the sediment eddy diffusivity. If the diffusivity is a linear function of  $z$  (i.e.  $v_s = \kappa u^* z$ ) the solution for the concentration profile is:

$$\overline{c(z)} = c_r(z_r) \left( \frac{z}{z_r} \right)^{-w_f/\kappa u^*} \quad (\text{EQ 3.31})$$

The vertical length scale ( $\bar{L}_z$ ) in the Rouse profile is determined by the factor  $-w_f/\kappa u^*$ ; where a large value implies the sediment will remain close to the seabed and  $\bar{L}_z$  will be small. In the case of a highly wave dominated environment, the wave friction velocity  $u_w^*$  can be used for the friction velocity  $u^*$ . While the wave friction velocity depends largely on the wave velocity, it has a weak dependence on the wave orbital amplitude ( $A$ ) and the roughness height ( $\eta$ ) through the parameter  $k_n/A$  in the wave friction factor ( $f_w$ , see equation 3.6) [Swart, 1974].

$$f_w = \exp \left( 5.213 \left( \frac{k_n}{A} \right)^{0.194} - 5.977 \right) \quad (\text{EQ 3.32})$$

Here  $k_n$  is the physical roughness length scale. For the skin friction component of bottom stress,  $k_n$  is related to the grain diameter. Whereas for the form drag component of the bottom stress it is a linear function of the ripple height and sometimes steepness. [Grant and Madsen, 1982; Wikramanayake and Madsen, 1990]. In the case of orbital scale ripples, where the ripple height is linearly related to the wave orbital amplitude, the form drag wave friction factor is a constant. Regardless of which friction factor is used,  $w_f/\kappa u^*$  is nearly identical for the two periods chosen, in contrast to the data where  $\bar{L}_z$  is larger in the second period (table 3-1).

As an alternative to the diffusive model in equation 3.30, advective models have been suggested for modeling the time-averaged vertical profile of suspended sediment [e.g Nielsen 1992, Lee and Hanes, 1996]. In this type of model, the time-averaged concentration profile is determined by the probability of an ejection of sediment reaching a certain height in a manner that is conceptually consistent with time-averaging the GLT model. For this type of model, Nielsen [1984, 1986] suggested a vertical distribution of the form:

$$\overline{c(z)} = \overline{c_r(z_r)} \exp\left(-\frac{z}{L_z}\right). \quad (\text{EQ 3.33})$$

Here the vertical length scale is equal to  $\sqrt{0.225Ak_n}$ , where the roughness scale  $k_n$  is equal to the ripple height ( $\eta$ ), and the wave orbital amplitude ( $A$ ) is scaled by  $(2)(0.75)(0.15)=0.225$ , consistent with orbital scale ripples since  $\lambda=.75(2A)$  and  $\eta/\lambda=0.15$  for this type of ripple. Thus the vertical scaling is essentially equal to one ripple height. This type of scaling is consistent with the data since both  $\sqrt{k_n A}$  and  $L_z$  as estimated from the data become about 25% larger in the second period, and are approximately one ripple height throughout the deployment. It should be noted at this point that diffusive models could also be formulated with a vertical length scale of  $\sqrt{0.225Ak_n}$ , and eddy diffusion can be thought of as a time-averaging of advective processes that are on a shorter time scale than the averaging period. The formulation of an eddy diffusion that increases linearly away from the seafloor is based on a mixing length argument that allows larger eddies to form at increased distances from the seafloor. While this is physically reasonable for mean currents over a wave-rippled seafloor, or waves over a seafloor dominated by small scale roughness (much smaller than the wave orbital amplitude), for wave flows over orbital scale ripples, the eddy size is probably dominated by the ripple dimensions and wave orbital amplitude so that a vertical scaling of  $\sqrt{0.225Ak_n}$  is more appropriate.

	$\overline{L_z}$ (cm)	$w_f/\kappa u^*$	$\sqrt{0.225Ak_n}$ (cm)
Period 1	9.2	2.4	9.2
Period 2	13.0	2.4	12.0
Ratio 1/2	0.7	1.0	0.77

Table 3-1 Time averaged vertical length scales  $\overline{L_z}$ , diffusive vertical distribution parameter  $w_f/\kappa u^*$ , and advective vertical length scale  $\sqrt{0.225Ak_n}$  are compared for period 1 (yearday 240 to 241.5) and period 2 (yearday 249 to 254) in figure 3-21.

Both advective and diffusive models for the vertical distribution of suspended sediment are able to predict the cumulative transport due to mean currents adequately (figure 3-22). The model with the advective vertical scaling predicts the temporal dependence near yearday 250 through 254 slightly better than the diffusive model. In figure 3-22, the bottom boundary condition in equation 3.10 is used for the diffusive model with  $\gamma$  set equal to 0.002. For the advective model a boundary condition of  $\overline{c_r(z_r)} = 0.002(\theta_{w, rms}^{sf})^3$  was used.

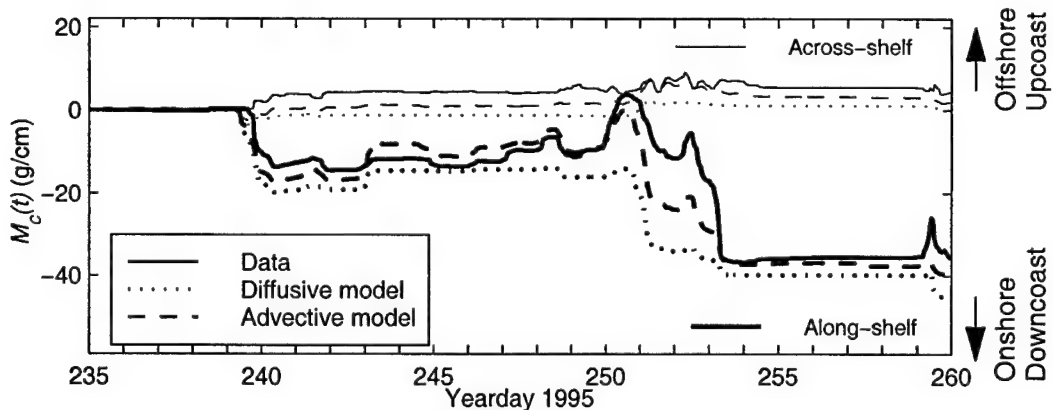


Figure 3-22 Cumulative sediment transport by currents for the data (solid lines), the diffusive model (dotted lines), and the advective model (dashed lines). Thicker lines indicate along-shelf transport and thinner lines represent across-shelf transport.

### 3.7 S4 long term current meter record analysis

To determine which of the observed sediment transport mechanisms was dominant over a longer time period, a one and a half year long current meter record was used as input to the models developed and tested with data from the intensive observational period during the fall of 1995. The current meter data was collected with a InterOceans Inc. S4 current meter located 1 m above the seafloor near the location of the tripod. Selected hydrodynamic parameters calculated from the current meter record are displayed in figure 3-23. While the maximum wave periods observed during the fall 1995 tripod deployment are among the longest observed in the entire 1.5 year record, the wave velocities in the fall deployment are relatively low compared to the high wave velocities observed during winter 1994-95 storms. The mean alongshore current observed during the fall 1995 tripod deployment are also relatively low. However, the ratio of rms wave velocities to mean currents is approximately two for both the fall deployment and the severe storms of the winter of 1994-95. While the Shields parameter did not exceed 0.2 during the fall 1995 deployment, in the winter of 1994-95 it reaches peak values of 0.5 to 0.6. In this region, the wave-formed ripples are expected to decrease in steepness, but since the Shields parameter does not exceed a value of 0.7 to 1.0, a planar bed is not expected, except for brief periods during wave groups when the Shields parameter exceeds this threshold [Wikramanayake and Madsen, 1990]

The three sediment transport mechanisms considered in the context of this longer time period include wave forced bedload (see Traykovski et al. [submitted]), wave-forced suspended sediment

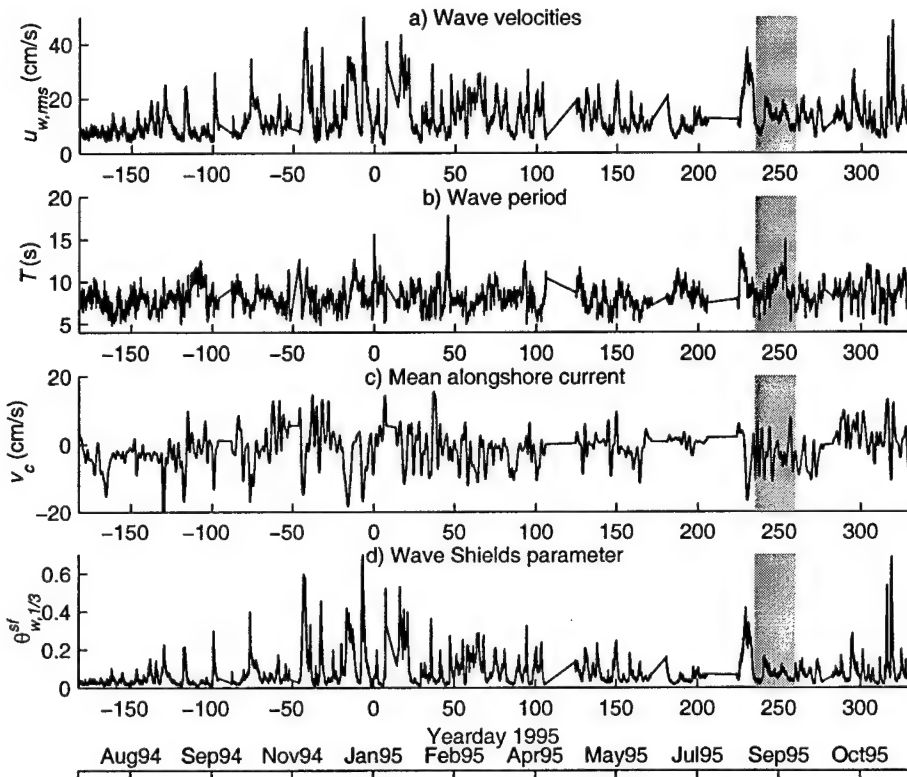


Figure 3-23 Selected hydrodynamic parameters from the S4 current meter record. The period during which data from the bottom tripod was analyzed is highlighted in grey. a) rms wave velocities. b) Wave period as calculated by equation 3.4. c) Mean alongshore currents. d) The wave Shields parameter calculated by equation 3.7.

transport, and suspended sediment transport due to mean currents. The cumulative transport due to wave-forced bedload was calculated based on the bedload model developed in *Traykovski et al.* [submitted] to relate bedload to ripple migration. This model calculates bedload transport based on the instantaneous wave Shields parameter raised to a power of 3/2. The wave-forced suspended sediment transport was calculated using the grab and dump model as described in section 3.5, and the transport due to mean currents was calculated using the advective vertical profile as described in section 3.6. Over the entire year and a half time series the wave-forced transport mechanisms clearly dominate over the transport due mean currents. During the fall 1995 deployment (gray shaded region in figure 3-24) the bedload transport associated with the observed onshore ripple migration was much greater than the observed offshore wave forced suspended transport. However, at the end of the 1.5 year record, the predicted net onshore bedload transport associated with ripple migration approximately balances the grab and dump model predicted net offshore

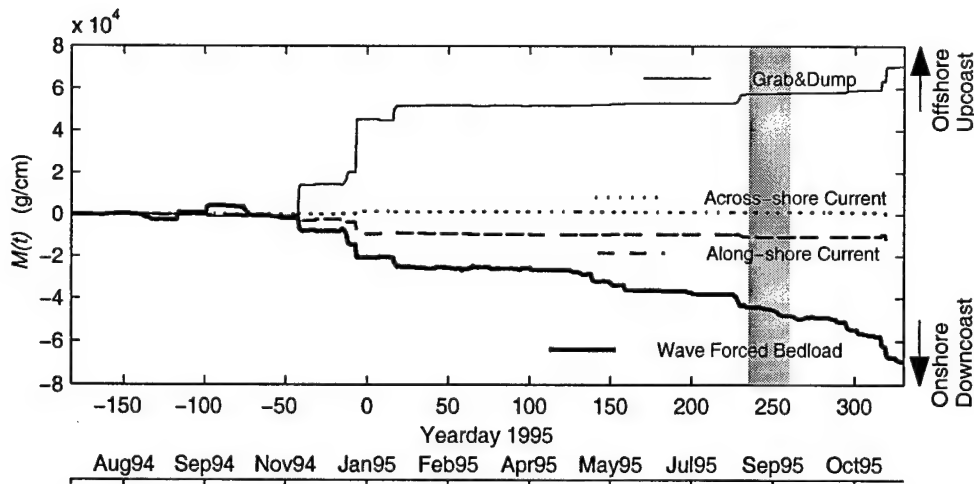


Figure 3-24 Cumulative sediment transport predicted using the S4 current meter data for three transport mechanisms. Wave forced bedload predicted by a wave-forced bedload model (thick solid line) [Traykovski *et al.*, submitted], Wave-forced suspended sediment transport as predicted by the grab and dump model (thin solid line), and suspended sediment transport by mean current as predicted by the advective model (dashed and dotted lines). The period during which data from the bottom tripod was analyzed is highlighted in grey.

suspended transport. At the end of the 1.5 year time series the difference between these two quantities is of the same order of magnitude as the net across-shore transport due to mean currents. However, at any other time the difference between cumulative wave-forced bedload transport and wave-forced suspended transport is far greater than the alongshore transport due to mean currents.

When examining these model results it is important to consider that the bedload model was formulated using observed onshore ripple migration during periods of relatively low bottom stress. It is not clear how these results will be affected by the transition of ripples into a decreased steepness regime. Further observations during high stress periods are needed to verify this. Also, the pickup function in the grab and dump model is proportional to the wave Shields parameter to the third power. For the range of Shields parameters (0 to 0.2) observed during the fall 1995 deployment, the predictions of a cubic pickup function model and those of a model based on a linear proportionality to the excess Shields parameter are very similar (with both fitting the data equally well, see figure 3-10). However, as the Shields parameter begins to exceed 0.2, the predictions of the two types of models diverge. If a linear model were used, the transport due to the grab and dump model would be proportional the Shields parameter with an exponent of 3/2, which is the same exponent as used in the bedload model. The grab and dump model with a cubic exponent pickup function predicts that the three severe storms in the winter of 1994-95 transport

the same amount of sediment as does the more temporally persistent onshore ripple migration over the one and a half year period. However, if the grab and dump model had a 3/2 dependence on the Shields parameter it would predict far less transport than the bedload model, because the constant of proportionality ( $C_p$ , equation 3.14) in the GD model would have to be lower than the constant of proportionality for the bedload model ( $C_B$ ) in order to match the observed fall 1995 data. Again, further observations during high stress periods are needed to determine which specific model parameters are appropriate.

### 3.8 Conclusions

One of the principal goals of the analysis discussed in this paper was to determine the relative roles of wave-forced vs. mean current-forced sediment transport mechanisms over wave-orbital-scale ripples at the LEO-15 site. The analysis reveals unambiguously that the non-linear wave-forced transport mechanisms dominate over those due to mean currents. In particular, the timing of the suspension events on the wave period time scale are well described by a vortex ejection mechanism. The resulting offshore transport of suspended sediment can be successfully modeled by a simple grab and dump (GD) model.

A highly nonlinear dependence of the suspension process (proportional to wave bottom stress to the third power) allows the model to predict transport events that are dominated by the largest waves, consistent with the observed data. However, other forms of the pickup function, such as linear proportionality to excess stress, are also consistent with the data in the limited range of bottom stress conditions observed during the fall 1995 deployment. Collecting additional data during high stress events is required to determine which type of pickup function is suitable over a wide range of bottom stress and ripple morphology conditions.

Although the more complex grab, lift and trickle (GLT) model provides a more physically realistic description of the vertical dependence of the vortex ejection mechanism than does the simpler grab and dump model, it is not necessary to incorporate this additional complexity to describe the depth-integrated sediment transport. However, the vertical length scale of the suspension events that emerged from the formulation of the GLT model is similar to the observed time-averaged vertical length scale. This time-averaged vertical length scale of approximately one ripple height is consistent with describing the suspended sediment concentration profile in terms of an advective process due to eddy ejections from the wave orbital scale ripples. A diffusive vertical length scale

model that depends on a parameter estimated from wave velocities (such as wave bottom stress) does not match the observed length scales as accurately as the advective length scale model. The suspended sediment transport predictions due to mean currents for both the advective and the diffusive model fit the data reasonably well, with the advective model performing slightly better during periods with large ripples.

Although interpreting a long-term current meter record with the existing sediment transport models provides interesting insights into the relative roles of the various transport mechanisms, long-term observations of sediment transport, including extreme storm events, are required to evaluate the accuracy of these models under a variety of conditions. The analysis of the long-term current meter records does show that wave-forced transport processes dominate over those due to mean currents. Thus, in order to accurately model sediment transport at an inner continental shelf site such as LEO-15 characterized by orbital scale vortex-shedding ripples and non-linear surface gravity waves, the transport due to wave-forced processes must be considered.

### **Acknowledgments**

The authors would like to thank Dr. Scott Glenn at Rutgers University for making the BASS and long-term S4 current meter data available, and the Rutgers University Marine field station and WHOI staff for assistance with the deployment. This work was completed in partial fulfillment of the requirements for a Ph.D., and the first author would like to thank his thesis committee, which included the co-authors, Ole Madsen and Henrik Schmidt from the Massachusetts Institute of Technology. This work was supported by NOAA New York Bight Research Center grant. NA46GU0149 and ONR grant. N00014-97-1-0556. This is WHOI contribution #.

## References

- Bagnold, R.A., Motions of waves in shallow water; interaction between waves and sand bottoms, *Proc. R. Soc. London, Ser. A*, 187, 1-15, 1946
- Blondeaux, P., G. Vittori, Vorticity dynamics in an oscillatory flow over a rippled bed, *J. Fluid Mech.* 226 p.257-28, 1991
- Craghan, M., Topographic changes and sediment characteristics at a shoreface sand ridge- Beach Haven Ridge, New Jersey, M.Sc. Thesis, 123pp, Rutgers University, New Jersey, 1995
- Dean, R.G. Heuristic Model of sand transport in the surf zone, Proc. First Australasian Conf. Coastal Eng., Sydney, pp. 208-214. 1973
- Gibbs, R.J., M.D. Mathews and D.A. Link, The relation between sphere size and settling velocity, *J. Sed. Petrology*, Vol 41, pp 7-18, 1971
- Grant, W.D. and O.S. Madsen, Combined wave and current interaction with a rough bottom, *J. of Geophys. Res.* 84, p1797-1808, 1979
- Grant, W.D. and O.S. Madsen, Moveable bed roughness in unsteady oscillatory flow, *J. of Geophys. Res.* 87, p469-481, 1982
- Grant, W.D. and S.M. Glenn, *Continental shelf bottom boundary layer model, Vol. 1, Theoretical model development*, Woods Hole Oceanographic Inst. 1983.
- Hansen, E.A., J. Fredsoe, and R. Deigaard, Distribution of suspended sediment over wave generated ripples, Int. Symposium on the transport of suspended sediment and its mathematical modeling, Florence, Italy p. 111-128, 1991
- Hay, A.E. and A.J. Bowen, Coherence scales of wave induced suspended sand concentration fluctuations. *J. of Geophys. Res.* 99 (c6) p. 12,749-12,765, 1994
- Inman, D.L. and A.J. Bowen, Flume Experiments on sand transport by waves and currents. *Coastal Engineering*, Proc. 8th Conf., Am. Soc. Civil Eng., p137-150, 1963
- Irish, J.D., J.F. Lynch, P. Traykovski, and A.E. Newhall "A self contained sector scanning sonar for bottom roughness observations as part of suspended sediment studies," submitted to *J. Atmos. and Ocean Technol.* 1997
- Longuet-Higgins M.S., Oscillating flow over steep sand ripples, *J. Fluid Mech.* 107 p.1-35, 1981
- Lynch, J.F., J.D. Irish, C.R. Sherwood, and Y.C. Agrawal, Determining suspended sediment particle size information from acoustical and optical backscatter measurements, *Cont. Shelf Res.* Vol. 14, No. 10/11, p. 1139-1165, 1994
- Madsen, O.S., P.N. Wikramanayake, "Simple models for turbulent wave current bottom boundary layer flow," US Army Corps of Engineers Coastal Engineering Research Center Dredging Research Program contract report DRP-91-1, 1991
- Meyer-Peter, E. and R. Muller, Formulas for bedload transport, *Proc. Int. Ass. Hydr. Struct. Res.*, Stockholm. 1948

- Nakato, T., F.A. Locher, J.R. Glover, and J.F. Kennedy, Wave entrainment of sediment from rippled beds, *J. of the Waterway, Port, Coastal, and Ocean Division*, Proc. Am. Soc. Civil Eng., 103 (WW1) p83-100, 1987
- Nielsen, P., Field measurements of time averaged suspended sediment concentrations under waves, *Coastal Eng.*, (8), p 51-73, 1984
- Nielsen, P., Suspended sediment concentrations under waves, *Coastal Eng.*, (10), p 23-31, 1986
- Nielsen, P., Three simple models of wave sediment transport, *Coastal Eng.* (12) p 43-62, 1988
- Osborne, P.D., and B. Greenwood, Frequency dependent cross-shore suspended sediment transport. 1. A non-barred shoreface, *Marine Geology*, 106, p 1-24, 1992
- Osborne, P.D., and B. Greenwood, Sediment suspension under waves and currents: time scales and vertical structure, *Sedimentology*, 40, p 599-622, 1993
- Sato, S. and Horikawa, K., Laboratory study on sand transport over ripples due to asymmetric oscillatory flows. *Coastal Engineering*, p 1481-1495, 1986
- Sleath, J.F.A., The suspension of sand by waves, *J. of Hydraul. Res.* 20(5), p 439-451, 1982
- Styles, R - Modeling of Sediment Transport at LEO-15, Ph.D.. Thesis, Rutgers University, New Brunswick, NJ. 1998
- Swart, D.H. Offshore sediment transport and equilibrium beach profiles. *Delft Hydr. Lab. Publ. No. 131.* 1974
- Traykovski, P., A.E. Hay, J.D. Irish, J.F. Lynch, Geometry, migration, and evolution of wave orbital ripples at LEO-15, Submitted to *J. of Geophys. Res.* 1997
- Vincent, C.E., and M.O. Green, Field measurements of the suspended sand concentration profiles and fluxes and of the resuspension coefficient  $\gamma_0$  over a rippled bed, *J. Geophys. Res.* 95 (c7) p. 11,591-11,601, 1990
- Vincent, C.E., D.M. Hanes, and A.J. Bowen, Acoustic measurements of suspended sand on the shoreface and control of concentration by bed roughness, *Mar. Geol.*, 96, p1-18. 1991
- Wiberg, P.L., and C.K. Harris, Ripple geometry in wave-dominated environments, *J. Geophys. Res.*, 99, 775-789, 1994
- Wikramanayake P.N., and O.S. Madsen, Calculation of movable bed friction factors," Technical Progress report No. 2, Dredging research program, U.S. Army Corps of Engineers. Coastal Engineering Research Center, 1990
- Williams, A.J., J.S. Tochko, R. L. Koehler, W.D. Grant, T.F. Gross, and C.V. Dunn, Measurement of turbulence in the oceanic bottom boundary layer with an acoustic current meter array, *Jour. of Atmos. and Oceanic Tech.* Vol. 4, No 2, 1987

## CHAPTER 4

### Summary and Conclusions

#### 4.1 LEO-15 as a proto-typical site

Observations conducted during the late summer of 1995 at LEO-15 revealed that wave-forced sediment transport processes are the dominant mechanisms of sediment transport over the wave orbital scale ripples found during this time period. The extension of these results to longer time scales was discussed in chapters 2 and 3, with the conclusion that the observations should be typical of other storm events at LEO-15. The primary exception to this may be the rare extreme storm events with high bottom stresses that may erode the ripples. Further observations at LEO-15 are required to quantify sediment transport during these periods.

The remaining important question to be addressed is: are these results transferable to other sites? It is anticipated that in environments with wave-orbital scale ripples, non-linear waves, and relatively weak currents, the results found in this study should be directly applicable. These conditions are generally found in a range of water depths outside the surf zone from one to two meters depth with short wavelength surface gravity waves, up to ten to twenty meters depth with long wavelength surface gravity waves, such as at LEO-15. Relatively coarse sand is necessary for the formation of orbital scale ripples; with fine sand an orbital ripples are formed, and the results of the analysis presented in this thesis may not apply. A complete study on this topic would include investigating the spatial distribution of sediment grain sizes and the predominant wave and current conditions in the area of interest. Predictions based on this type of study could then be tested with actual observations of sediment transport processes as was performed at LEO-15.

#### 4.2 Summary of thesis results

##### Bedform Geometry

- The predominant bedforms at LEO-15 were found to be wave orbital scale ripples with ripple wavelengths equal to 3/4 of the wave orbital diameter, aligned with the ripple crests parallel to the wave crests. Mean current-formed bedforms were rarely observed.
- The ripples followed a characteristic evolution of ripple type during storm events, transitioning from: 1) *relic ripples* left from the previous storm, to 2) *3-d wave orbital scale ripples*, to 3) *2-d wave orbital scale ripples*, and finally back to 4) *relic ripples*, which

remain after the storm passed until the next storm.

- Models for ripple geometry, such as *Nielsen* [1981] or *Grant and Madsen* [1982], that included a wave period dependence could predict the observed ripple wavelength. The *Wiberg and Harris* [1994] model, based only on the grain size and wave orbital diameter, required using a grain size parameter larger than the median to allow the predicted ripple wavelengths to reach the maximum observed wavelengths of 1 m.

### Ripple Migration

- The ripples migrated consistently in the onshore direction (the direction of wave propagation), forced by non-linear waves.
- The sediment transport associated with ripple migration was the dominant transport mechanism at LEO-15 during the observational time period. Based on the assumption that ripples transport their entire volume sand at the ripple migration rate the sediment transport associated with ripple migration was twenty times greater than the wave-forced suspended sediment transport at this site.
- Since the ripple migration was in the direction of wave propagation, and wave-forced suspended transport was of an insufficient magnitude to force ripple migration, it was hypothesized that ripple migration was forced by unobserved bedload or near-bottom suspended load. A simple bedload model, with transport proportional to excess wave bottom stress to the 3/2 power, was used to relate the sediment transport associated with ripple migration to the non-linear wave velocities.

### Suspended Sediment Transport

- Despite the fact that the ripples migrated onshore, wave-forced suspended transport was found to occur in the weaker offshore phase of the wave motion, resulting in net offshore wave forced suspended sediment transport.
- The onshore ripple migration and offshore suspended sediment flux can be explained in terms of a vortex ejection process whereby: 1) sediment is swept over the ripple crest towards the shore in the faster, shorter onshore phase of wave motion; 2) some of this sediment (particularly the larger grain size fraction) is deposited in the lee of the ripple crest thus forcing the ripple migration; 3) the remaining sediment is entrained into a lee vortex, which is ejected at the wave velocity reversal; 4) this sediment is then transported offshore in the weaker, longer offshore phase of wave motion.
- A simple grab and dump model (based on *Nielsen* [1988]), which describes the transport due to the vortex ejection mechanism is in agreement with both the magnitude and direction of the observed net suspended sediment transport.

- Suspended sediment transport due to mean currents was found to account for five times less net transport than the wave-forced suspended sediment transport. Thus, the wave forced sediment transport mechanisms are clearly dominant at LEO-15.

#### **Acoustic Doppler Bedload and Near-bottom Suspended Load Sensor**

- Based on the observations at LEO-15 it was hypothesized that unobserved wave-forced bedload or near-bottom suspended load forces ripple migration. Since a instrument to measure this form of sediment transport on the appropriate time and space scales does not exist, an instrument was developed to measure wave-forced bedload and near-bottom suspended load (see appendix A).

## Appendix A

### A initial study on using full spectrum pulsed doppler to measure sand transport on and near the seafloor

Peter Traykovski, James D. Irish, and James F. Lynch.

\*Dept. of Applied Ocean Physics and Engineering, Woods Hole Oceanographic Institution, Woods Hole, MA

#### Abstract

Recent observations of ripple migration and suspended sediment transport have shown that wave forced bedload and saltation load may be the dominant form of sediment transport in certain situations. There is a lack of suitable observational techniques to measure these modes of sediment transport. Therefore, a pulsed acoustic doppler technique is being examined to determine if it can quantitatively measure the bedload and saltation load flux magnitude and direction on a rapid time scale. A laboratory test of this technique was made in the WHOI 17m flume and excellent agreement in mass transport estimates were obtained between the acoustic results and a bedload trap. Based on these results a field deployable implementation of this technique should be pursued.

#### A.1 Introduction

Recent observations of ripple migration and suspended sediment transport (Traykovski *et al*, 1997) have shown that wave forced bedload and saltation load may be the dominant form of sediment transport in environments with coarse sand and non-linear shoaling waves. While traditional bedload traps are marginally suitable for measuring bedload rates in unidirectional flows, techniques for measuring bedload flux on the surface gravity wave time scale do not exist. Previous acoustics techniques for measuring bedload, such as those described by Sutton and Jaffe [1992], attempt to find a bedload velocity instead of the flux (mass times velocity.) We are developing a remote acoustic sensing instrument based on Doppler frequency shift to quantitatively measure sediment transport flux on and near the bed on a rapid (within wave period) time scale. Figure A-1 illustrates the three types of sediment transport modes. The bedload layer is where the grains are supported primarily by intergranular forces. The saltation layer is a transitional layer where the grains have frequency contact with the bottom and are supported by both intergranular forces and hydrodynamic forces, and finally the suspended layer is where the grains are supported only by hydrodynamic forces. Acoustic systems have been developed to measure the noise generated by intergranular collisions of gravel sized sediments moving as bedload [Williams et. al. 1989]. While these systems have been calibrated to measure bedload mass flux, they do not give the directional information needed for oscillatory flows, and may not be suitable for sand sized sediment.

The acoustic system shown in figure A-1 measures the doppler shift of backscattered energy from sand grains in all three layers. This doppler shift can be used to estimate a velocity, or velocity spectrum, of the moving sand grains. This combined with the back scattered intensity, or spectral level, which is assumed to be proportional to concentration, can produce an estimate of sediment flux. It has the unique advantage over other types of systems that velocity and concentration are measured from the same sand grains. Previous systems for measuring sediment transport, such as combining a current meter with a downward aimed acoustic backscatter sensor can not spatially resolve the thin saltation and bedload layers from the stationary bed, and thus can not estimate transport in these layers. A doppler based system can resolve these layers by their non-zero velocity. While range gating is possible with the doppler system geometry shown in figure A-1, it will only result in sampling different locations on the bottom. If a vertical profile of concentration and velocity through the water column is desired an alternate geometry can be used as shown in figure A-2. This is similar to the geometry used by Hay (Personal Comm.) and Zedel *et. al.*

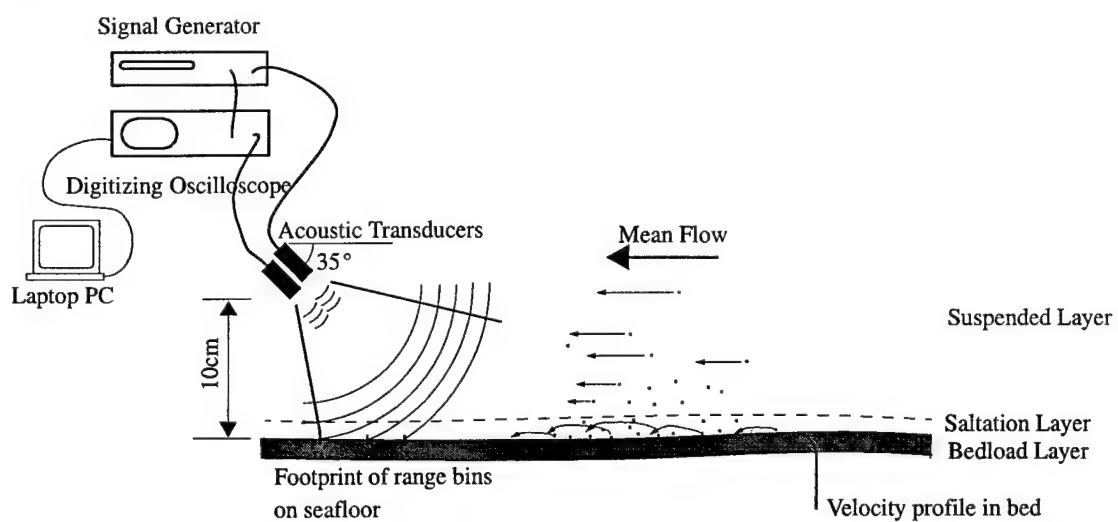


Figure A-1 Sketch of bedload, saltation, and suspended load layers and doppler system geometry.

(1996). This geometry can be used in three modes. A bistatic mode transmitting on the vertical axis and receiving on the angled axis can be used to measure vertical profiles of horizontal velocity. A monostatic mode on the vertical axis can be used to measure vertical profiles of vertical velocity. Finally a monostatic mode on the angled axis can be used to measure horizontal velocities on different locations on and near the bed. This final geometry is similar to the bistatic geometry with both transducers on the same angled axis shown in figure A-1.

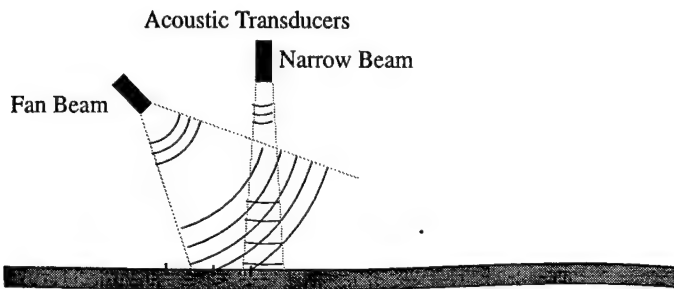


Figure A-2 Alternate Doppler geometry for measuring vertical profiles in the boundary layer, and near bed transport.

### A.2 Bedload vs. Velocity Estimates

Doppler instruments that measure scattering in the water column from objects moving at the mean water speed ( $U_0$ ), or possibly with some variance about the water speed, can be used to estimate a single velocity in each range bin from the mean of the doppler spectrum (e.g. the family of Acoustic Doppler Current Profilers by R.D. Instruments, Sontek, etc.), (Lhermiite *et al.*, 1984, Brumley *et al.*, 1991, Pinkel, 1981.) Previous techniques to acoustically measure bedload velocity, such as that described by Sutton and Jaffe [1992], use a time domain method to determine the mean velocity of the bedload.

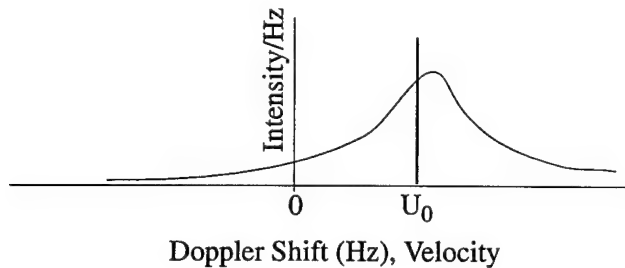


Figure A-3 Doppler shift with no strong stationary target

When a strong stationary target, such as the seafloor, is present in the range bin of interest along with moving sand grains the estimate of the mean velocity will be biased toward zero. This estimate of velocity with a strong stationary target present is not very useful since the bias is dependent on the strength of the stationary bed return relative to the moving target return. Therefore, other techniques are required to separate out the bedload signal.

Since the intensity ( $I$ ) at each doppler shift (or the continuous spectral level) is assumed to be proportional to the concentration ( $C$ ) of sand at the velocity ( $U$ ) corresponding to the doppler shift

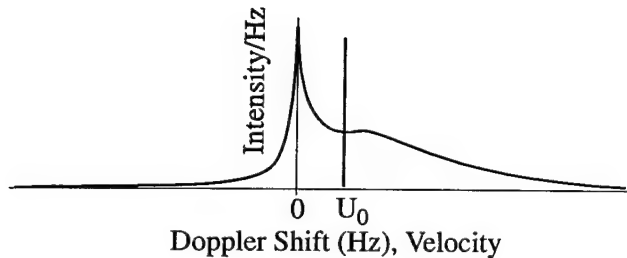


Figure A-4Doppler shift with a strong stationary target

( $f_s$ ), one should be able to make an accurate estimate of sand transport by integrating the doppler spectrum times the intensity if this assumption is valid

$$Q = \int C U dU = K \int I f_s df_s \quad (\text{EQ 1.1})$$

Here the constant  $K$  is a acoustic calibration factor that will depend on the grain properties, and acoustic frequency.

The principle limitation of this concept as applied to a bedload measurement is that if the bedload layer is thicker than the acoustic penetration into the bottom, sand that is moving will not receive acoustic energy and thus will not be included in the transport estimate. However, if this happens, it will be observed with this system, since the amplitude of the zero shifted Doppler signal will decrease, or disappear altogether. Using the definition of bedload presented earlier the proposed system will measure near bed suspended transport, saltation transport, and the upper layer of bedload transport if the bedload layer is thicker than the acoustic penetration depth. The acoustic penetration depth can be modified slightly by choosing a suitable acoustic frequency. Sutton and Jaffe [1992] found 50% penetration of 2.2MHz acoustic energy at 3mm with 1mm sand grains. Thus if the bedload layer is contained to a few grain diameters, there should be adequate acoustic penetration.

Acoustically, the assumption that backscattered intensity is proportional to concentration has been shown to be valid for dilute suspensions (Hay, 1983, 1992, Sheng and Hay, 1988). While the upper part of the saltation layer may be dilute with sand grains separated by over an acoustic wavelength on average, the lower part of this layer and the bed load layer are clearly not dilute. In the lower part of the saltation layer multiple scattering effects will become important as the particles are separated by less than a wavelength. Scattering from the bedload layer is complex, poorly understood, acoustic problem, since it is not simply an interface made of water on one side and

discrete particles in contact with one another on the other side, but the particles are moving, and thus changing separation distance. The particles exchange will exchange acoustic energy on a intermittent basis depending on how long they are in contact with neighboring particles. A bulk characterization of this layer is not necessarily appropriate since the particle diameter is on the order of the acoustic wavelength. Thus, for the purposes developing this instrument, we will make the assumption that acoustic backscattered intensity is proportional to concentration, and the results of calibration experiments will determine if this is a suitable approximation. It most likely to be valid for the saltation mode, and less likely to be valid for a thick bedload layer mode of transport, thus if most of the transport is occurring as saltation then this approximation should hold.

### A.3 Signal design and processing

Previous experience (Traykovski *et al.* 1997) and theoretical scattering models (Sheng and Hay, 1988) indicate that 2.5MHz is a good frequency for scattering measurements from 100 to 400 $\mu$ m sand grains. Transducers tuned for this frequency could also be borrowed from the ABS systems thus this was chosen as the carrier frequency ( $f_0$ ). It became necessary to shift it slightly to 2.475MHz due to aliasing from the 1MHz sampling rate as will be discussed later.

Doppler for a given velocity ( $U$ ) shift can be calculated by

$$f_s = \frac{-2U}{\lambda} = \frac{-2Uf_0}{c_0} \quad (\text{EQ 1.2})$$

where  $\lambda$  is the acoustic wavelength (0.06cm for 2.5Mhz in sea water with sound speed  $c_0=1500\text{m/s}$ ). In order to obtain velocity resolutions of a few cm/s, frequency resolution must be on the order of tens of Hz (33Hz  $\sim$  1cm/s). This requires a signal of temporal length  $1/30\text{Hz}=0.03\text{s}$ . The spatial length of this signal is  $0.03\text{s} * 1500,00\text{cm/s}=4500\text{cm}$ . This far greater than distance of the transducer from the bottom and will cause a problem since energy is still being transmitted while it is being received. A pulsed Doppler scheme can be used to alleviate this problem. In a pulsed Doppler, pulses shorter than the two way travel time (or distance) to the sea floor are transmitted and recorded coherently for the length of time required to meet the velocity resolution requirements.

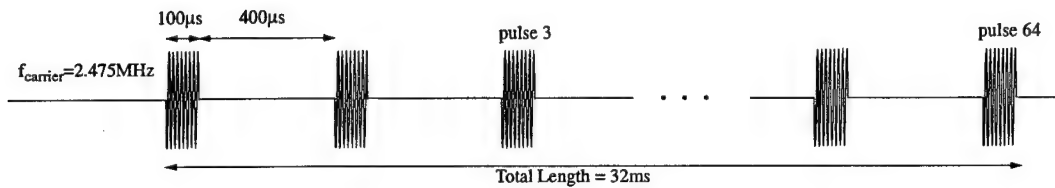


Figure A-5 Typical transmitted signal

For the flume and tank experiments, the transmitted signal consisted of a series of  $100\mu\text{s}$  long pulses, each separated by gap of  $400\mu\text{s}$ . This signal was generated on a ANALOGIC model 2020 signal generator using the following equation:

STOP

```
AT TRIG RPT 120 (FOR 1 0 RPT 80 (FOR 100u 5*SIN(2.475M*T) FOR 400u 0) MARK 10m)
CLK=40n
```

RUN

While 80 pulses were transmitted, the HP oscilloscope data acquisition system could only record a maximum of  $2^{15}=32,768$  points with at a sampling frequency of 1 MHz. This limited the received number of pulses to 65.5, of which 64 were processed to use a even power of two for Fourier transforms. The signal generator transmitted one ping (the series of 80 pulses) each second for 120 seconds. The data acquisition system was controlled via a RS232 serial link from a laptop PC with a PCPLUS communication software package script file. This script file allowed a ping to be recorded each time the operator hit a key on the PC keyboard. Four pings could be recorded on the four RAM channels on the oscilloscope. After this had occurred the scope would take about 3 minutes write these four pings to a floppy disk. This procedure limited the temporal sampling of the system to a maximum rate of 4 pings of  $0.0327\text{ s}$  each every 3 minutes.

The received signal was post-processed in MATLAB as follows: First, the signal was complex demodulated to remove the carrier. While the demodulation frequency should been 2.475MHz, it was found that the system actually received a carrier frequency of 2.47593MHz. The signal was low pass filtered with a filter of bandwidth 30KHz to remove high frequency noise due to aliasing the 2.475MHz carrier with a 1MHz sampling rate. This was chosen to be slightly wider than the spectral width of the  $100\mu\text{s}$  pulses. The signal was then block averaged in blocks of  $200\mu\text{s}$  (to be sure to catch the entire  $100\mu\text{s}$  pulse with a bottom location variability of 10cm due to bedform

migration) separated by  $400\mu\text{s}$  to match the  $500\mu\text{s}$  pulse interval. This yields 64 complex averaged samples of the magnitude and phase relative to the carrier of the 64 received pulses. Three steps of this process are shown in figure A-6 for illustrative purposes. While this example of processing only uses the one range bin that contains the bottom return, shorter averaging blocks could be used with different delays to obtain several range bins. The final step of signal processing is to transform the time series of 64 samples into the frequency domain using a fft. The values of the fft

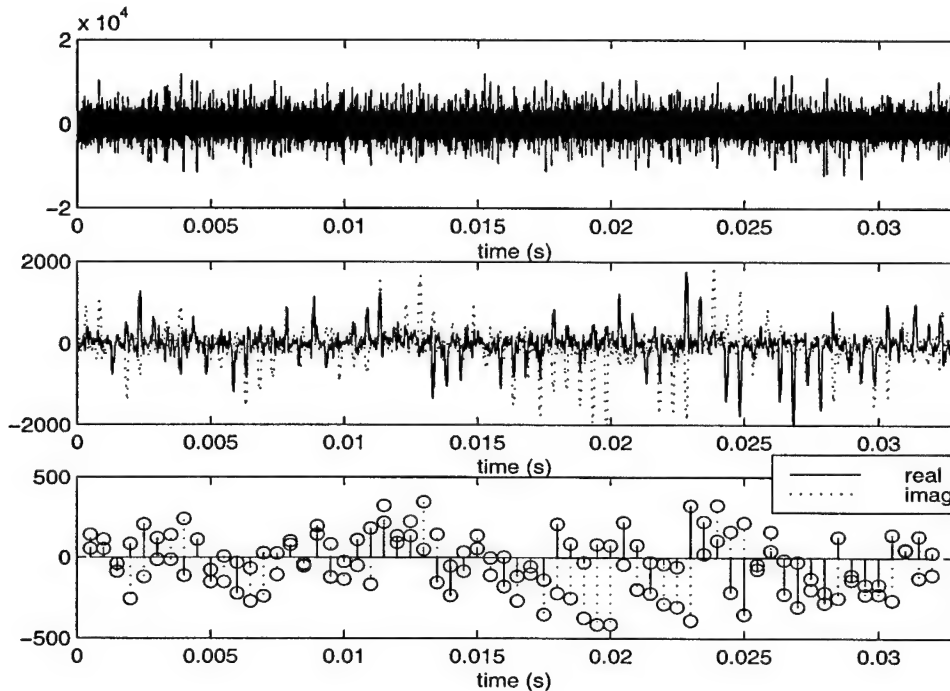


Figure A-6a) Raw time series. b) After complex demodulation and low-pass filtering. c) 64 samples after block averaging

are then squared so that they are proportional to acoustic intensity instead of pressure. The frequency axis of the fft can be converted to velocity using equation 2. The frequency bandwidth is determined by  $1/(the\ pulse\ interval\ of\ 500\mu\text{s})=2,000\text{Hz}$ . Thus velocities from  $-30\text{cm/s}$  to  $30\text{cm/s}$  can be measured. Velocities greater than  $30\text{cm/s}$  will be wrap around on to negative velocities.

In a pulsed doppler scheme there exists a trade-off between the maximum velocity measured and the pulse interval, as determined by the distance to the seafloor. In this case we have set the maximum velocity to  $\pm 30\text{cm/s}$ , and thus the maximum distance to the seafloor is  $(500\mu\text{s} \times 150,000\text{cm/s})/2 = 37.5\text{cm}$ . In order to increase the maximum velocity the transducer

would need to be closer to the seafloor. A lower carrier frequency would also increase the maximum velocity for a given maximum range. This however, would push scattering from finer sand grains farther into the Raleigh scattering regime which is undesirable. As discussed earlier the length of the signal, or number of pulses is one factor in determining the velocity resolution. However, if the correlation time scale of the scattering process is shorter than the signal length, this may determine the velocity resolution. In calculating total bedload flux all the velocity bins will be integrated so high velocity resolution is not crucial for this system to work. However, low resolution will bias the flux estimate. The return from the stationary bottom in particular, if spread into adjacent velocity bins could bias the results towards zero. Since the stationary bed is stationary it should have an “infinite” correlation time scale, so resolution of the bed in the frequency domain will be determined by the signal length.

In terms of signal processing considerations, the velocity estimation techniques, such as the pulse pair algorithm used by Zedel. *et. al.* [1996] and the time domain correlation technique used by Sutton and Jaffe [1992], use a high bandwidth but short time-length signal. This allows an accurate estimation of time delay, or phase rate change, to give an accurate velocity estimate. However, it does not allow the stationary bottom return to decorrelate from the returns from the moving, Doppler shifted, targets within the time window. Our technique will employ a high bandwidth, and longer time signal to give a higher time bandwidth product, and thus allow the multiple Doppler shifts from targets to decorrelate from each other and the stationary bed return. The longer time length of our signal is due to the fact that in our technique all pulses are used coherently as opposed to just a pair. While the previous techniques rely on a high correlation between successive pulse pairs, the techniques described here does not require a high pulse to pulse correlation, but does require some degree of phase coherence at the different frequency shifts within the time window used to form the spectra in order to avoid excessive frequency spreading. Once the intensity spectrum has been calculated by means of a fft the bedload flux estimate is calculated by simply multiplying the intensity in each bin by the velocity associated with each bin and then summing the product over all the velocity bin (equation 1).

#### A.4 Experiments and Results

To test these concepts two sets of experiments were performed. The first involved measuring the doppler spectrum of sand sliding down a inclined plane with the geometry shown in figure A-7.

This was a first order test to see if a Doppler shift could be recorded in the presence of a stationary bottom producing a strong zero shifted return, and to determine if the data acquisition and signal generation system were working as expected. No corroborative measurements of sand flux were made in this experiment, but the approximate velocity of the sand was measured using the length of time it took to reach the bottom of the tank. The inclined plane was constructed from a sheet of plywood with sand glued on it so acoustic energy scattered off the plane would not simply be scattered in the spectral direction.

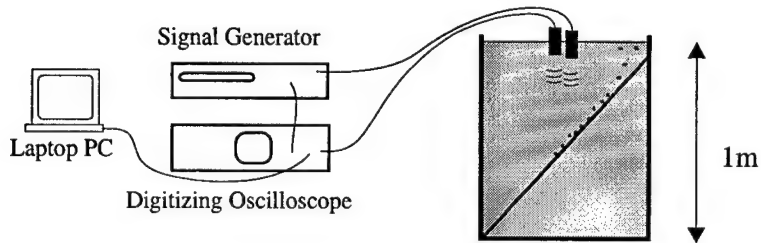


Figure A-7 Inclined plane tank setup

Figure A-8 shows spectra from four pings with sand being poured down the ramp and from four pings with only the stationary bottom. The observed doppler shifts of up to 500Hz are roughly consistent with the 10-15cm/s fall velocities observed in the tank. Since results from the tank experiment were encouraging a flume experiment was designed to quantitatively examine whether bedload could be measured.

The flume experiment was performed in the WHOI Rinehart Coastal Research Center 17m flume, with a geometry as shown in figure A-1. A bedload trap consisting of a 1 inch deep tray of 20 x 20 in<sup>2</sup> area with 1cm square grating in it was used to quantify bedload and saltation load down stream of the acoustic sampling volume. Water flow speeds were measured 18cm from the bed with the flume LDV. The flume was run at six speeds: 22, 35, 45, 50, 55, and 62cm/s. The runs of 22, 35, 50, and 62cm/s were performed in order of increasing speed, and then the runs of 45 and 55cm/s were performed, also in order of increasing speed. Thus, for the latter two runs the ripples were not in equilibrium with the flow since large ripples were left over from the 62cm/s run performed previously. A few sand grains began to move at 22cm/s but bedload measurements were not taken since the transport rate was very low. At 35cm/s the bedload trap filled to 1/4 capacity in one hour. By 62 cm/s the bedload trap filled to 3/4 capacity in 6 minutes. Visual observations of the bedload

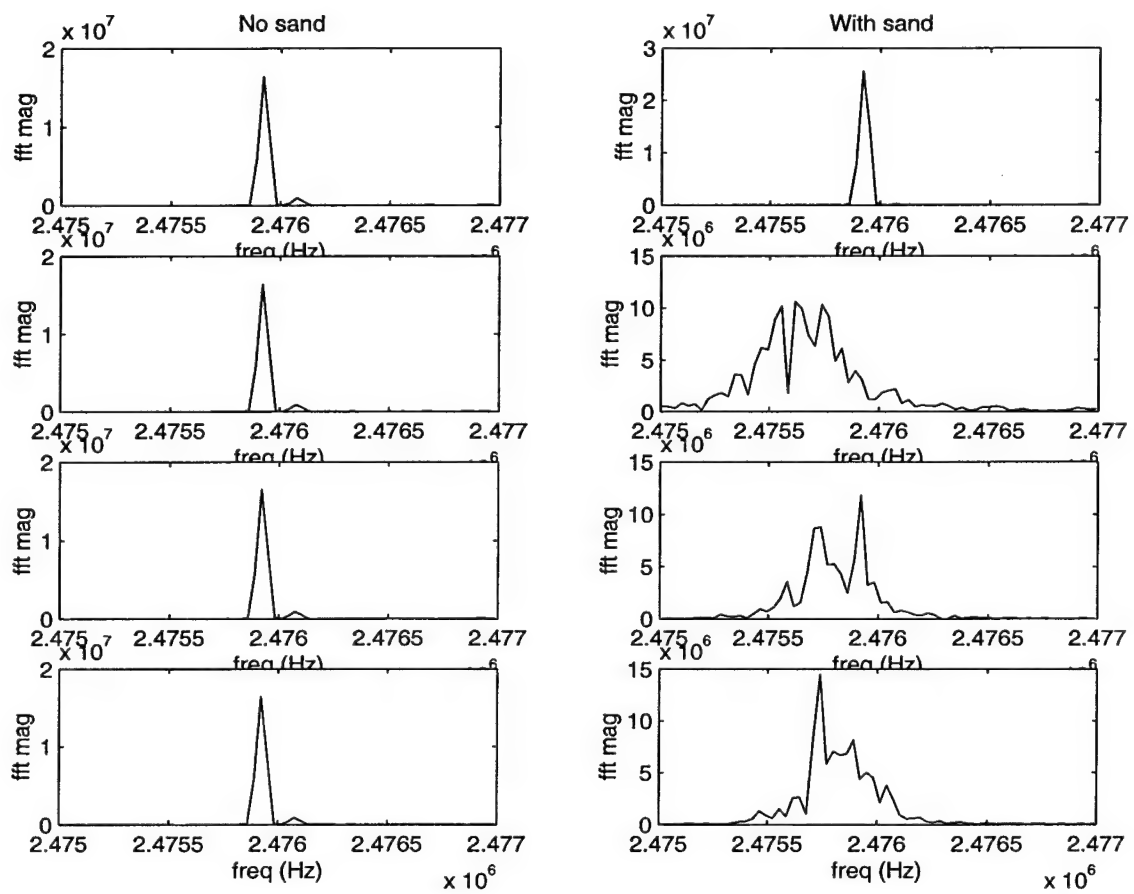


Figure A-8 Spectra from included plane tank test. Left side: with no moving sand only the stationary bed return at the carrier frequency is visible; Right side: with moving sand a “shoulder” of down-shifted (away from the transducer) returns appears.

trap indicated that it was filled by ripple migration forced by saltation load and bedload in the form of avalanches down the lee side of a ripple.

Six sets of four pings were collected at each flow speed. The pings were separated by about 1 s and the sets were separated by 2 to 3 minutes. Figure A-9 shows spectra for the six speeds. The increased shoulder on the up frequency shift side of the stationary bed return (since the transducer is aimed into the flow) is clearly seen as flow speed increases. Also shown in figure A-9 is the spectra of velocity times intensity (flux). In these plots the zero velocity component of flux obviously gives no flux. However, over the range of velocities from slightly above zero to a value of 20 to 30 cm/s (depending on flow speed) the different velocity components have roughly equal contributions to the total flux i.e. the velocity times intensity spectra is roughly flat. This make physical sense because of the compensating effects of a greater concentration of slow moving

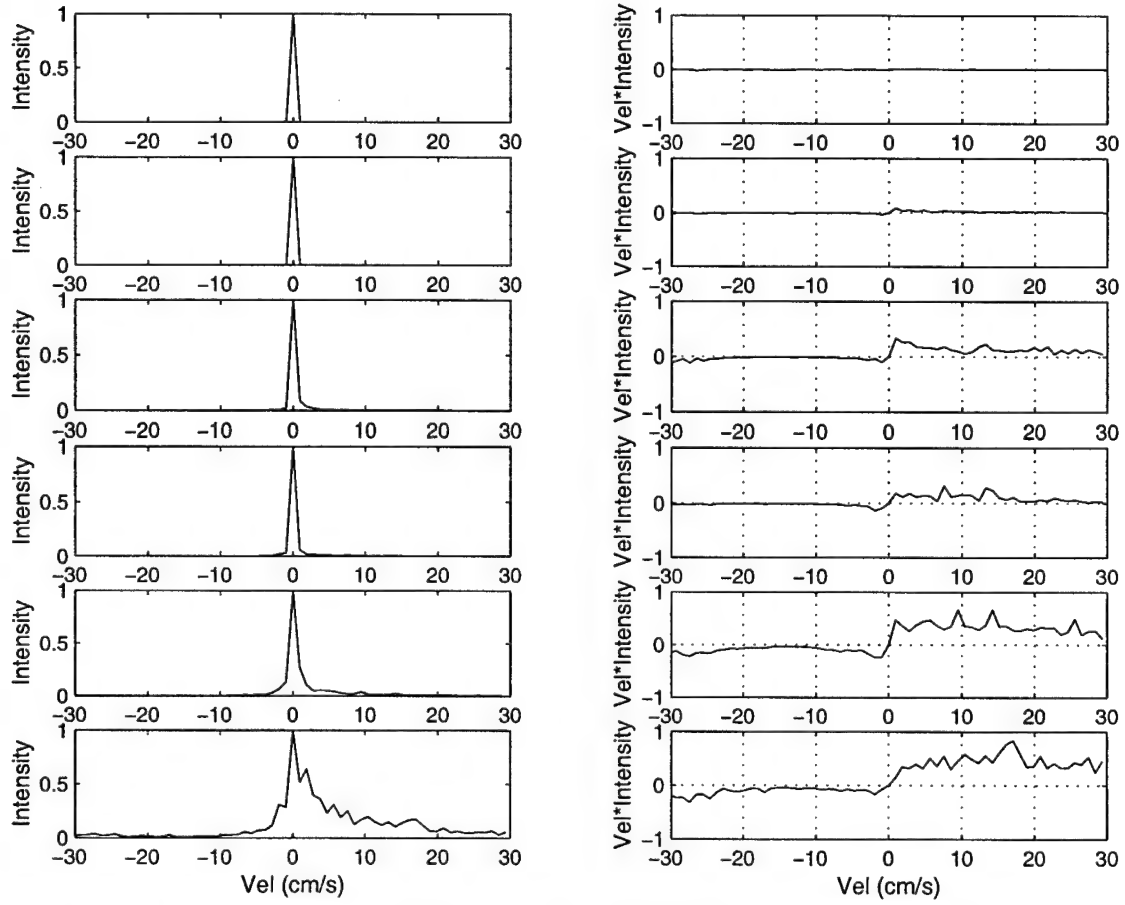


Figure A-9 Left: Doppler Spectra of intensity for the six flow speeds: 22, 35, 45, 50, 55, and 62 cm/s in order of increasing flow speed. The spectra are averaged over all pings and normalized to have a maximum of unity. Right: Doppler spectra of flux (velocity \* intensity) with all six flow speeds are normalized by a single constant.

particles closer to the bed and fewer fast moving particles higher up in the flow in the product of velocity times intensity that is spatially averaged in depth over the sampling volume of the instrument.

These individual spectra that were averaged to give the flux spectra shown on the right side figure A-9 are then integrated using equation 2 to get the acoustics bedload measurement which is then averaged to get one bedload measurement for each flow speed. Since some of the negative velocities may be positive velocity greater than 30 cm/s that have wrapped around the spectra integrated first by using the whole spectra, and then by using only the positive velocity half of the spectra. The results from these calculations along with the bedload measurement from the trap are shown in figure A-10. A single empirical acoustic calibration constant ( $K$  from eqn. 1) was used to

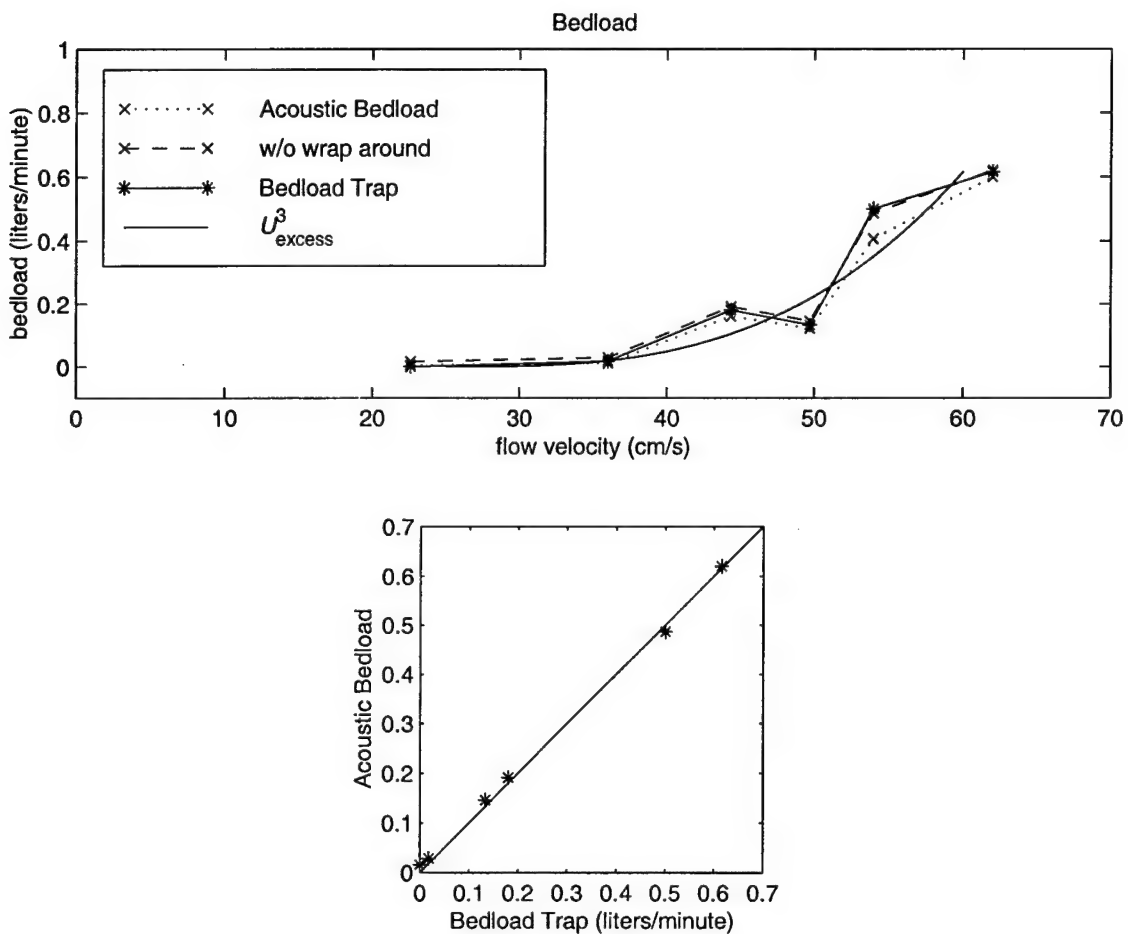


Figure A-10Upper panel: Acoustic and bedload trap measurement of bedload vs. flume nominal flow speed.  
 Lower panel Acoustically measured bedload vs. bedload trap

scale the acoustic data to best fit the bedload data. A simple theoretical bedload model of  $U^3_{\text{excess}}$  is also shown where  $U_{\text{excess}}$  is defined as  $U - U_{\text{critical}}$ . A scaling constant was used to make  $U^3_{\text{excess}}$  fit the bedload data. The critical velocity for initiation of motion ( $U_{\text{critical}}$ ) was observed to be 23cm/s for this size sand.) The two points that are substantially above the  $U^3_{\text{excess}}$  are the points that were performed with ripples that not in equilibrium with the flow. The agreement between the acoustic measurement of bedload and the bedload trap is excellent. Of particular interest is that the acoustic measurement is able to capture the "high" points which are most likely due to disequilibrium between the ripples and the flow speed. Before performing the experiment we expected that the slow temporal sampling, due to disk writing time, of this system would be unable to produce accurate estimates of mean bedload since the transient nature of the bedload over the migrating ripples would not be captured. However, the beam width of these transducers is fairly

wide (-3db at 15° from on axis in the transducer farfield) thus, there is spatial averaging over approximately one ripple wavelength. This spatial averaging is probably partially responsible for compensating for the slow temporal sampling in producing the excellent agreement between the bedload trap and the acoustic estimate of bedload shown in figure A-10.

From visual observation of the sand motion in the flume it appeared that most of the transport was occurring in saltation mode on the upstream side of a ripple. Bedload motion, supported by intergranular forces, seemed to occur largely in the form of avalanches down the lee side of a oversteepened ripple. Thus the acoustic penetration of the bedload layer did not pose a problem obtaining a quantitative agreement between the bedload trap and the acoustic transport estimate. For this experiment the assumption that acoustic intensity is proportional to concentration has been shown to be valid.

### A.5 Conclusions

Based on these preliminary results, this technique shows great promise for much needed field measurements. Therefore, development of a field deployable version should be undertaken as soon as possible. The Sontek Dopbeam system is well adapted for this type of measurement so development efforts should begin with adapting this system to our signal processing requirements.

### Acknowledgments

This project was funded by a WHOI Keck award to investigators James F. Lynch and James D. Irish. Special thanks go to Jim Doutt for writing the procomm script to interface with HP digital oscilloscope data acquisition system, to Sandy Williams for providing the HP digital oscilloscope, and to Steve Fries for assisting with the flume experiment and Processing the LDV data. Initial feasibility tank experiment were performed using Tim Stanton's signal generation and data acquisition equipment with the assistance of Dezhang Chu. Thanks also go to Gene Terray for valuable discussions regarding this project.

### References

Brumley, B.H., R.G. Cabrera, K.L. Denies, and E.A. Terray, "Performance of a broad-band acoustic Doppler current profiler," *IEEE J. Ocean Eng.* 16, p402-407, 1991

- Hay, A.E., "On the remote acoustic detection of suspended sediments at long wavelengths," *J. Geophys. Res.* **88**(c12), p7525-7542 (1983)
- Hay, A.E., "Vertical Profiles of suspended sand concentration and size from multifrequency acoustic backscatter," *J. Geophys. Res.* **97**(c10), p 15,661-15,677 (1992)
- Lhermiite, R. and R. Serafin, "Pulse to pulse coherent Doppler sonar signal processing techniques," *J. Atmos. Oceanic Tech.* 1(4), p293-308, 1984
- Pinkel, R., "On the use of Doppler sonar for internal wave measurements," *Deep-Sea Res.* 28A, p269-289, 1981
- Sheng, J. and A. E. Hay, "An examination of the spherical scatterer approximation in aqueous suspension of sand," *J. Acoust. Soc. Am.* **83** (2), p598-610 (1988)
- Sutton D.W. and J.S. Jaffe, Acoustic bedload velocity estimates using a broadband pulse-pulse time correlation technique, *Jour. Acoust. Soc. Am.*, 92(3), p1692-1698, 1992.
- Williams, J.J., P.D. Thorne, A.D. Heathershaw, Comparisons between acoustic measurements and predictions of the bedload transport of marine gravels. *Sedimentology*, 36, p973-979, 1989
- Traykovski, P., A.E. Hay, J.F. Lynch, J.D. Irish, Geometry, migration, and evolution of wave orbital ripples at LEO-15, submitted to *J. Geophys. Res.*, 1997
- Zedel, L., A.E. Hay, R. Cabrera, and A. Lohrmann, Performance of a single beam pulse to pulse coherent Doppler profiler, *IEEE Jour. of Oceanic Eng.*, Vol. 21, No. 3, p 290-297, 1996.

**Document Library**  
*Distribution List for Technical Report Exchange—November 1998*

University of California, San Diego  
SIO Library 0175C  
9500 Gilman Drive  
La Jolla, CA 92093-0175

Working Collection  
Texas A&M University  
Dept. of Oceanography  
College Station, TX 77843

Hancock Library of Biology & Oceanography  
Alan Hancock Laboratory  
University of Southern California  
University Park  
Los Angeles, CA 90089-0371

Fisheries-Oceanography Library  
151 Oceanography Teaching Bldg.  
University of Washington  
Seattle, WA 98195

Gifts & Exchanges  
Library  
Bedford Institute of Oceanography  
P.O. Box 1006  
Dartmouth, NS B2Y 4 A2  
CANADA

Library  
R.S.M.A.S.  
University of Miami  
4600 Rickenbacker Causeway  
Miami, FL 33149

NOAA/EDIS Miami Library Center  
4301 Rickenbacker Causeway  
Miami, FL 33149

Maury Oceanographic Library  
Naval Oceanographic Office  
Building 1003 South  
1002 Balch Blvd.  
Stennis Space Center, MS 39522-5001

Research Library  
U.S. Army Corps of Engineers  
Waterways Experiment Station  
3909 Halls Ferry Road  
Vicksburg, MS 39180-6199

Library  
Institute of Ocean Sciences  
P.O. Box 6000  
Sidney, B.C. V8L 4B2  
CANADA

Institute of Geophysics  
University of Hawaii  
Library Room 252  
2525 Correa Road  
Honolulu, HI 96822

National Oceanographic Library  
Southampton Oceanography Centre  
European Way  
Southampton SO14 3ZH  
UK

Marine Resources Information Center  
Building E38-320  
MIT  
Cambridge, MA 02139

The Librarian  
CSIRO Marine Laboratories  
G.P.O. Box 1538  
Hobart, Tasmania  
AUSTRALIA 7001

Library  
Lamont-Doherty Geological Observatory  
Columbia University  
Palisades, NY 10964

Library  
Proudman Oceanographic Laboratory  
Bidston Observatory  
Birkenhead  
Merseyside L43 7 RA  
UK

Library  
Serials Department  
Oregon State University  
Corvallis, OR 97331

IFREMER  
Centre de Brest  
Service Documentation-Publications  
BP 70 29280 PLOUZANE  
FRANCE

Pell Marine Science Library  
University of Rhode Island  
Narragansett Bay Campus  
Narragansett, RI 02882

<b>REPORT DOCUMENTATION PAGE</b>		<b>1. REPORT NO.</b> MIT/WHOI 98-25	<b>2.</b>	<b>3. Recipient's Accession No.</b>
<b>4. Title and Subtitle</b>  Observations and Modeling of Sand Transport in a Wave Dominated Environment		<b>5. Report Date</b> June 1998		
		6.		
<b>7. Author(s)</b> Peter Traykovski		<b>8. Performing Organization Rept. No.</b>		
<b>9. Performing Organization Name and Address</b>  MIT/WHOI Joint Program in Oceanography/Applied Ocean Science & Engineering		<b>10. Project/Task/Work Unit No.</b> MIT/WHOI 98-25		
		<b>11. Contract(C) or Grant(G) No.</b> (C) N00014-97-1-0556 (G) NA46GU0149		
<b>12. Sponsoring Organization Name and Address</b>  Office of Naval Research National Oceanic and Atmospheric Administration		<b>13. Type of Report &amp; Period Covered</b> Ph.D. Thesis		
		14.		
<b>15. Supplementary Notes</b> This thesis should be cited as: Peter Traykovski, 1998. Observations and Modeling of Sand Transport in a Wave Dominated Environment. Ph.D. Thesis. MIT/WHOI, 98-25.				
<b>16. Abstract (Limit: 200 words)</b>  Observations of bedforms, suspended sediment and water velocities were used to examine sediment transport processes at the sandy LEO-15 site located off the New Jersey coast. The bedforms were observed during storms using a rotary sidescan sonar and were found to be wave orbital scale ripples. The onshore migration of these ripples was forced by non-linear wave velocities, and could be related to a simple bedload model. Observations of suspended sand flux were calculated from acoustic backscattering profiles and water velocity profiles. Suspended sand transport forced by wave velocities was found to occur primarily during the weaker offshore phase of wave motion, as part of a vortex ejection mechanism. This net offshore suspended sediment flux was an order of magnitude less than the flux associated with onshore ripple migration. Thus it is hypothesized that ripple migration was forced by unobserved bedload or near bottom suspended flux. The net suspended sediment flux due to mean currents was a factor of five less than the wave-forced offshore suspended flux. These wave dominated events at LEO-15 represent a contradiction of the conceptual idea that waves are primarily responsible for suspending sediment and mean currents provide the transport mechanism.				
<b>17. Document Analysis</b> <b>a. Descriptors</b> Wave Sediment Transport				
<b>b. Identifiers/Open-Ended Terms</b>				
<b>c. COSATI Field/Group</b>				
<b>18. Availability Statement</b>  Approved for publication; distribution unlimited.		<b>19. Security Class (This Report)</b> <b>UNCLASSIFIED</b>	<b>21. No. of Pages</b> 151	
		<b>20. Security Class (This Page)</b>	<b>22. Price</b>	